The Dissertation Committee for Arindam Sarkar Certifies that this is the approved version of the following dissertation:

SYNTHESIS AND CHARACTERIZATION OF NANOSTRUCTURED PALLADIUM-BASED ALLOY ELECTROCATALYSTS

Committee:

Arumugam Manthiram, Supervisor

Keith J. Stevenson

Paulo Ferreira

Harovel G. Wheat

Jeremy P. Meyers

SYNTHESIS AND CHARACTERIZATION OF NANOSTRUCTURED PALLADIUM-BASED ALLOY ELECTROCATALYSTS

by

Arindam Sarkar, B. E.; M. Tech.

Dissertation

Presented to the Faculty of the Graduate School of
The University of Texas at Austin
in Partial Fulfillment
of the Requirements
for the Degree of

Doctor of Philosophy

The University of Texas at Austin
August 2009

Dedication

Dedicated to my parents

Acknowledgements

I would like to express my deepest gratitude to my dissertation advisor Professor Arumugam Manthiram who gave me an opportunity to continue my higher studies. I am deeply indebted to him for introducing me to this new area of electrochemistry and electrocatalysis. Being an entirely novice to this area, initially it has been a walk for me into the dark. I thank Professor Manthiram for his expert beacon-like guidance and his encouragement.

I would also like to express my gratitude to Dr. A. Vadivel Murugan for his help and support. I thank Professors Keith J. Stevenson, Jeremy P. Meyers, Paulo Ferreira, and Harovel G. Wheat for serving on my committee and providing helpful suggestions and ideas.

I also thank Jung-Hyun Kim, Wen Li, Eungje Lee, and Juan Zhou for their help in experimentation and stimulating discussions, which helped to firm up my ideas and concepts. I also thank past and present members of Professor Manthiram's group for their assistance and support. Additionally, financial support by the National Science Foundation and Welch Foundation is gratefully acknowledged.

Finally, and most importantly, I thank my parents for their boundless love and support.

SYNTHESIS AND CHARACTERIZATION OF NANOSTRUCTURED PALLADIUM-BASED ALLOY ELECTROCATALYSTS

Publication No._____________

Arindam Sarkar, Ph.D.
The University of Texas at Austin, 2009

Supervisor: Arumugam Manthiram

Low temperature fuel cells like proton exchange membrane fuel cells (PEMFC) are expected to play a crucial role in the future hydrogen economy, especially for transportation applications. These electrochemical devices offer significantly higher efficiency compared to conventional heat engines. However, use of exotic and expensive platinum as the electrocatalyst poses serious problems for commercial viability. In this regard, there is an urgent need to develop low-platinum or non-platinum electrocatalysts with electrocatalytic activity for the oxygen reduction reaction (ORR) superior or comparable to that of platinum.

This dissertation first investigates non-platinum, palladium-based alloy electrocatalysts for ORR. Particularly, Pd-M (M = Mo and W) alloys are synthesized by a novel thermal decomposition of organo-metallic precursors. The carbon-supported Pd-M (M = Mo, W) electrocatalyts are then heat treated up to 900 ^{o}C in H_2 atmosphere and investigated for their phase behavior. Cyclic voltammetry (CV) and rotating disk electrode (RDE) measurements reveal that the alloying of Pd with Mo or W significantly enhances the catalytic activity for ORR as well as the stability (durability) of the electrocatalysts. Additionally, both the alloy systems exhibit high tolerance to methanol, which is particularly advantageous for direct methanol fuel cells (DMFC).

The dissertation then focuses on one-pot synthesis of carbon-supported multi-metallic Pt-Pd-Co nanoalloys by a rapid microwave-assisted solvothermal (MW-ST) method. The multi-metallic alloy compositions synthesized by the MW-ST method show much higher catalytic activity for ORR compared to their counterparts synthesized by the conventional borohydride reduction method. Additionally, a series of Pt encapsulated Pd-Co nanoparticle electrocatalysts are synthesized by the MW-ST method and characterized to understand their phase behavior, surface composition, and electrocatalytic activity for ORR.

Finally, the dissertation focuses on carbon-supported binary Pt@Cu and ternary Pt_xPd_{1-x}@Cu "core-shell" nanoparticles synthesized by a novel galvanic displacement of Cu by Pt^{4+} and Pd^{2+} at ambient conditions. Structural characterizations suggest that the Pt@Cu nanoparticles have a Pt-Cu alloy layer sandwiched between a copper core and a Pt shell. The electrochemical data clearly point to an enhancement in the activity for ORR for the Pt@Cu "core-shell" nanoparticle electrocatalysts compared to the commercial Pt electrocatalyst, both on per unit mass of Pt and per unit active surface area basis. The increase in activity for ORR is ascribed to electronic modification of the outer Pt shell by the Pt-Cu alloy core. However, incorporation of Pd to obtain Pt_xPd_{1-x}@Cu deteriorates the activity for ORR.

Table of Contents

List of Tables

List of Figures

Chapter 1: Introduction

1.1 FUEL CELLS

One of the greatest challenges of the 21st century is to address the growing global energy need and environmental concerns. The limited availability of fossil fuels, their unequal distribution among various nations, and the pollution associated with combustion has mandated the development of alternative, unconventional energy technologies. Although for stationary power applications, a host of clean energy technologies like solar cells, wind power, and nuclear energy are appealing, transportation applications overwhelmingly rely on fossil fuels. In this regard, hydrogen as an energy carrier is attractive and is becoming increasingly popular. Nevertheless, the effective utilization of hydrogen must rely on the device that converts the chemical energy of hydrogen into useful work. One such device is a fuel cell. Fuel cells are electrochemical devices that can effectively convert the chemical energy of hydrogen directly into electrical energy [1-5].

Conventional heat engines that burn the fuel depend on the temperature difference between the source (engine) and the sink (ambient) to generate useful power. Therefore, they are limited by the maximum Carnot's cycle efficiency. On the other hand, fuel cells convert the chemical energy directly into electrical energy, and unlike heat engines, they are not limited by the Carnot's cycle efficiency. Consequently, they can have very high efficiency. A fuel cell converting the chemical energy of hydrogen in combination with oxygen directly into electrical energy offers the additional advantage of clean energy with little or no pollution as water is the only product. Fuel cells are an important technology for a wide variety of applications including transportation, on-site power generation, backup power for hospitals and other such critical establishments, power modules for laptops and small electrical devices, and military applications.

At the heart of a typical low temperature fuel cell lies the membrane-electrode assembly (MEA), which basically consists of an ionomer membrane sandwiched between two catalyst-coated gas diffusion layers (anode and cathode). In a typical fuel cell, the hydrogen fuel fed through the anode is catalytically dissociated into protons and electrons. The protons travel through the membranes and combines catalytically with the oxygen (fed through the cathode) to form water, while the electrons travel through an external circuit to generate electrical power [1-6].

1.2 THERMODYNAMICS AND KINETICS OF A FUEL CELL

1.2.1 Thermodynamics of a fuel cell

The maximum work other than the pressure-volume work that can be obtained for any system is given by ΔG. In the case of fuel cells, the maximum electrical work obtained is defined as

$$W_{el} = \Delta G = -nFE \qquad [1.1]$$

where n is the number of electrons participating in an electrochemical reaction, F is the Faraday constant, and E is reversible cell potential.

For the reaction of hydrogen and oxygen leading to water, the overall fuel cell reaction can be written as

$$H_2 + \frac{1}{2} O_2 \rightarrow H_2O \qquad [1.2]$$

and the change in Gibb's free energy can be expressed as

$$\Delta G = \Delta G^0 + RT\, ln \frac{p_{H_2O}}{p_{H_2}\sqrt{p_{O_2}}} \qquad [1.3]$$

where R is the gas constant, T is the temperature in Kelvin, and p is the partial pressure of the gases. Similarly, the cell potential can be expressed as

$$\Delta E = \Delta E^0 + \frac{RT}{nF} ln \frac{p_{H_2O}}{p_{H_2}\sqrt{p_{O_2}}} \quad [1.4]$$

1.2.2 Kinetic considerations

Although the thermodynamic cell potential defines the open circuit voltage (V) of a fuel cell, once current is drawn, the voltage (V) drops because of irreversible losses [7-10]. Generally, the losses can be classified into three categories: (a) ohmic polarization, (b) concentration polarization, and (c) activation polarization.

a) Ohmic polarization is caused by the resistance for the migration of ions in the electrolyte as well as the resistance for the flow of electrons. Mathematically, it can be expressed as

$$\eta_{Ohm} = i. R \quad [1.4]$$

where, i is the current and R the resistance.

b) Concentration polarization occurs when the reactants are consumed rapidly and the reactants do not diffuse as fast as they are being consumed. A polarization due to mass transport can be described as

$$\eta_{Conc.} = \frac{RT}{n.F} \ln\left(1 - \frac{i}{i_L}\right) \quad [1.5]$$

where, i_L is the limiting current.

c) Activation polarization is purely due to the electrocatalyst. It quantifies the loss due to slow rate of reaction at the surface of the electrocatalyst. Sluggish electrode kinetics causes a large drop in cell potential for a small change in current. The nature of surface, species formed during reaction, and the intrinsic characteristics of the electrocatalysts play an important role in the reaction kinetics and influence the activation polarization. A measure of the kinetics of the rate-controlling step is the Tafel equation,

$$\eta_{Act.} = \frac{RT}{\alpha n.F} \ln\left(\frac{i}{i_0}\right) \qquad [1.6]$$

where, i_o is the exchange current density and α is the transfer coefficient. A plot of $\eta_{Act.}$ vs ln(i) yields a straight line and the slope is called Tafel slope, which measures the resistance due to charge transfer. A good electrocatalyst must have a Tafel slope a low as possible.

The final cell voltage can then be defined as

$$V_{cell} = E^{Cathode} - E^{Anode} - |\eta_{Act}{}^{Anode}| - |\eta_{Act}{}^{Cathode}| - (\eta_{Conc.}{}^{Anode} + \eta_{Conc.}{}^{Cathode}) - \eta_{Ohm} \qquad [1.7]$$

Fig. 1.1 illustrates the various over-potentials in a fuel cell.

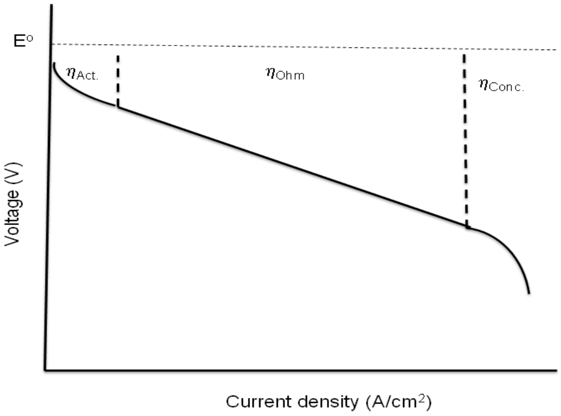

Figure 1.1. Current-voltage curve of a fuel cell showing various losses.

1.3 TYPES OF FUEL CELLS

There are different types of fuel cells and typically they are classified according to the electrolyte used [3,5]. The electrolyte in turn dictates the temperature of operation, the choice of fuel, fuel processing equipments, and choice of materials for device components (current collectors, electrodes, interconnects, etc.). Broadly, they are classified into 5 major types:

- Proton exchange membrane fuel cells (PEMFC)
- Alkaline fuel cells (AFC)
- Phosphoric acid fuel cells (PAFC)
- Molten carbonate fuel cells (MCFC)
- Solid oxide fuel cells (SOFC)

The section below provides a brief overview of the various types of fuel cells.

1.3.1 Proton exchange membrane fuel cells (PEMFC)

The electrolyte in these types of fuel cells is a hydronium ion (H_3O^+) conducting membrane (fluorinated sulphonic acid or other similar types). Typically, carbon electrodes coated with a catalyst (platinum, platinum alloys, non-platinum electrocatalysts) are used at both the anode and cathode with metal interconnects. For efficient operation, water management is vital and the operating conditions should be such so as not to dry the membrane or flood the electrodes. Also, extensive fuel processing is required for both anodes and cathodes as they are easily poisoned by CO and sulfur-containing species even at trace levels.

The primary advantage with PEMFC is the solid electrolyte, which provides excellent resistance to gas crossover, offers low temperature of operation ($< 100\ ^oC$), and minimizes corrosion of the cell components. However, the narrow operating temperature and complex water management lead to little operational maneuverability. Also, the use of exotic and expensive metal electrocatalysts is a severe limitation to large scale deployment and commercialization of the technology.

A type of PEMFC that employs methanol as a fuel is known as direct methanol fuel cell (DMFC). The use of methanol alleviates the need to build complex storage system for hydrogen in a car as well as infrastructural issues associated with reforming and transporting hydrogen. The electrochemical oxidation of methanol involves 6 electron transfer (higher current) and the thermodynamic potential (0.02V vs NHE) is close to that of hydrogen [3]. However, the oxidation of methanol is kinetically slow and the reaction intermediates tend to poison the catalyst. The crossover of methanol from the anode to the cathode and its oxidation at the cathode also poses a significant challenge to large scale commercialization. For both PEMFC and DMFC, the charge carrier is a proton.

1.3.2 Alkaline fuel cells (AFC)

In alkaline fuel cells (AFC), concentrated KOH is used as an electrolyte. The charge carrier is OH^- ions. AFC's can operate in a wide temperature range (50 – 250 ^oC). This type of fuel cell shows excellent performance because of facile oxygen reduction reaction (ORR) kinetics. One of the desirable attributes of AFC is the ability to use a variety of electrocatalysts. This in turn makes them economical from the view of electrocatalyst cost. However, this type of fuel cell is sensitive to CO_2 because of the presence of KOH. The fuel reforming conditions are stringent and these cells cannot operate on air.

1.3.3 Phosphoric acid fuel cells (PAFC)

A phosphoric acid fuel cell operates similar to PEMFC, but uses phosphoric acid in silicon carbide matrix as the electrolyte. The operating temperature for this type of fuel cell is 180 – 200 ^oC. The prime advantage of this type of fuel cells is the high temperature of operation, which lessens the requirement of high purity fuel and oxygen. Although the efficiency is lower compared to PEMFC, less complex fuel conversion makes it economically feasible. However, this type of fuel cells uses precious noble metals (Pt) as the catalyst. As in PEMFC, the charge carrier is H^+.

1.3.4 Molten carbonate fuel cells (MCFC)

Molten carbonate fuel cells use molten alkali carbonate salts in lithium aluminum oxide as the electrolyte. The charge carrier is CO_3^{2-} ions. At higher temperatures (600 - 700 °C), the alkali carbonates form a highly conductive electrolyte and provides ionic conduction. Because of the much higher temperature of operation, the requirement of expensive precious metals to catalyze the electrochemical reactions is eased and Ni (anode) and NiO (cathode) are adequate to promote the reactions. However, the electrolyte is corrosive and high temperature of operation limits the choice of cell parts, interconnects, and other hardware materials.

1.3.5 Solid oxide fuel cells (SOFC)

Solid oxide fuel cells use ceramic oxides as the ion conductor. The electrolyte is usually Y_2O_3 stabilized ZrO_2, and the charge carrier is O^{2-} ions. The advantages of this type of fuel cells include flexibility of fuel, little need for reforming, and higher efficiencies. The corrosion problems are minimal due to the use of solid electrolytes. However, the operating temperature is 600 – 1000 °C, so thermal expansion mismatch between the electrolyte and electrodes becomes a critical issue. This limits the type of materials than can be used for cell construction and fabrication.

1.4 PEMFC ISSUES AND CHALLENGES

Proton exchange membrane fuel cells (PEMFC) are promising candidates for vehicular applications because of their high power density, quick startup, and high efficiency. Compared to other types of fuel cells, PEMFCs offer more power per unit volume or weight of the fuel cell. At the heart of a PEMFC or DMFC lies the membrane-electrode assembly (MEA), which basically consists of an ionomer membrane (typically Nafion) sandwiched between two catalyst-coated gas diffusion layers (anode and cathode). In a PEMFC, hydrogen fed through the anode is catalytically dissociated into protons and electrons. Oxygen at the cathode is reduced to oxide ion. The protons travel through the membranes and combine catalytically with the oxide ions to form water. The electrons travel through the external circuit to generate electrical power. The reactions at the anode and the cathode can be summarized as

Anode reaction: $2H_2 \rightarrow 4H^+ + 4e^-$ [1.8]

Cathode reaction: $O_2 + 4\,H^+ + 4e^- \rightarrow 2H_2O$ [1.9]

Overall reaction: $2H_2 + O_2 \rightarrow 2H_2O$ [1.10]

Nevertheless, the conversion of the chemical energy of the fuel in a PEMFC is primarily limited by the slow kinetics of the oxygen reduction reaction (ORR) in the cathode [1, 3, 5, 11]. The ORR involving a four electron transfer is much more sluggish than the hydrogen oxidation reaction (HOR) in a PEMFC. The key component that determines the ORR kinetics is the cathode catalyst. In a practical fuel cell, the above anode and the cathode reactions are catalyzed by Pt dispersed as nanoparticles on a carbon support [11]. Even on high surface area Pt catalyst, the cathode over-potential is several mV. To mitigate the sluggish nature of the ORR kinetics, usually the Pt loading is significantly higher on the cathode side than on the anode side [3,4].

Additionally, present PEMFCs suffer from severe durability issues. One of the biggest concerns is the dissolution of Pt in highly acidic environment. From TEM studies, it has been confirmed that long-term, steady state operation of a PEMFC causes dramatic changes in the particle size distribution and morphology of the Pt electrocatalyst particles [12-16]. Ferriera *et al.* observed nonspherical Pt nanoparticles (in the membrane) along with spherical Pt nanoparticles in the cathode layer which point to dissolution of Pt and subsequent reduction in the ionomer by hydrogen [12,13]. Growth of Pt nanoparticles due to Ostwald ripening during long-term operation is also a major issue as it decreases the available surface area for ORR. In addition to the dissolution of Pt, the carbon support also corrodes. Although, the oxidation of carbon is thermodynamically possible in a fuel cell operating voltage, the reaction is kinetically slow [17-19].

A model by National Renewable Energy Laboratory (NREL) based on high production volume (500,000 units) and status of PEMFC technology in 2005 estimated that 77% of the cost of a PEMFC is due to the electrode with platinum contributing a majority of it [20]. The cost breakup is shown in Fig. 1.2.

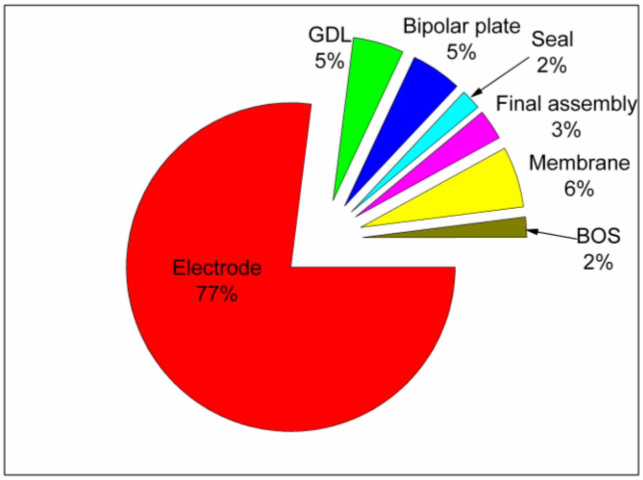

Figure 1.2. Cost analysis of a PEMFC stack ($/kW).

Clearly, for successful commercialization and long-term viability of the PEMFC technology, there is an urgent need to increase the kinetics of ORR and to find alternate non-platinum electrocatalysts with performance similar to or better than that of Pt.

1.5 OXYGEN REDUCTION REACTION (ORR) KINETICS ON PLATINUM

Although the reaction pathways and reaction intermediates for oxygen reduction on noble metals like Pt and Pd are open to debate, the most accepted pathway in acidic medium is presented in Fig. 1.3. In short, the initial step involves the adsorption of molecular oxygen on the surface of the electrocatalysts. The adsorbed oxygen can either follow a two electron transfer process to form hydrogen peroxide, which can undergo further reduction to form water, or a direct four electron reduction of adsorbed oxygen to water.

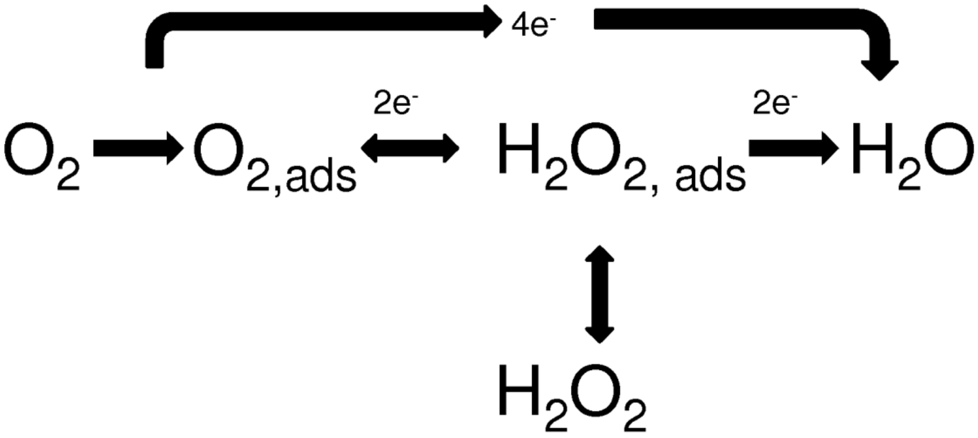

Figure 1.3. Oxygen reduction pathways [21, 22].

The reaction pathways can be written as [23]

Direct reduction:

$O_2 + 4\,H^+ + 4e^- \rightarrow 2H_2O$ $\quad E^0(O_2/H_2O) = 1.23$ V [1.11]

Indirect reduction:

$O_2 + 2H^+ + 2e^- \rightarrow H_2O_2$ $\quad E^0(O_2/H_2O_2) = 0.682$ V [1.12]

followed by

$$H_2O_2 + 2H^+ + 2e^- \rightarrow 2H_2O \qquad E^0(H_2O_2/H_2O) = 1.77\ V \qquad [1.13]$$

or chemical decomposition as

$$2H_2O_2 \rightarrow H_2O + O_2 \qquad [1.14]$$

The pathways depend on adsorbed states and the structure of the surface. For metal electrocatalysts like Pt, different planes show different behavior for oxygen reduction pathways. Usually, for nanoparticle elctrocatalysts, the oxygen reduction reaction follows both the reaction pathways, but the four electron reduction pathway dominates. In the case of non-platinum metals like Au or non metals like carbon, the oxygen reduction reaction in acidic media proceeds via the two electron reduction pathway, leading to the formation of hydrogen peroxide (H_2O_2). The adsorbed state of oxygen is schematically shown in Fig. 1.4, where molecular oxygen can get adsorbed on a metal atom in three different ways [23].

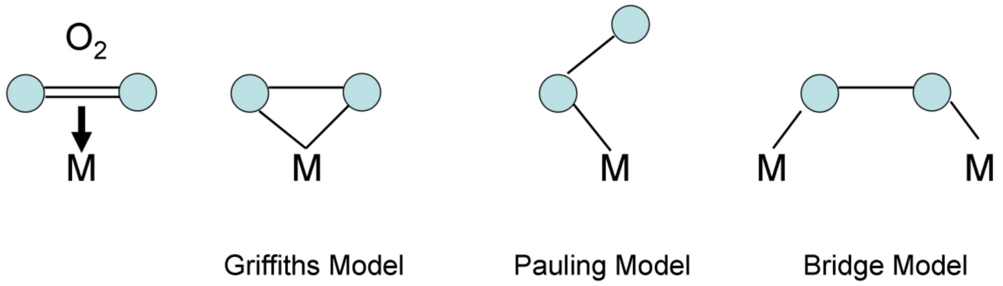

Figure 1.4. Adsorbed states of molecular oxygen [23].

An adsorbed state following the Pauling model favors H_2O_2 while both the Griffith model and the Bridge model favor direct four electron reduction pathway to water. In a fuel cell, the four electron pathway is desirable as the production of hydrogen peroxide leads to decreased utilization of the cathode gas and degradation of the polymer electrolyte membrane.

Among all the noble metals, Pt shows the lowest over-potential for ORR and the reaction proceeds via the four electron route. Thus, Pt is the electrocatalyst of choice for ORR in PEMFC.

1.6 APPROACHES FOR LESS EXPENSIVE ELECTROCATALYSTS

It has been pointed out that for full scale commercialization and deployment of hydrogen fuel cells, multifold increase in the kinetics of ORR or novel non-platinum electrocatalyst is essential. Presently, Pt shows the highest activity for ORR among all elements in acidic media. However, Pt is expensive and over the years different strategies have been employed to mitigate the problem. Some aspects of these are summarized below.

1.6.1 Improving the kinetics of ORR

The development of Pt-based alloy electrocatalysts for ORR can be attributed to United Technologies Corporation (UTC) in 1980s, when several Pt alloys (Pt-V, Pt-Co-Cr, Pt-Co, etc.) were disclosed as ORR electrocatalysts for PAFC with superior activity compared to Pt [24]. Subsequently, a large number of binary, ternary, and quaternary electrocatalysts have been explored and reported. One of the prominent Pt-based alloy catalysts is Pt-Co. Mukhejee *et al.* [25,26] were the first to employ Pt-Co alloy electrocatalysts for ORR in a PEMFC. Along with carbon-supported Pt-Co, several first row transition metals alloyed with Pt such as Pt-Ni, Pt-Mn, Pt-Fe, and Pt-Cr were also explored. Fig. 1.5 shows the IR corrected Tafel plots obtained from fuel cell experiments for the various binary cathode electrocatalysts at 90 ^{o}C. These results indicate much lower over-potential and higher activity for ORR for the alloy electrocatalysts. Among the various catalysts investigated, Pt-Cr shows the highest activity. Since then, a large number of Pt-based alloy systems have been explored as cathode catalysts for PEMFC.

Alloying of Pt with other elements like V, Cr, Fe, Co, Ni, Cu, and Ir have been shown to improve the kinetics of ORR significantly while reducing the cost. Of all the Pt-based alloys, Pt-Co alloys have received maximum attention as almost 2 times higher mass-based activity has been found with Pt-Co alloys compared to Pt [26-41].

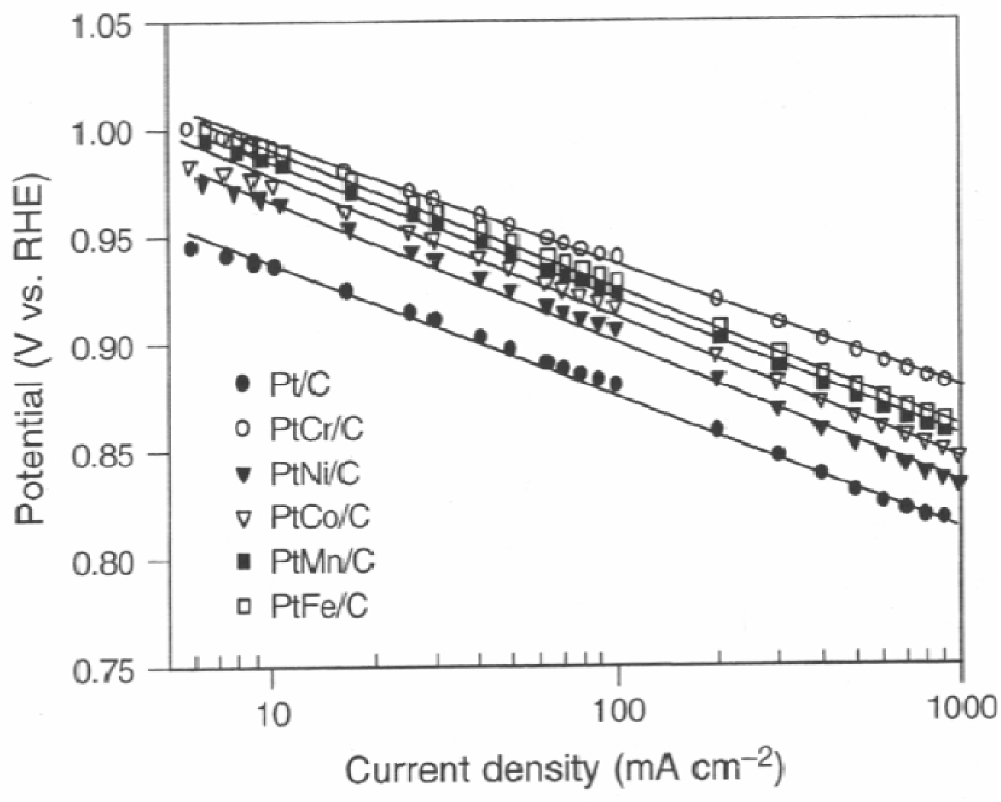

Figure 1.5. Steady-state IR-corrected Tafel plots for the cathodic ORR catalyzed by several binary Pt alloy electrocatalysts at 90 °C and 5 atm pressure. Performance of a Pt/C electrocatalyst is shown for comparison. The electrodes had a metal loading of 0.3 mg cm^{-2} and the loading of the metal on the carbon-supported catalyst was 20 wt%. The humidification temperature for the anode and cathode gas streams was kept at, respectively, 10 and 5 °C above the cell temperature [25,31].

1.6.1.1 Origin of the enhanced activity of the alloy electrocatalysts

The effect of alloying of other transition metals with Pt on the enhancement in activity for ORR has attracted a lot of attention. In the early part of 1980s, several mechanisms were proposed for the enhanced activity such as dissolution of non-noble transition metal in the acidic environment leading to surface roughening and activity increase due to higher proportion of favorable planes and formation of special sites [34-37]. Although the mechanism of enhancement in activity for ORR is still evolving, three effects are usually cited for enhanced activity for ORR.

1.6.1.1.1 Structural and geometric effects

Jalan *et al.* [38] reported that the activity increase for ORR in the case of Pt alloys can be related to Pt-Pt interatomic distance, which would facilitate dissociative adsorption of oxygen by providing favorable sites. Alloying of Pt with smaller transition metal would result in a decreased lattice parameter and consequently smaller Pt-Pt interatomic distance and favor adsorption of molecular oxygen [27, 38-42]. Min *et al.* [42] observed nearly linear increase in specific activity (current density per unit electrochemical active area) with decreasing Pt-Pt bond distance for a series of alloys. It was also observed that the specific activity increases with increasing heat treatment temperature. Additionally, extended X-ray absorption fine structure spectroscopy (EXAFS) studies indicated variations in electronic states upon alloying the transition metals with Pt. Fig.1.6 shows the variation of the specific activity with Pt-Pt interatomic distance measured from X-ray diffraction (XRD) data. However, dissolution of the less noble transition metals under reaction conditions imposes severe limitation to the application of this theory.

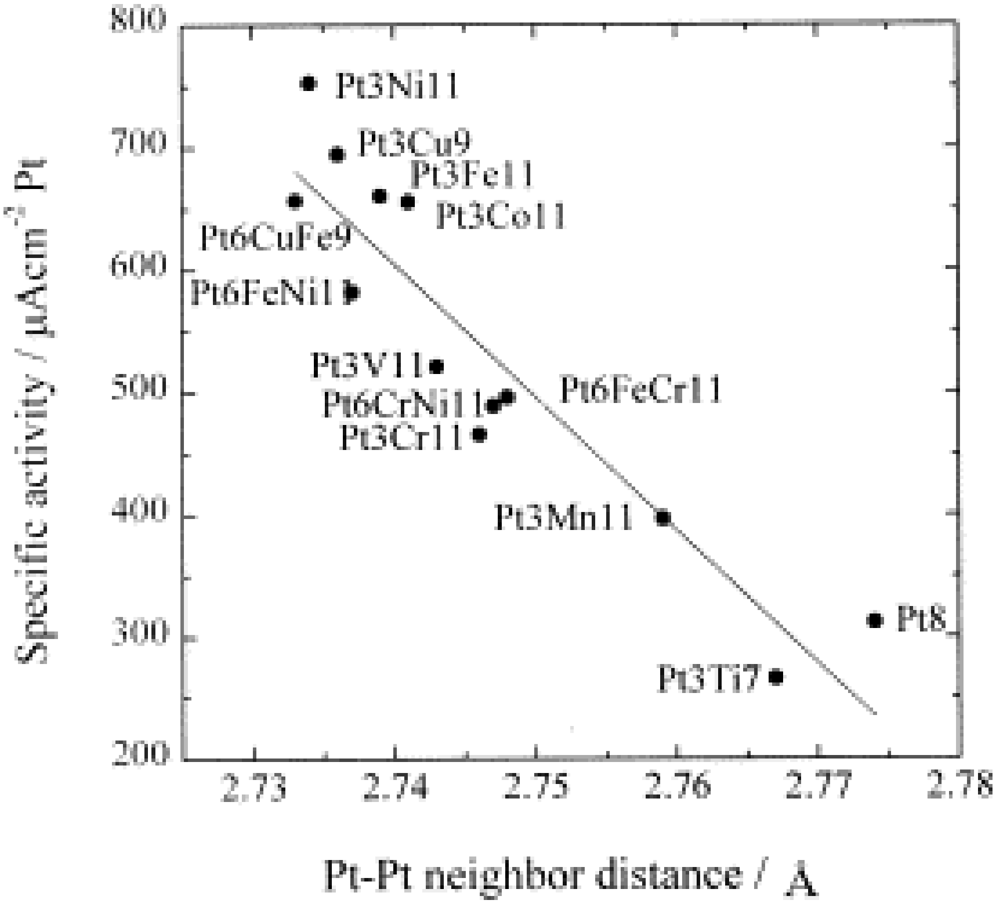

Figure 1.6. Relationship between the Pt–Pt nearest neighbor distance and specific activity [42].

1.6.1.1.2 OH_{ads} inhibition effect

As seen in Fig. 1.4, an increase in the strength of adsorption of O_2 on the metal surface would result in a weakening of the O-O bond and formation of M-O (metal oxygen) bond. However, a stronger M-O bond would inhibit the addition of protons and release of the adsorbed species. Specifically, one of the reaction intermediates that blocks the number of available sites for oxygen reduction is OH^-. Therefore, maximum reaction rates can be achieved if the metal atom binds strongly enough to break the O-O bond, but loosely enough to desorb intermediates like OH^- after the addition of proton. This gives rise to the classic volcano-type plot [43,44].

In the case of platinum, the OH^- adsorption arises from both as an intermediate species during the oxygen reduction reaction as well as from water activation (Pt-OH formation at potentials > 0.75 V *vs* NHE). In addition to blocking active sites on Pt surfaces, OH adsorption also changes the Tafel slope as has been demonstrated by Murthi *et al* [48] in various mixtures of water and trimethylfluro sulphonic acid. Additionally, it was found that Pt-Co and Pt-Fe electrocatalysts show no improvement over Pt at very low water concentration. Thus, it was postulated that the alloy electrocatalysts show improvement in ORR by inhibiting OH^- adsorption. Mukherjee *et al.* [31, 45-49] also observed a shift on the onset potential for Pt-OH formation depending on the nature of the alloy. Moreover, the potential shift observed for OH^- formation is being increasingly cited for the increased activity of the Pt alloy electrocatalysts. In the case of de-alloyed Pt-Cu electrocatalysts with activity for ORR four times higher than that of pristine Pt, a clear shift in the activation potential of water ($Pt + H_2O \rightarrow PtOH + H^+ + e^-$) by several mV was observed [51,52]. Like OH^-, other non-specific anions like chlorides, bromides, iodides, bisulphate/sulphates also adsorb and cause blocking of surface sites for ORR [53-55]. These results in lower kinetic currents as well as change in Tafel slope. Particularly, the observed change in Tafel slope and lower limiting currents in rotating disk electrode (RDE) experiments conducted in O_2 saturated 0.5 M H_2SO_4 has been ascribed to strong bisulphate adsorption [56, 57].

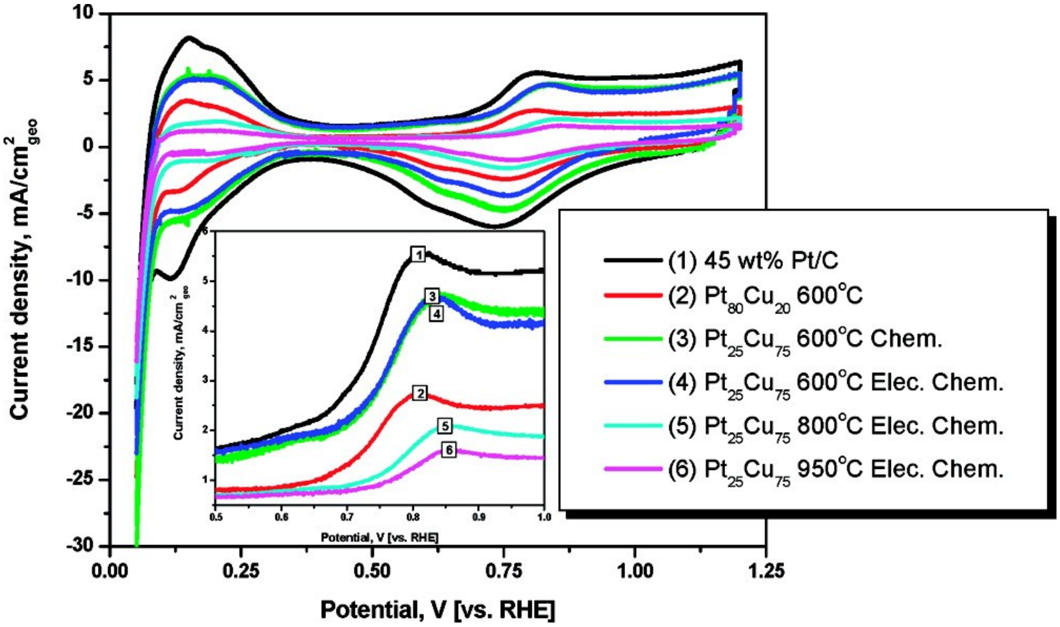

Figure 1.7. Cyclic voltammogram of the chemically/electrochemically activated catalysts. Position of the peak anodic current densities due to oxidation of surface atoms (coverage of hydroxide species) are marked with square symbols in the inset to show the positive shift in water activation potential of the catalysts [52].

1.6.1.1.3 Electronic effect

The formation of d-band vacancies upon alloying plays an important role in the enhancement of ORR activity. Mukherjee *et al.* [26] investigated the electronic effect (d band vacancy/atom) by *in situ* X-ray absorption near edge structure (XANES) and extended X-ray absorption fine structure (EXAFS). It was observed that alloying of Pt with base metal gives rise to d-band vacancies due to differences in electro negativity, and a volcano plot was obtained by plotting the current density *vs* d-band vacancies for various Pt-M (M= Mn, Cr, Fe, Co, and Ni) alloy systems as shown in Fig. 1.8.

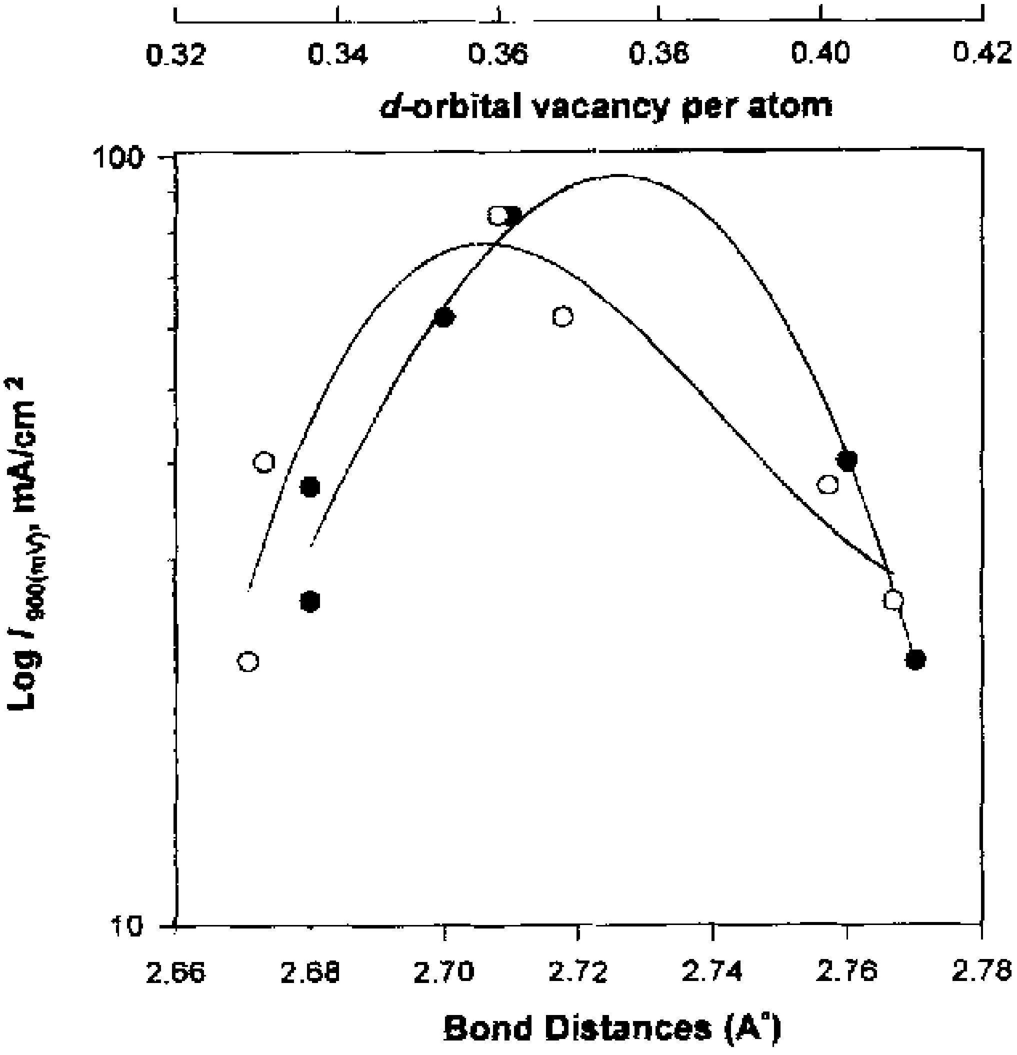

Figure 1.8. Correlation of oxygen electrode performance (Log $i_{900\ mV}$, mA cm^{-2}) of Pt and Pt alloy electrocatalysts in PEMFC with Pt-Pt bond distance {●} and the d-orbital vacancy of Pt {○} obtained from *in situ* XAS [58].

It was suggested that increased d-band vacancy strengthens metal-oxygen bond and thus facilitates O-O bond cleavage. More recently, it has been suggested that the electrocatalytic activity is dependent on the interaction between oxygen 2p states and the metal d states and the position of d-band determines the binding energy of the adsorbate.

The filling of the antibonding states of O_2:2p, which determines the strength of interaction of the metal-oxygen bond, is dependent on the position of the metal d states relative to the Fermi level. A shifting of the metal d states upward relative to the Fermi level results in less filling of antibonding states and a strong metal-oxygen bond facilitating cleavage of O-O bond. On the other hand, if the d-band center is too close to the Fermi level, the strongly adsorbed OH^- limits the availability of free sites. The surface structure as well as the composition of the under layers below Pt skin affects the d band centers and consequently the catalytic activity.

Alloying of a reactive transition metal like Co with Pt causes selective dissolution of the transition metal under reaction conditions. Thus, Pt-Co stoichiometric alloy cannot be directly attributed to increased activity for ORR. However, it has been observed that the surface of the electrocatalysts gets enriched both by dissolution and high temperature annealing [59]. These effects result in a strained Pt skin. Moreover, DFT calculations have shown systematic change in d-band centers on these strained Pt skin surfaces that affects the activity towards ORR [60-62]. A compressive strain leads to a weaker adsorbate-surface interaction and consequently oxygen binds less strongly on Pt skins over Pt alloys than on pure Pt.

1.6.2 Pt monolayers and overlayers on other metals and alloys

The successful use of Pt sub-monolayers on Ru as CO tolerant hydrogen oxidation electrocatalyst has lead to a new class of non-alloyed platinum monolayer electrocatalyst for ORR [63,64]. Deposition of a monolayer of Pt on other metals or alloys allows not only tailoring the electrocatalytic activity for ORR but also decreasing the loading of Pt substantially. This type of electrocatalyst for ORR, consisting of a mixed monolayer of Pt and late transition metal (Ir, Ru, Rh, Re, or Os) on Pd(111) single crystal or on carbon-supported alloy nanoparticles, have been found to offer significantly higher activities [65-72]. Some of these systems showed many fold increase in activity for ORR on a Pt mass-based activity compared to the state-of-the-art Pt electrocatalyst [70]. Although purely by chemical means, it may not be possible to deposit a monolayer of Pt on other substrates, under potential deposition of Cu by electrochemical means and subsequent displacement of Cu by Pt has used to obtain these monolayer electrocatalysts on bulk non-platinum substrates as well as on non-platinum nanoparticles. Significantly, it was also found out that the activity for ORR is greatly influenced by the underlying substrate as shown in Fig. 1.9. These results were among the first direct evidence of influence of substrate on the ORR activity of Pt skin. Strains on the Pt monolayer caused by lattice mismatch have been used to explain some of the observed results. The compressive strains on Pt monolayer over Ir(111), Ru(0001), and Rh(111) causes the oxygen molecule to bind less strongly on Pt surface. However, Pt monolayer on Au (111) introduces an expansive strain. A second effect called ligand effect caused by the differences in reactivity of the elements towards oxygen was also found to play a significant role.

Similar increase in ORR was obtained for a monolayer of Pd deposited on different substrates. As a further extension of this idea, Pt monolayer has also been deposited on Pd-Co alloy “core-shell” nanoparticles and an improvement by 2.5 to 3 times compared to commercial Pt has been obtained [70]. A monolayer of Pt on surface segregated Au-Ni alloy has also shown an improvement of 5-6 times based on total Pt mass based activity [72].

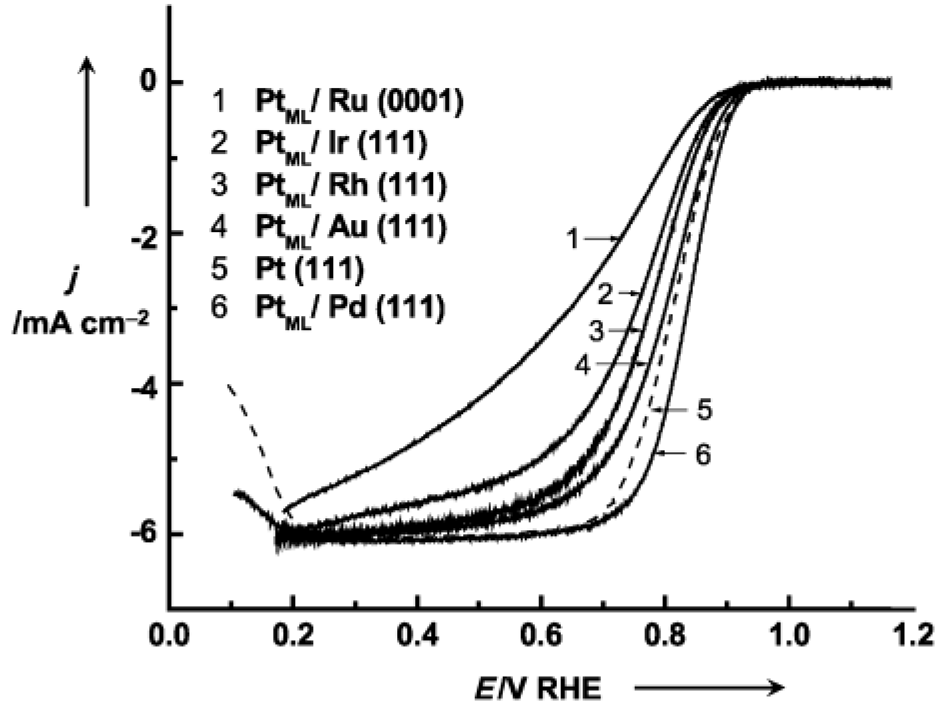

Figure 1.9. Polarization curves for O_2 reduction on platinum monolayers (Pt_{ML}) on Ru(0001), Ir(111), Rh(111), Au(111), and Pd(111) in a 0.1 M $HClO_4$ solution on a disk electrode. The rotation rate is 1600 rpm, and the sweep rate is 20 mV s^{-1} (50 mV s^{-1} for Pt(111)); *j* refers to current density and RHE refers to reversible hydrogen electrode [71].

Recently, other class of electrocatalysts consisting of a Pt shell on Pt-Cu alloy core has been developed by a voltammetric dissolution of Cu from Pt-Cu alloys [51,52]. It has been postulated that after dealloying, the resulting alloy electrocatalyst consists of a Pt-Cu alloy core encapsulated by Pt shell. Additionally, it was postulated that presence of a reactive core modifies the Pt shells and leads to higher activities. The ORR activity of these electrocatalysts were found to be 4 times higher than that of the state-of-the-art commercial Pt electrocatalyst [51,52]. This idea has also been further extended to the Pt-Co-Cu alloy system [73].

1.6.3 Non-platinum electrocatalysts for ORR

The high cost of Pt has mandated search for alternate non-platinum electrocatalysts. The following section briefly describes various non-platinum electrocatalysts that have been developed:

(a) *Transition metal macrocycles:* Jasinski [74] first reported the use of cobalt phthalocyanine for the oxygen reduction reaction. Since then, many transition metal N_4 complexes like porphyrins, phthalocyanines, tetraaznnulares have shown some activity for ORR [75-77]. Among them, Co- and Fe-containing systems have exhibited the highest electrocatalytic activity. It has been postulated that Fe-N_x metal centers on the metal particle are active sites for oxygen reduction. However, a complete mechanism is still elusive. It has been also discovered that combinations of two metal porphyrin complexes like (Fe and Co tetraphenyl porphyrin) give better electrocatalytic activity. However, these metal complexes suffer from stability issues in acidic media [78-81].

(b) *Transition metal carbide and nitrides:* Carbides of several transition metals like tungsten, titanium, and tantalum are active towards oxygen reduction reaction [82-85]. Tungsten carbide in particular has received a lot of attention because it shows platinum-like characteristics in terms of hydrogen chemisorption [86, 87]. However, tungsten carbide is unstable at high potentials. Although, nitrides have not been investigated extensively, some of them, especially titanium nitrides, have shown some activity for ORR [88].

Mo_2N and tungsten nitride have also been investigated and have been found to promote four electron oxygen reduction reaction [89,90].

(c) *Transition metal chalcogenides:* Transition metal chalcogenides have been explored as ORR electrocatalysts for over two decades and are promising materials among non-platinum catalysts [91,92]. Alonso Vante *et al.* [91] were the first to report Ru-Mo-Se ORR electrocatalysts and since then, a large number of compounds of the type MX (M= transition metal atom, X = S, Se, Te) has been identified. However, most of these electrocatalysts use Ru, so their long-term viability is open to debate. Recently Co-based chalcogenides, especially CoS_2, has been reported to promote four electrons transfer with acceptable electrocatalytic activity [93]. More recently, W-Co-Se has been shown to have significant catalytic activity towards ORR, showing the ORR onset potential at 0.755 V vs NHE in 0.5 M H_2SO_4 at 25 °C [94].

(d) *Pd-based electrocatalysts for oxygen reduction reaction:* Pt and Pd are in the same group in the periodic table and the ORR activity of Pd is close to Pt in acidic media. Additionally, like platinum, palladium also promotes four electron pathway for oxygen reduction. Savadogo *et al.* [95] reported significant enhancement in the activity for ORR of bulk Pd-Co alloys made by sputtering Pd and Co compared to that of Pd [95]. More recently, a broad thermodynamic guideline has been proposed by Bard *et al.* [96] to rapidly screen Pd-based alloy systems. The thermodynamic model is based on splitting of O-O bond to form adsorbed oxygen and its electro-reduction to water as shown in equations 1.15 and 1.16:

$$2\,M + O_2 \leftrightarrow 2\,MO \qquad [1.15]$$

$$2\,MO + 4H^+ + 4e^- \leftrightarrow 2\,M + 2\,H_2 \qquad [1.16]$$

where M refers to metal.

Equation 1.15 signifies the formation of M-O bond and cleavage of O-O bond, which is the first step for the reduction of oxygen to water. Since equation 1.15 is a chemical oxidation, a free energy change (ΔG) can be associated with it and the magnitude of ΔG denotes the strength of M-O bond. Equation 1.16 denotes the reduction of M-O in presence of protons and electrons and a standard reduction potential (E^o) can be associated with it (step 2). A plot of the free energy change for the first step (equation 1.15) *vs* the standard reduction potential for the second step (equation 1.16) is shown in Fig. 1.10 for various elements (ΔG and E^0 values were evaluated from Bard *et al.* [97]).

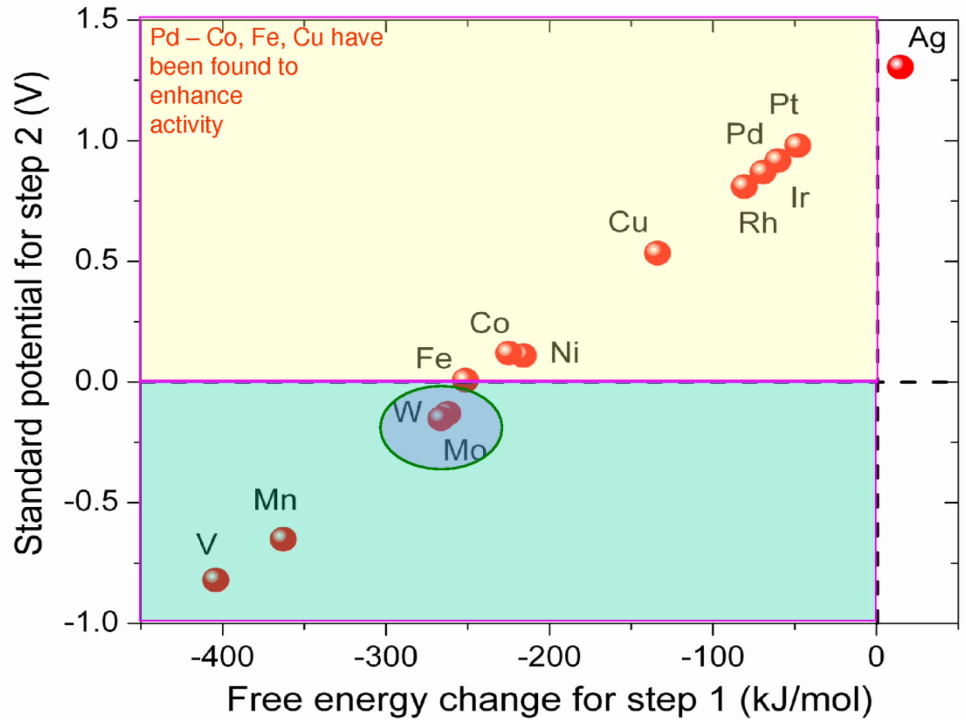

Figure 1.10. Graph of the Gibbs free energy for reaction 1.15 versus the standard potential for reaction 1.16.

The model proposed alloying a metal that can cleave the O-O bond effectively with another metal that can facilitate the reduction of oxide to water as shown in Fig. 1.11 can provide good activity for ORR.

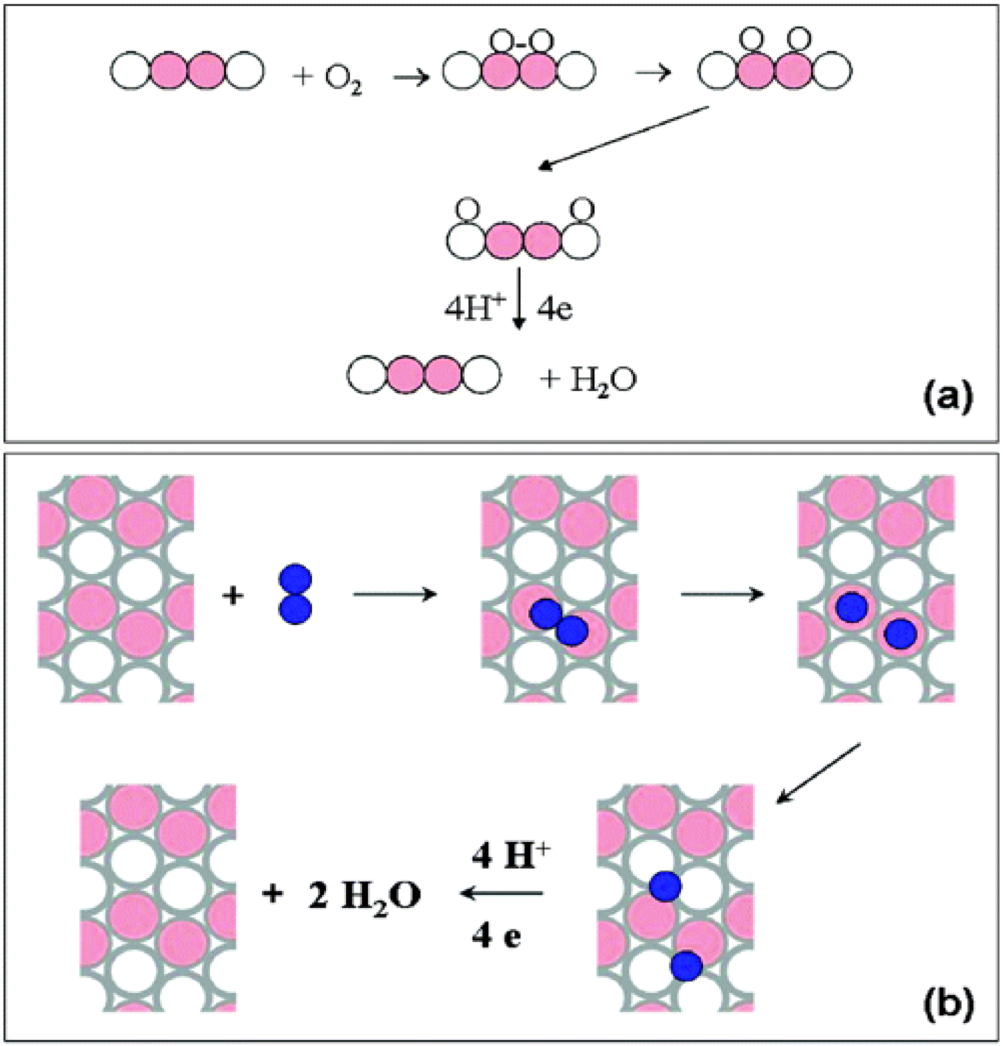

Figure 1.11. (a)Proposed synergetic mechanism for the enhanced electrocatalytic activity on bimetallic surfaces. (b) Top view schematic of the proposed mechanism, with large pink circles representing good oxygen bond cleaving metal atoms (M), grey circles representing metal atoms that reduce adsorbed oxygen efficiently (M‘), and small blue circles representing oxygen atoms [96].

Based on this model and rapid screening of electrocatalysts, a number of binary and ternary electrocatalysts have been identified. Two ternary systems Pd-Co-Au and Pd-Co-Mo have been identified that has activity for ORR close to that of Pt in a fuel cell [98-100]. The ORR activity of Pd-Fe has also been investigated, and it has been reported to be superior to that of commercial Pt [101]. Other binary systems like Pd-Cu, Pd-Ni, Pd-Cr have also been investigated and in some cases, the ORR activity has been reported to be either comparable or superior to that of commercial Pt [102-104].

One of the key advantages of Pd-based ORR electrocatalysts compared to Pt other than its cost is its inactivity to methanol oxidation. This provides a distinct advantage in direct methanol fuel cells (DMFC) as cathodes, where methanol crossover from the anode to the cathode causes a severe drop in potential [104].

1.7 OBJECTIVES OF THIS DISSERTATION

The objectives of this dissertation is to synthesize low-platinum and non-platinum (palladium-based) cathode electrocatalysts for oxygen reduction reaction in a proton exchange membrane fuel cell and to develop an understanding of the effect of the alloying of transition metals on the catalytic activity. In this regard, two new alloy electrocatalysts, Pd-Mo and Pd-W alloys, are synthesized by a novel organometallic decomposition route and systematically investigated for ORR in Chapter 3. The effects of alloying on the activities are examined. Then, a series of low-platinum ternary Pt-Pd-Co alloys are synthesized by a novel microwave-assisted solvothermal method and investigated for ORR in Chapter 4. Finally, a novel approach based on galvanic displacement of copper by platinum and palladium ions to form a "core-shell" structure is developed and investigated for ORR in Chapter 5. All the samples are systematically characterized to obtain information on crystal structure, alloy composition, surface composition, and morphological features by various techniques such as X-ray diffraction (XRD), energy dispersive spectroscopy (EDS) in scanning electron microscope (SEM), X-ray photoelectron spectroscopy (XPS), and transmission electron microscopy (TEM). Electrochemical characterizations such as cyclic voltammetry (CV), rotating disk electrode experiments (RDE), and single cell PEMFC tests are employed to investigate the catalytic activity for ORR.

Chapter 2: Experimental Procedures

In this dissertation, all chemicals were used as received without any further purification. All reagent used were ACS grade.

2.1 MATERIALS SYNTHESIS

The synthesis conditions and procedures to obtain the various electrocatalysts are described in respective Chapters. This Chapter introduces the general materials and electrochemical characterization techniques employed in this dissertation along with a brief overview of the techniques.

2.2 MATERIALS CHARACTERIZATION TECHNIQUES

2.2.1 X-ray diffraction

X-ray powder diffraction is a technique to investigate the phase structure and crystallize size of powdered polycrystalline samples. Since the wavelength of X-rays (~ 1 Å) is comparable to the size of atom, it is ideally suited to determine the crystal structure and the atom positions in a crystalline solid. The method relies on scattering of X-rays by rows of atom. The determination of crystal structure utilizes Bragg's law, which can be modeled as constructive interference by two waves reflected from rows of atoms [105]. Figure 2.1 shows the model of reflection from two planes of atoms in a solid. If the wavelength (λ) of the incident X-rays and the incident angle (θ) are known then the interplaner spacing (d) can be determined by Bragg's equation as

$$2\ d \sin(\theta) = n\lambda \qquad [2.1]$$

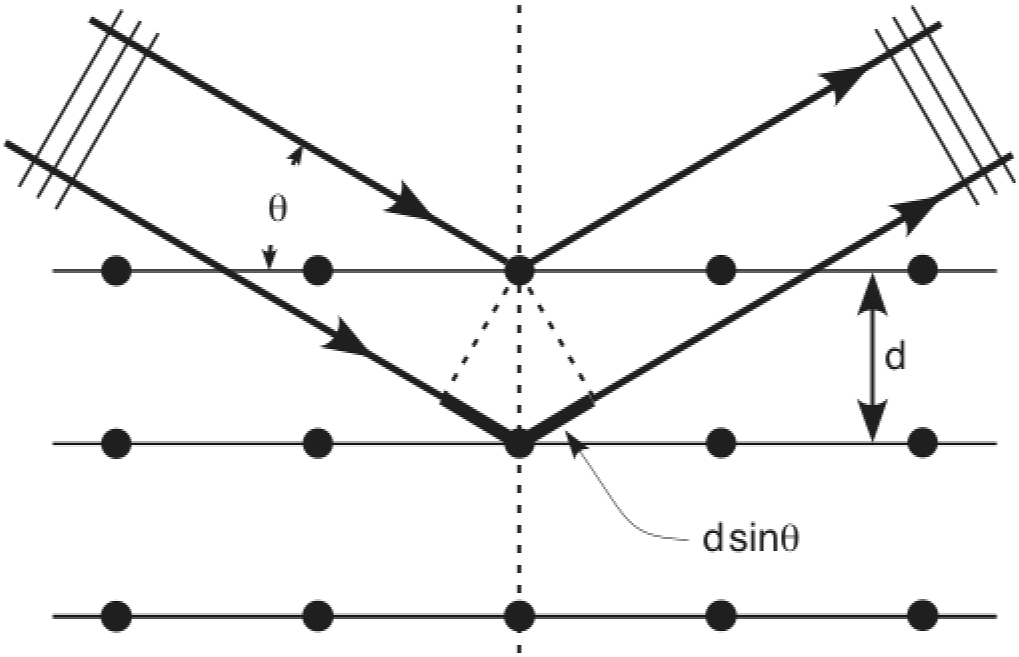

Figure 2.1. Diffraction of X-ray by rows of atoms in a crystal lattice [106].

In this dissertation, the X-ray diffraction studies were carried out with a Philips Model APD 3520 X-ray diffractometer and Cu Kα radiation. Diffraction patterns recorded with variable slit values in the 2θ range of 30° to 90° were used to determine the lattice parameter values of the metal and alloy catalysts synthesized. Profile fitting and lattice parameter evaluation were carried out using the JADE MDI software and the profile fitting parameters are discussed in the respective Chapters.

2.2.2 Energy dispersive spectroscopic analysis (EDS) in scanning electron microscope (SEM)

Energy dispersive X-ray spectroscopy (EDS) was used to determine the atomic ratios of the constituent elements in the electrocatalysts synthesized. The technique relies on measuring the characteristic X-rays energies emitted when a transition of the outer shell electrons to inner shell occurs. A high energy incident electron beam creates an electron hole in the inner shell and causes the transition of an outer shell electron. As the energy of the X-rays emitted is characteristic of the element, an accurate estimation of elemental compositions can be obtained using this technique [107]. EDS analysis was conducted with a JEOL-JSM5610 scanning electron microscope (SEM) having an Oxford instruments EDS attachment. The incident electron energies were kept constant at 20 keV for all the samples.

2.2.3 X-ray photoelectron spectroscopy (XPS)

X-ray photoelectron spectroscopy was used to obtain surface compositions and chemical states of the metals in the electrocatalysts. The technique basically relies on photoelectric effect. When an element with a core level electron binding energy of E_B is illuminated with soft X-ray photon of energy hν, it causes the electrons to be emitted [108,109]. The energy of the emitted photoelectrons is then analyzed by the spectrometer.

The kinetic energy of the emitted photoelectrons ($E_{kinetic}$) can be expressed as

$$E_{kinetic} = h\nu - E_B - \phi \qquad [2.2]$$

where, ϕ is the work function. A change in the chemical state causes a change in the core level binding energy and thus can be detected by XPS measurements. As the soft X-rays do not penetrate more than 10 nm in the sample, this technique is surface sensitive. XPS studies were conducted with a Kratos Analytical spectrometer using monochromatic Al Kα radiation. The compositions of the constituent elements were determined based on the ratio of integrated peak intensities.

2.2.4 Transmission electron microscopy (TEM)

Morphological and particle distribution studies were carried out with a JEOL 2010F high-resolution transmission electron microscope (TEM) operated at 200 keV.

2.3 ELECTROCHEMICAL CHARACTERIZATION TECHNIQUES

2.3.1 Cyclic voltammetry (CV)

Cyclic voltammetry (CV) is a type of potentiodynamic electrochemical technique, where potential is varied linearly with time and the current response of a system is recorded. This technique is similar to linear sweep voltammetry (LSV). However, unlike linear sweep voltammetry, the potential is reversed after a set potential is attained. The inversion gives useful information about the species present in the solution. Generally, the current response of a system is dependent on the concentration of the species, scan rate, diffusion coefficient, and the reaction rate [9,110-115].

However, for adsorbed species, where the reaction happens at the surface as in hydrogen adsorption-desorption on Pt and surface oxide formation-reduction on noble metals, the classical voltammetry equations need to be modified. For a surface species O being reduced to another adsorbed species R with the fraction of surface covered being θ, the electrochemical charge transfer reaction can be written as

$$\underset{(1-\theta)}{O_{ads}} + e^- \rightarrow \underset{\theta}{R_{ads}} \qquad [2.3]$$

If the reaction is fast enough, the Nernst equation for the surface process can be expressed as

$$E = E^0 + \frac{RT}{F} ln\left(\frac{\theta}{1-\theta}\right) \qquad [2.4]$$

where E^0 is the standard thermodynamic potential for adsorbed species, R is the gas constant, T is temperature in Kelvin, and F is the Faraday constant. The current response of such a system will be given by

$$i = FA\frac{\partial\theta}{\partial t} \qquad [2.5]$$

where A is the electrode area. The peak current is given by

$$i_p = \frac{F^2}{4RT}\vartheta A \qquad [2.6]$$

where, υ is the scan rate and the other symbols have their usual meaning [111]. A typical cyclic voltammogram of an adsorbed species obeying Nernst equation is shown in Fig. 2.2.

The CV of polycrystalline noble metals in acidic media shows a more complex behavior in terms of adsorbed species. For a polycrystalline Pt, the current response below 0.4 V vs NHE is due to the adsorption/desorption of hydrogen and the current response above 0.6 V vs NHE is due to hydroxide and oxide formation/reduction. Fig. 2.3 shows the CV of polycrystalline bulk Pt electrode in 0.5 M H_2SO_4.The electrochemical area for Pt or Pt alloys can be estimated using the hydrogen adsorption/desorption charge and using a conversion factor of 210 μC/cm^2.

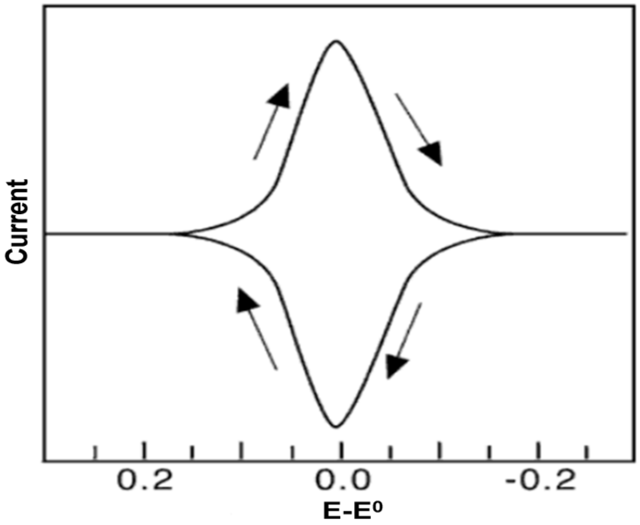

Figure 2.2. CV response of a surface adsorbed species [111].

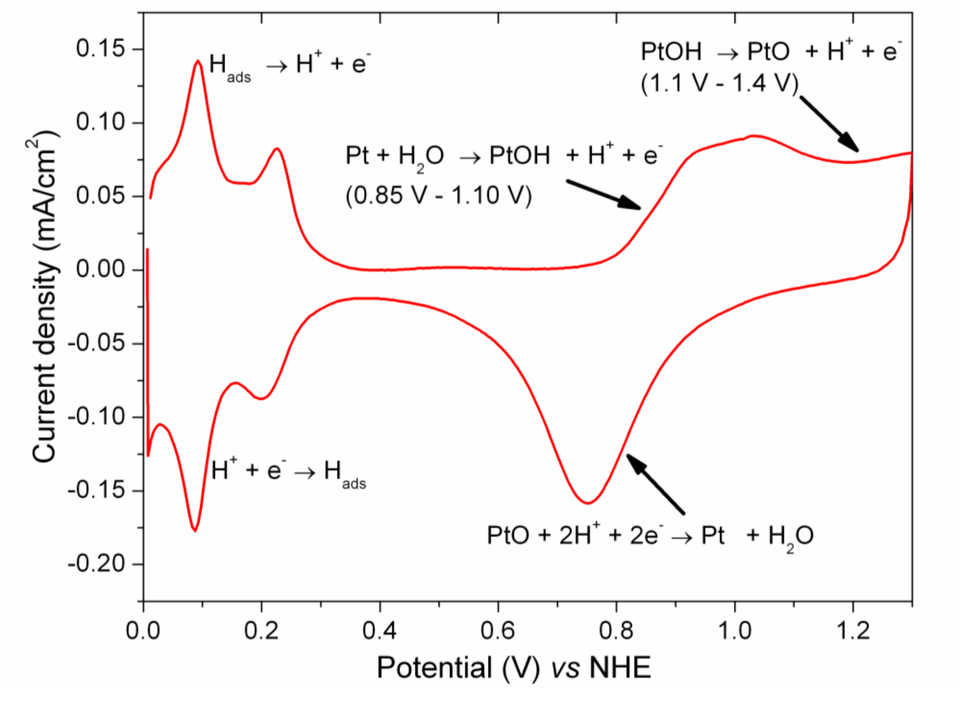

Figure 2.3. Cyclic voltammetry of bulk polycrystalline electrode (5mm dia.) in N_2 saturated 0.5 M H_2SO_4 at 50 mV/s.

In this dissertation, the CV characterizations were carried out with a standard single compartment three electrode cell having a Pt mesh counter electrode and a glassy carbon working electrode. The exact potential range, catalyst loading, analyte solution, scan range, and scan rate used are given in the respective Chapters. Experimental details of CO stripping voltammetry and methanol tolerance tests are also described in the respective Chapters.

2.3.2 Rotating disc electrode (RDE) experiments

Rotating disc electrode (RDE) experiments are hydrodynamic techniques, where the working electrode is rotated to induce forced convection and obtain diffusion limited current (i_l) [9]. The limiting current is a function of the rotation speed and is given by Koutecy-Levich equation as

$$i_l = 0.62nFAD^{\frac{2}{3}}\gamma^{\frac{-1}{6}}C_o\omega^{\frac{1}{2}} \qquad [2.7]$$

where, i_l is the limiting current in A, n is the total number of electrons transferred, F is the Faraday constant (96485 C mol^{-1}), A is the area of the electrode, D is the diffusion coefficient of the species in cm^2 s^{-1}, C is the concentration in mol cm^{-3}, γ is the kinematic viscosity in cm^2 s^{-1}, and ω is the rotation rate in rads^{-1}. The determination of i_l
allows an easy evaluation of the kinetic currents as

$$\frac{1}{i} = \frac{1}{i_l} + \frac{1}{i_k} \qquad [2.8]$$

Additionally, a plot of $1/\omega^{1/2}$ and $1/i_l$ yields a straight line that gives information on the total number of electrons transferred. Figure 2.4 shows such a plot obtained for bulk polycrystalline Pt electrode in 0.5 M H_2SO_4.

RDE experiments were conducted with a glassy carbon disk electrode (5 mm dia.) mounted onto an interchangeable RDE holder (Pine Instruments, USA) in O_2 saturated 0.5 M H_2SO_4 (solutions prepared from Fisher Scientific high purity Optima grade 18 M H_2SO_4) at room temperature. Before each experiment, the glassy carbon electrode was polished to a mirror-like finish with 0.05 μm alumina (Buehler). For most experiments, the rotation rate of the electrode was fixed at 1600 rpm and the potential was scanned at 5mV/s. The catalyst layer preparation and loading are described in the respective Chapters.

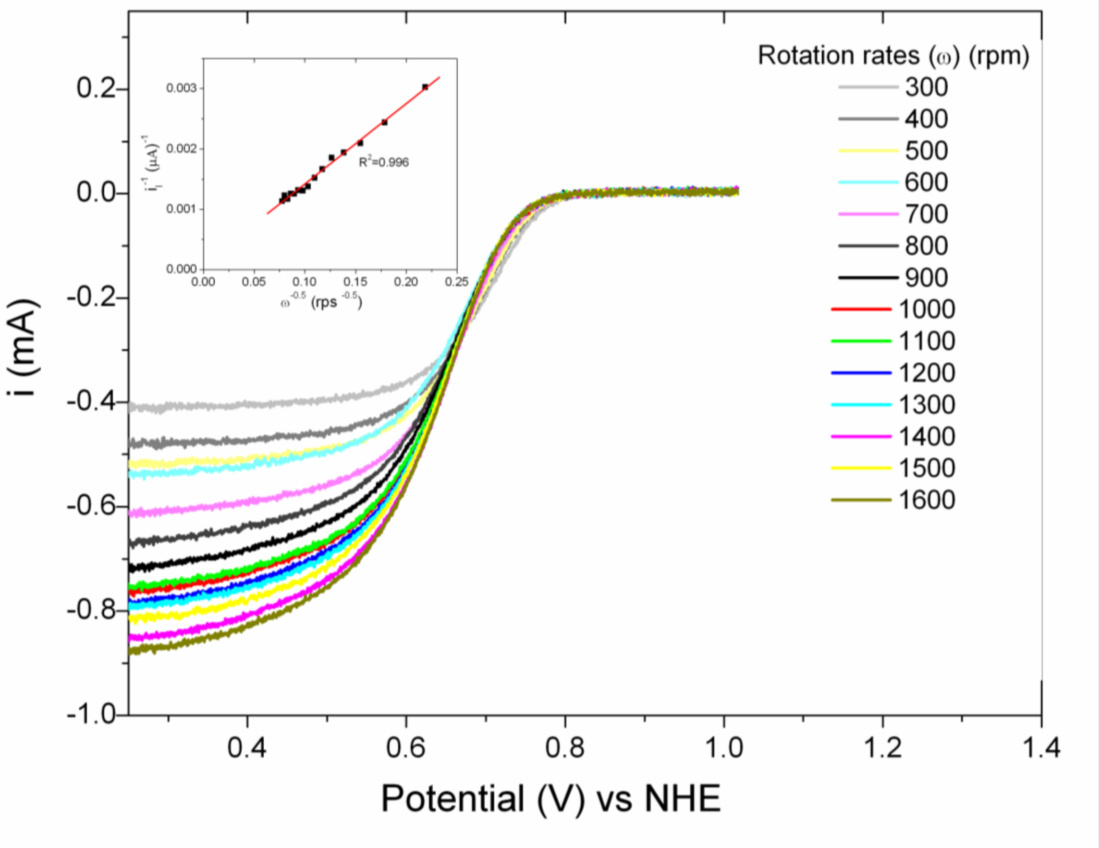

Figure 2.4. Hydrodynamic polarization curves for bulk platinum electrode (5mm dia.) obtained in 0.5 M H_2SO_4 at various rotation rates. The inset shows the variation of 1/il with 1/√ω.

2.3.3 Single cell proton exchange fuel cell (PEMFC) experiments

The electrochemical performances of the electrocatalysts were evaluated with a commercial fuel cell test system (Compucell GT, Electrochem Inc.) using a single cell fixture having an active area of 5 cm^2 (Fig. 2.5). The experimental results were collected under steady-state conditions after at least 6 hours of operation. The catalyst layer preparation is described in the respective Chapters.

Figure 2.5. Single cell proton exchange membrane fuel cell test station.

Chapter 3: Pd-based alloy electrocatalysts Pd-M (M = Mo,W)

3.1 INTRODUCTION

As discussed in section 1.6.3, various non-platinum electrocatalysts for oxygen reduction reaction (ORR) have been widely investigated. Among them, Pd-based alloys form a separate class of noble metal-based electrocatalysts, which are active for ORR. Although palladium by itself is active for ORR in a fuel cell, the over-potential is several mV. Additionally, electro-dissolution of Pd in acidic media at high potential is a concern [116-130]. The electro-dissolution of Pd commences from 0.7 V *vs* NHE and is more pronounced than that for either Pt or Au [119].

Recently, alloying of Pd with other elements like Fe, Co, and Ti has become appealing as they offer high catalytic activity for ORR. Thus, suitable Pd-based alloy electrocatalysts offer tremendous advantages as the cost of palladium is one-fifth of the cost of platinum. Moreover, ternary alloys such as $Pd_{70}Co_{20}Mo_{10}$ and $Pd_{70}Co_{20}Au_{10}$ have been found to exhibit good catalytic activity for ORR along with a high tolerance to methanol that may crossover from the anode to the cathode through the membrane [95-99]. However, while the catalytic activity of the binary Pd-M (M = Cr, Co, Fe, Ni, and Cu) systems for ORR has been investigated no data are available on the binary Pd-Mo or Pd-W systems [95-99, 101-104]]. Cr, Mo, and W belong to group 6A elements of the Periodic Table, are equally resistant to oxidation, and form insoluble oxides, so alloying of Pd with them could enhance the durability while offering good catalytic activity.

However, reduction of both Mo and W from respective inorganic salts is challenging because of their propensity to form oxides in an aqueous media. This Chapter demonstrates a novel synthesis scheme for simultaneous reduction of Pd and Mo or and W to obtain carbon-supported $Pd_{100-x}Mo_x$ ($0 \leq x \leq 40$) and $Pd_{100-y}W_y$ ($0 \leq y \leq 30$) electrocatalysts. Additionally, the as-synthesized Pd-Mo and Pd-W samples are heat treated at 300 to 900 ^{o}C in flowing H_2 to investigate the effect of alloying on the electrocatalytic activity for ORR. After heat treating at various temperatures, the Pd-Mo and Pd-W nanoparticles are characterized by XRD, TEM, EDS, XPS, cyclic voltammetry, and electrochemical polarization measurements in rotating disc experiments and single cell PEMFC for ORR.

3.2 EXPERIMENTAL

3.2.1 Synthesis and characterization of Pd-Mo and Pd-W alloy electrocatalysts

The Pd-M (M = Mo, W) electrocatalysts were synthesized using an organometallic decomposition method as shown in Fig 3.1. Briefly, 200 mg of carbon-supported $Pd_{100-x}Mo_x$ ($0 \leq x \leq 40$) and $Pd_{100-y}W_y$ ($0 \leq y \leq 30$) catalysts with 20 wt. % metal loading were synthesized by refluxing required amounts of palladium acetylacetonate, molybdenum carbonyl solution (0.00248 g $Mo(CO)_6$ per mL of o-xylene) or tungsten carbonyl solution (0.00319 g $W(CO)_6$ per mL of o-xylene) , and Vulcan XC-72R carbon black (Cabot Corp.) in 50 mL of o-xylene for 12 h. The reaction mixture was then cooled to room temperature, filtered, washed repeatedly with o-xylene, and dried overnight in an oven. The carbon-supported Pd-Mo and Pd-W catalysts thus obtained were then heat treated at 300, 500, 700, 800, and 900 ^{o}C for 2 h in a flowing H_2 atmosphere. For a comparison, 200 mg of carbon-supported Pt catalyst with 20 wt % metal in carbon was also synthesized by refluxing a required amount of platinum acetylacetonate with 0.106 g of 1,2-hexadecanediol as a reducing agent and Vulcan XC-72R carbon black in 50 mL of o-xylene. The carbon-supported Pt catalyst was not, however, subjected to any post heat treatment.

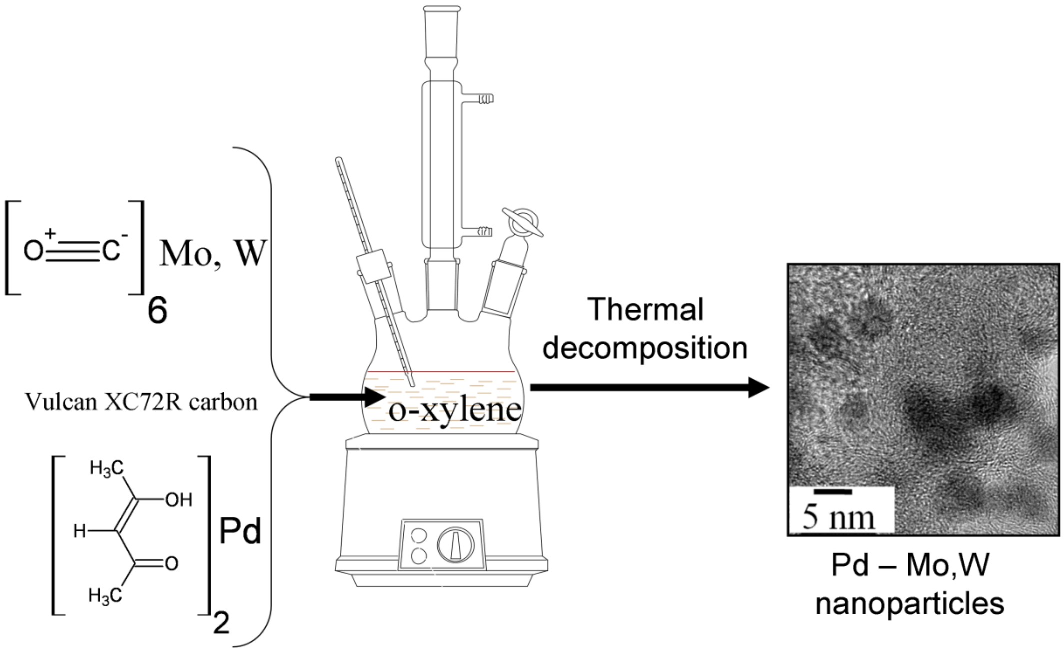

Figure 3.1. Synthesis scheme for carbon-supported Pd-Mo and Pd-W catalysts.

The samples were all characterized by XRD and the metal ratio in the synthesized samples were assessed by EDS. Morphological and particle distribution studies were carried out with high-resolution TEM and surface characterizations were carried out with XPS as described in Chapter 2.

CV characterizations were carried out with a standard single compartment three electrode cell having a Pt mesh counter electrode, a glassy carbon (3mm dia.) working electrode, and a saturated calomel reference electrode (SCE), employing a Voltalab PGZ 402 potentiostat (Radiometer Analytical). In a typical experiment, 5 mg of the carbon-supported catalyst in 1 mL of isopropyl alcohol was ultrasonicated until a dark homogeneous dispersion was formed. 5 μL of the dispersion was drop casted onto the glassy carbon electrode to give an effective carbon-supported catalyst loading of 25 ± 1 μg, and additionally dropping 2 μL of 5 wt. % Nafion solution (Electrochem Inc.) to form a thin film over the catalyst. The CV experiments were conducted in N_2 purged 0.5 M H_2SO_4 at a scan rate of 20 mV/s between -0.242 and 1.1 V (*vs* saturated calomel) at ambient conditions. Before recording the voltammograms, the catalyst surface was cleaned by cycling once between -0.242 and 1.1 V (*vs* saturated calomel).

To estimate the active surface area of the electrocatalysts, CO stripping voltammetry was performed on as-synthesized Pd_{100}, $Pd_{90}Mo_{10}$ and Pd_{100} after heat treatment at 900 ^{o}C, and $Pd_{95}W_5$ after heat treatment at 800 ^{o}C. 2 mg of carbon-supported electrocatalysts was dispersed in 1mL of water and 1 mL of 0.15 wt% Nafion solution till a dark suspension was obtained. 5mL of the suspension was drop casted onto a 3 mm dia. glassy carbon microelectrode to obtain a metal loading of 1 μg. To clean the impurities from the electrocatalyst surface, the potential was cycled 10 times between 0.0 and 1.3 V vs NHE in N_2 saturated 0.5 M H_2SO_4. Thereafter, CO was adsorbed for 0.5 h, maintaining the potential at 0.1 V vs NHE. Subsequently, the solution was purged again with N_2 and the potential was scanned from 0.1 to 1.3 V vs NHE. The CO stripping charge was calculated after background subtraction and a conversion factor of 420 μC/cm^2 was used to estimate the electrochemical active surface area.

Rotating disk electrode (RDE) experiments were conducted with a glassy carbon disk electrode (5 mm dia.) mounted onto an interchangeable RDE holder (Pine Instruments, USA) in O_2 saturated 0.5 M H_2SO_4. A Pt mesh and saturated calomel electrode (SCE) were used, respectively, as counter and reference electrodes. All potentials, however, are reported with respect to NHE. Before each experiment, the glassy carbon electrode was polished to a mirror-like finish with 0.05 μm alumina (Buehler). In a typical experiment, 1 mg of carbon-supported catalyst was ultrasonicated with 0.5 mL isopropyl alcohol and 0.5 mL of 0.15 wt. % Nafion solution (diluted from 5 wt. % Nafion solution by adding ethanol), 20 μL of the aliquot was drop casted onto the glassy carbon electrode, and dried in air to obtain a catalyst loading of 20.37 μg metal/cm^2. The catalyst surface was cleaned by cycling 10 times between -0.242 and 1.1 V (*vs* SCE) before the hydrodynamic polarization curves were recorded. The potential was scanned from 1.0 to 0.3 V *vs* NHE.

For fuel cell tests, the catalyst ink prepared by ultrasonicating required amount of the carbon-supported catalyst, isopropyl alcohol, water, and 40 wt. % Nafion was sprayed on to the top of a commercial gas diffusion layer (BASF) (2.5cm × 2.5cm), followed by drying in air at 90 ^{o}C. The catalyst loading was kept at 0.4 mg/cm^2 both for the anode and the cathode in PEMFC. After spraying the required amount of the catalyst, 50 mg of 5 wt. % Nafion solution was sprayed for better adhesion between the membrane and the catalyst coated gas diffusion layer. The membrane electrode assemblies (MEA) for PEMFC were made by sandwiching Nafion 112 membrane between the anode and cathode by hot-pressing at 140 ^{o}C for 2 min at 2500 psi (172 bar) in a Carver temperature controlled hot-press. The fuel cell testing was carried out at an operating temperature of 40 ^{o}C with hydrogen and oxygen pressures of, respectively, 10 psig (0.689 bar) and 12 psig (0.827 bar) and the humidifier temperature was same as the cell temperature. The gas flow rates were 0.2 L/min for H_2 and 0.4 L/min for O_2. The flow of H_2 and O_2 was varied with load as 0.022 L/min/A and 0.055 L/min/A respectively. The fuel cell (2.5 cm × 2.5 cm active area) was run for at least 6 h before the polarization curves were recorded.

3.3 Results and Discussions

3.3.1 Pd-Mo system

Figure 3.2 compares the XRD patterns of the carbon supported $Pd_{100-x}Mo_x$ ($0 \leq x \leq 40$) catalysts after heat treating at various temperatures. The reflections are characteristic of a face-centered cubic lattice. Additionally, no shifts in the positions of the reflections of $Pd_{100-x}Mo_x$ are seen compared to those of Pd even after heating at 900 ^{o}C due to the similar atomic sizes of Pd and Mo. Although, the formation of a solid solution alloy between Pd and Mo could not be established from the XRD data alone, the Pd-Mo phase diagram suggests that the formation of a face centered cubic solid solution up to 33 atom % Mo and a two-phase region consisting of a Pd-rich face centered cubic phase and a Mo-rich body centered cubic phase beyond 33 atom % Mo at 900 ^{o}C. It can be observed that, while no impurity phases are seen at 700 ^{o}C, reflections corresponding to the Mo_2C impurity phase are seen after heat treating $Pd_{60}Mo_{40}$ at 900 ^{o}C. However, no Mo_2C phase is seen in the case of $Pd_{70}Mo_{30}$ even after heat treating at 900 ^{o}C, suggesting the formation of single phase solid solution up to about 30 atom % Mo after annealing at 900 ^{o}C, which is consistent with the published phase diagram data [131]. It is possible that molybdenum may be present as an oxide or as unalloyed amorphous Mo after heating at 700 ^{o}C in the case of $Pd_{60}Mo_{40}$ and becomes reduced and partly alloyed on heating at 900 ^{o}C.

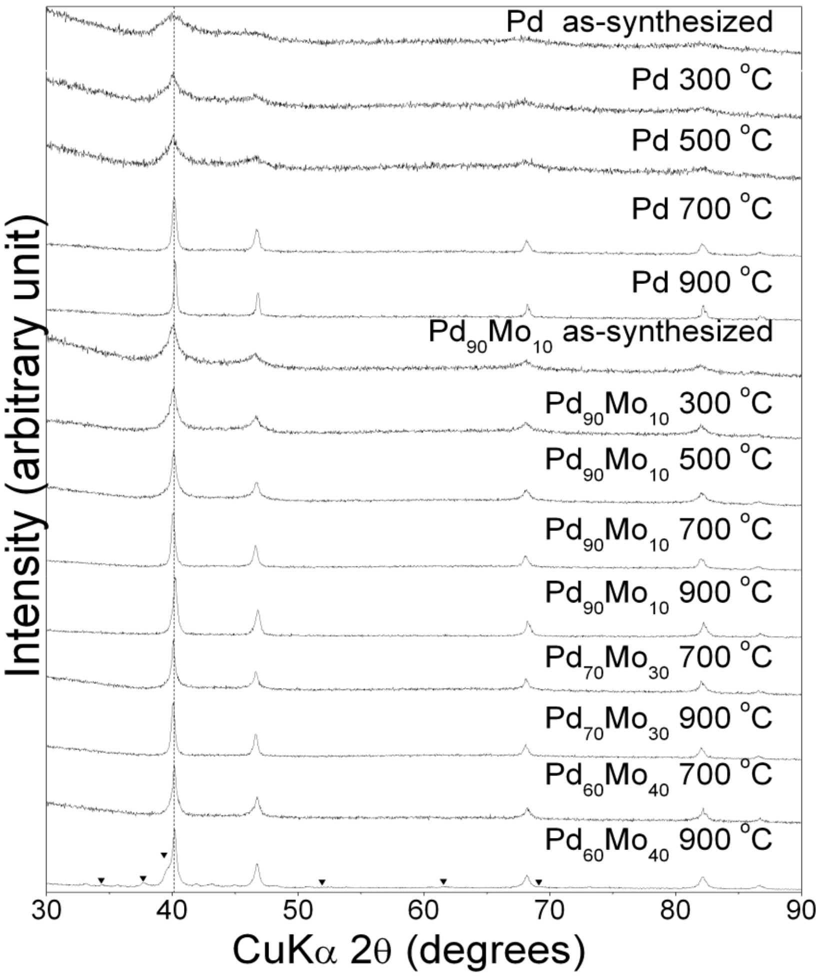

Figure 3.2. X-ray diffraction patterns of Pd, $Pd_{90}Mo_{10}$, $Pd_{70}Mo_{30}$, and $Pd_{60}Mo_{40}$ after heat treating at various temperatures. The dotted line refers to the expected position of the (111) reflection of Pd. The reflections marked with * in $Pd_{60}Mo_{40}$ after heat treating at 900 ^{o}C refer to the Mo_2C impurity phase (PDF # 97-005-9391).

Figures 3.3 and 3.4 compare the TEM images of the as-prepared and 900 °C heat treated Pd and $Pd_{90}Mo_{10}$ samples. The corresponding particle size distribution obtained using ImageJ software is also given in Figs. 3.3 and 3.4. The as-prepared $Pd_{90}Mo_{10}$ shows a broader size distribution centered around 5.6 nm compared to that of Pd that is centered around 4.5 nm. While most of the as-prepared $Pd_{90}Mo_{10}$ nanoparticles show a polyhedral shape as evident from the inset in Fig. 3.3, the Pd nanoparticles show spherical shape. However, on heating at 900 °C, the polyhedral $Pd_{90}Mo_{10}$ nanoparticles become spherical with a significant increase in size as seen in Fig. 3.4.

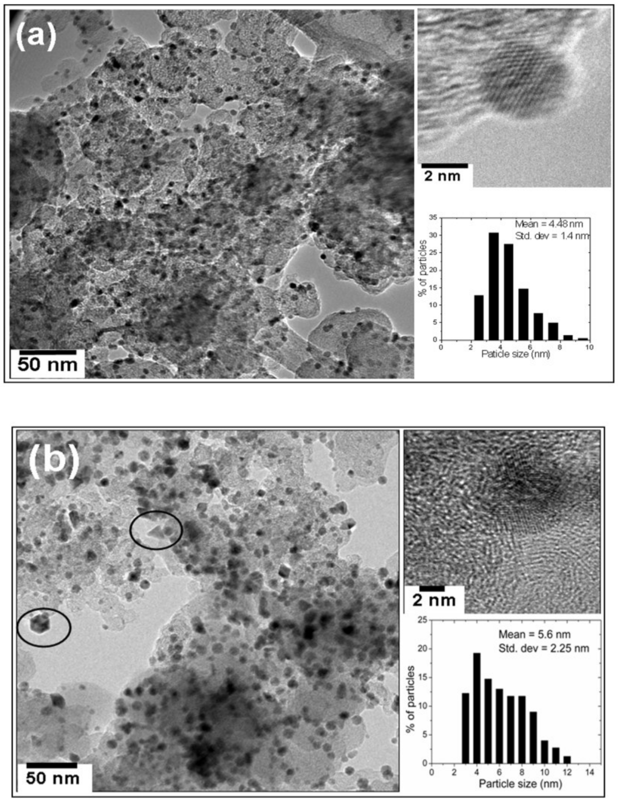

Figure 3.3. TEM images and particle size distributions of as-synthesized (a) Pd and (b) $Pd_{90}Mo_{10}$.

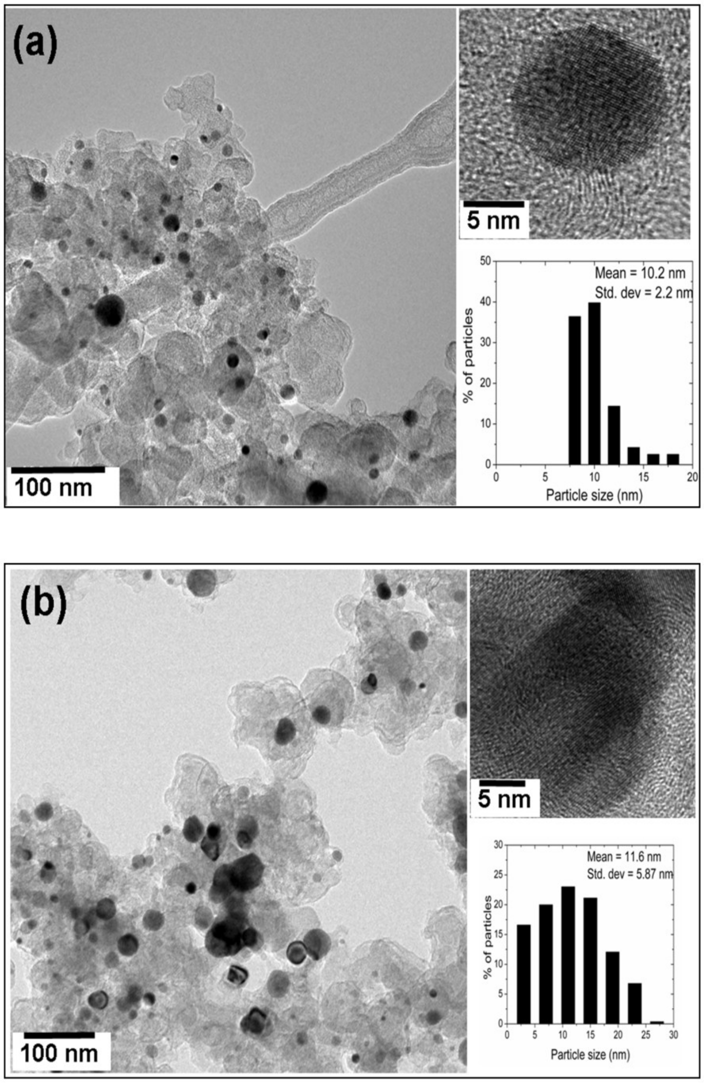

Figure 3.4. TEM images and particle size distributions of as-synthesized (a) Pd and (b) $Pd_{90}Mo_{10}$ after heat treatment at 900 °C.

Figures 3.5 (a) - (c) compares the XPS data of Pd and $Pd_{90}Mo_{10}$ after heat treating at 900 °C. The profiles have been fitted with a mixture of Gaussian and Lorentzian profiles. The profile of Pd for both Pd and $Pd_{90}Mo_{10}$ after heat treatment at 900 °C suggest presence of Pd both as metal (Pd^0) having a binding energy of Pd 3d $_{5/2}$ = 335.3

eV and as oxides (Pd^{2+} and Pd^{4+}) having higher binding energy. Additionally, it can be observed that the Pd $3d_{5/2}$ binding energy increases by 0.5 eV in $Pd_{90}Mo_{10}$ compared to that in Pd after correcting for charging, suggesting the incorporation of Mo into the Pd lattice and the chemical shift can be associated with transfer of electrons from Pd to Mo. XPS analysis of $Pd_{90}Mo_{10}$ indicated a surface composition of 90.8 : 9.2, which is close to the nominal composition. Additionally, XPS surface composition analysis suggests that there is no surface segregation of Mo on Pd, which is agreement with the theoretical calculation by Ruban *et al* [133].

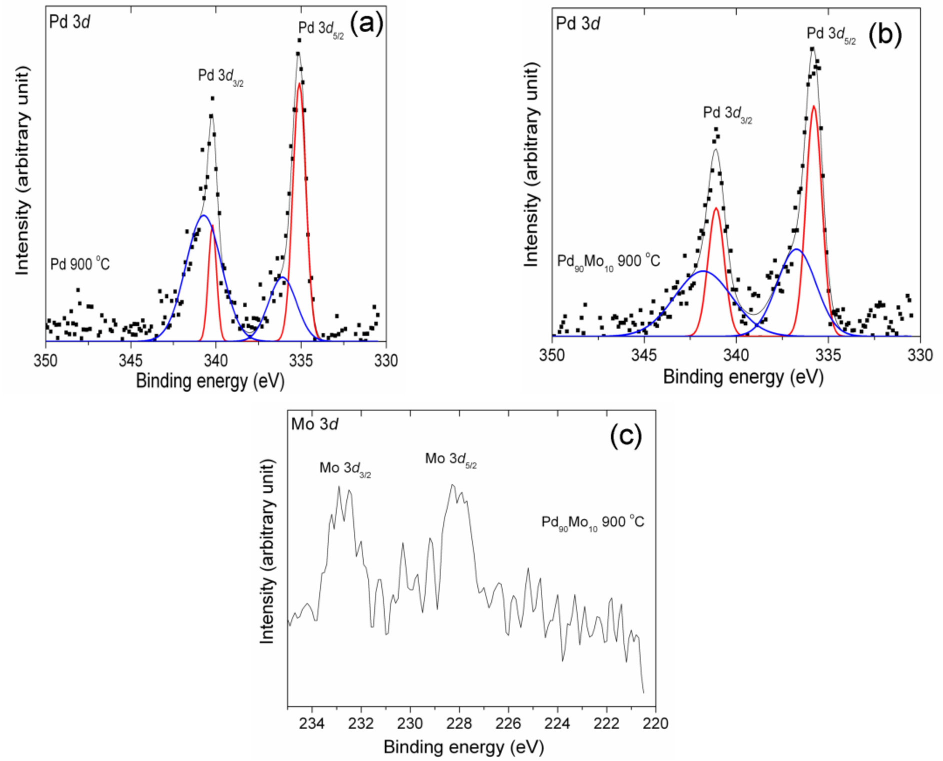

Figure 3.5. X-ray photoelectron spectra of Pd and $Pd_{90}Mo_{10}$ after heat treating at 900 °C. (a) Pd 3d core level in Pd (b) Pd 3d core level in $Pd_{90}Mo_{10}$ (binding energy shifts from 335.3 eV in Pd to 335.8 eV in $Pd_{90}Mo_{10}$), and (c) Mo 3d core level in $Pd_{90}Mo_{10}$.

Figure 3.6 compares the cyclic voltammograms at 1st and 10th cycle of the as-prepared carbon-supported Pd, $Pd_{90}Mo_{10}$, and $Pd_{80}Mo_{20}$ catalysts. As seen in Fig. 3.6(a), the Mo incorporated samples show higher peak current density corresponding to the cathodic peak at the surface oxide reduction region, indicating an enhanced electrochemical activity compared to Pd. Although no direct measurement of the electrochemical surface area are available in the literature as the coverage of hydrogen on Pd is not a monolayer, the higher peak area in the hydrogen desorption region for the Mo incorporated samples compared to that of Pd suggests higher electrochemical active surface area for the Pd-Mo samples. The peak current density values for the surface oxide reduction (cathodic) peak are almost the same for both $Pd_{90}Mo_{10}$ and $Pd_{80}Mo_{20}$ and the peak potential is shifted by 13 mV to the left. Moreover, the samples containing Mo such as $Pd_{90}Mo_{10}$ and $Pd_{80}Mo_{20}$ showed increased resistance to water activation reaction, as shown in equation 3.1 below, compared to Pd and the potential shifted by almost 0.5 V.

$$Pd + H_2O \rightarrow PdOH + H^+ + e^- \qquad [3.1]$$

However, after 10 cycles, there is a substantial drop in the peak current density (or active surface area) for both Pd and the Mo incorporated samples although the drop is less severe for the Mo incorporated samples as shown in Fig. 3.6 (b). The loss of activity has been explained to be due to the formation and incipient growth of PdO and $Pd(OH)_2$ films and subsequent dissolution of Pd as Pd^{2+} in acidic solutions in the potential range of 0.5 - 1.3 V *vs* SHE [116]. On heat treating at 300, 500 °C, and 700 °C, no significant change was noticed in the stability although the peak currents decrease due to an increase in particle size and decrease in surface area.

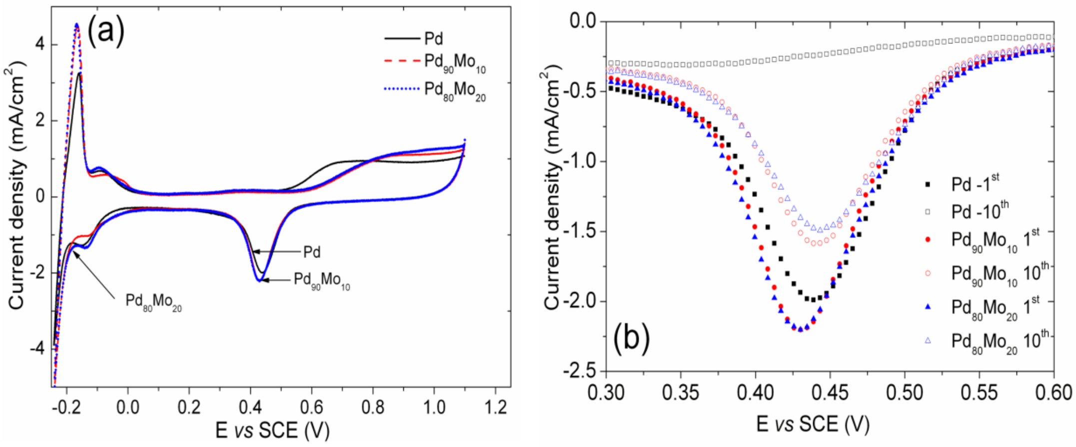

Figure 3.6. Comparison of the (a) cyclic voltammograms and (b) surface oxide reduction (cathodic) region of the voltammograms after 1st and 10th cycles of as-synthesized Pd, $Pd_{90}Mo_{10}$, and $Pd_{80}Mo_{20}$.

Figure 3.7 compares the voltammograms of the carbon-supported Pd, $Pd_{90}Mo_{10}$, and $Pd_{80}Mo_{20}$ catalysts after heat treatment at 900 ^{o}C. The surface oxide reduction (cathodic) peak area increases with Mo incorporation, reaches a maximum at 10 atom % Mo, and then decreases with increasing Mo content. The peak current density for the 900 ^{o}C $Pd_{90}Mo_{10}$ (1.3 mA/cm^2) is close to that obtained for the as-synthesized Pd (1.9 mA/cm^2) despite a significant increase in particle size. More importantly, the inset in Fig. 3.8 reveals that the $Pd_{90}Mo_{10}$ sample shows excellent stability (durability) during cycling. Pd heat treated at 900 ^{o}C also shows excellent stability, but it has much reduced surface oxide reduction (cathodic) peak area as shown in the inset in Fig. 3.7. Moreover, no change in the water activation potential for the reaction given in equation 3.1 was observed for $Pd_{90}Mo_{10}$ after heat treatment at 900 ^{o}C as can be seen in Fig. 3.8.

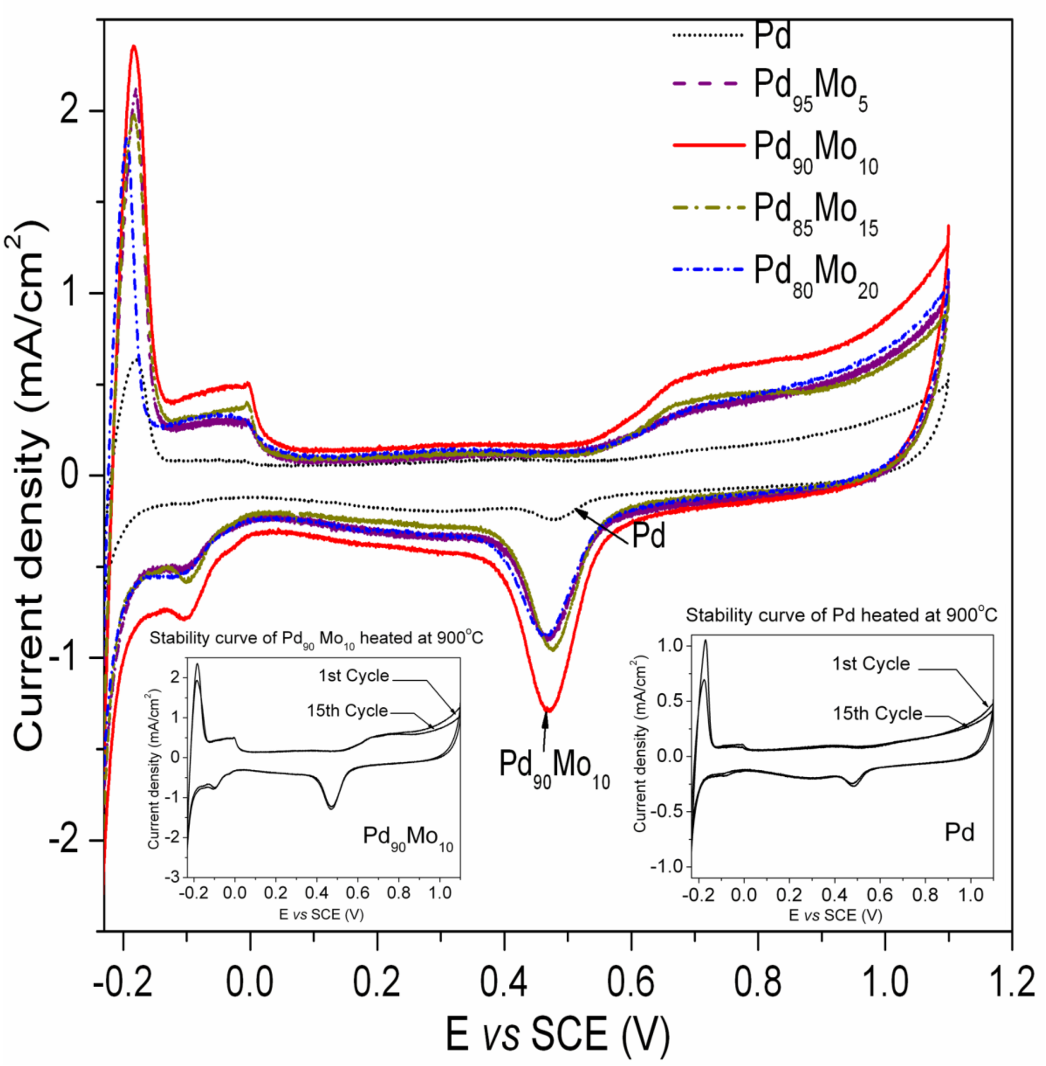

Figure 3.7. Cyclic voltammograms of Pd, $Pd_{95}Mo_5$, $Pd_{90}Mo_{10}$, $Pd_{85}Mo_{15}$, and $Pd_{80}Mo_{20}$ after heat treatment in flowing H_2 at 900 °C. The bottom insets compare the oxygen reduction region of the voltammograms at the 1st and15th cycles for $Pd_{90}Mo_{10}$ and Pd.

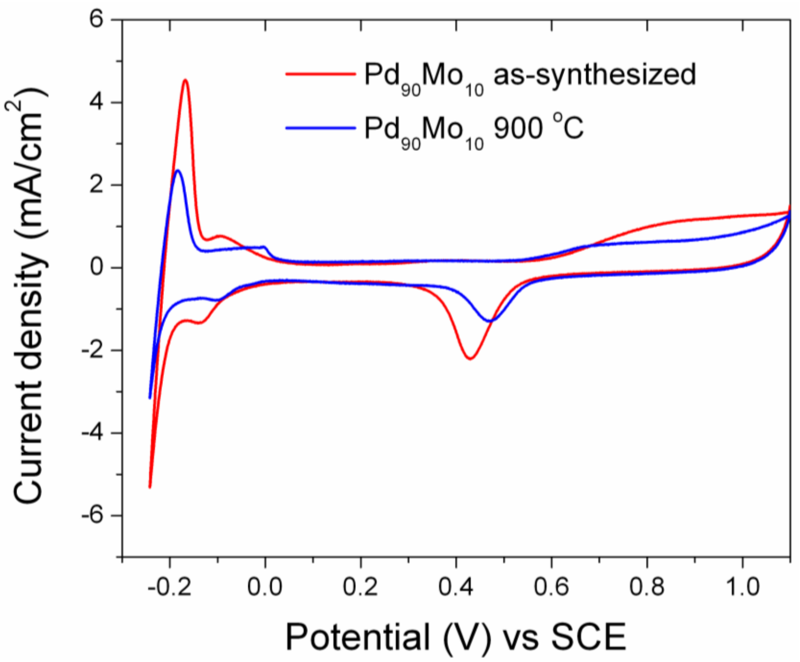

Figure 3.8. Cyclic voltammograms of the as-synthesized $Pd_{90}Mo_{10}$ and $Pd_{90}Mo_{10}$ after heat treatment at 900 °C, showing no change in the water activation potential.

Figures 3.9 (a)-(c) compare the CO stripping volatammetric profiles of as-synthesized Pd along with $Pd_{90}Mo_{10}$ and Pd after heat treatment at 900 °C. The base voltammograms for all the three samples in N_2 saturated 0.5 M H_2SO_4 obtained after complete oxidation of CO is also presented. As can be seen, the CO stripping peak for as-synthesized Pd is located at 1.1 V vs NHE. Moreover, the electrochemical surface area of as-synthesized Pd, evaluated from the charge due to CO stripping, was found to be 66.6 m^2/gm. However, after heat treating Pd at 900 °C, two distinct peaks were observed at 0.9 and 1.1 V vs NHE. Additionally, due to high heat treatment temperature, a marked decrease in electrochemical surface area as evaluated from CO stripping (22 m^2/gm) was observed. Similar to 900 °C heat treated Pd, $Pd_{90}Mo_{10}$ after heat treatment at 900 °C also showed two distinct stripping peaks located at 0.92 and 1.1 V vs NHE. The electrochemical surface area evaluated for $Pd_{90}Mo_{10}$ after heat treatment at 900 °C was found to be 17 m^2/g. This corroborates well with the TEM data that indicate slightly larger particle sizes for $Pd_{90}Mo_{10}$ compared to Pd after heat treatment at 900 °C.

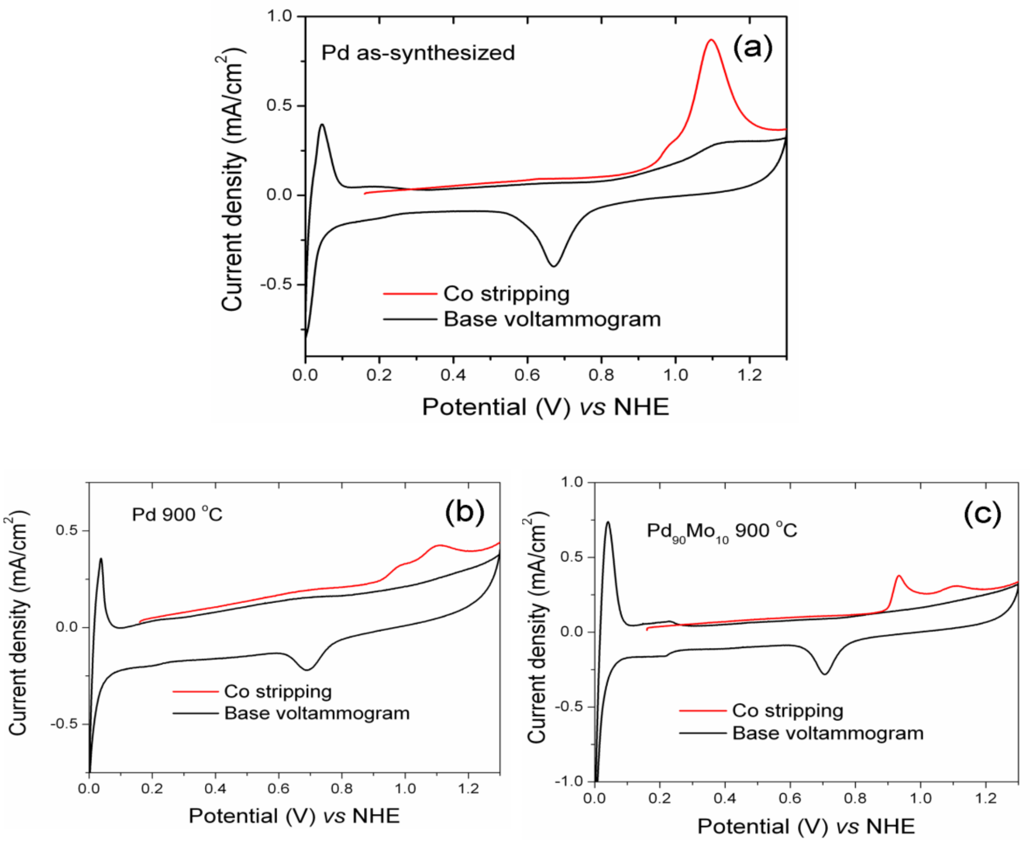

Figure 3.9. CO stripping voltammetry of (a) as-synthesized Pd, (b) Pd after heat treatment at 900 °C, and (c) $Pd_{90}Mo_{10}$ after heat treatment at 900 °C.

Figures 3.10(a) and (b) presents a comparison of the activities of selected Pd-Mo alloy electrocatalyst after heat treatment at 900 °C with those of heat treated Pd and as-synthesized Pt for oxygen reduction reaction in O_2 saturated 0.5M H_2SO_4. From the hydrodynamic polarization curves as shown in Fig. 3.10(a), it is evident that ORR on heat treated Pd catalyst is under mixed kinetic and diffusion control in the potential window between 1.0 and 0.3V. Also measurable currents were observed only below 0.70 V. Alloying of Mo significantly increases the activity as can be seen for $Pd_{90}Mo_{10}$ and $Pd_{80}Mo_{20}$. In the case of $Pd_{90}Mo_{10}$, the onset potential for ORR was found to be 0.80 V and the limiting current was same as that observed for as-synthesized Pt (3.4 mA/cm^2). Increasing the Mo content, however, has an adverse effect on activity as can be seen for $Pd_{80}Mo_{20}$. Figure 3.10(b) presents the mass transfer corrected kinetic currents for as-synthesized Pt, Pd, $Pd_{90}Mo_{10}$, and $Pd_{80}Mo_{20}$ heat treated at 900 °C at various potentials. The kinetic currents were obtained using equation 3.2 as shown below.

$$\frac{1}{i} = \frac{1}{i_l} + \frac{1}{i_k} \qquad [3.2]$$

where i_l is the limiting current (taken at + 300 mV), i_k is the kinetic current, and i is the total current. It can be observed that Pd and Pd-Mo alloys did not reach a clear limiting current. This can be attributed to strong adsorption of bisulphate ions [133].

From the plot, it can be concluded that the activity of $Pd_{90}Mo_{10}$ for ORR is significantly higher than those of Pd and $Pd_{80}Mo_{20}$.

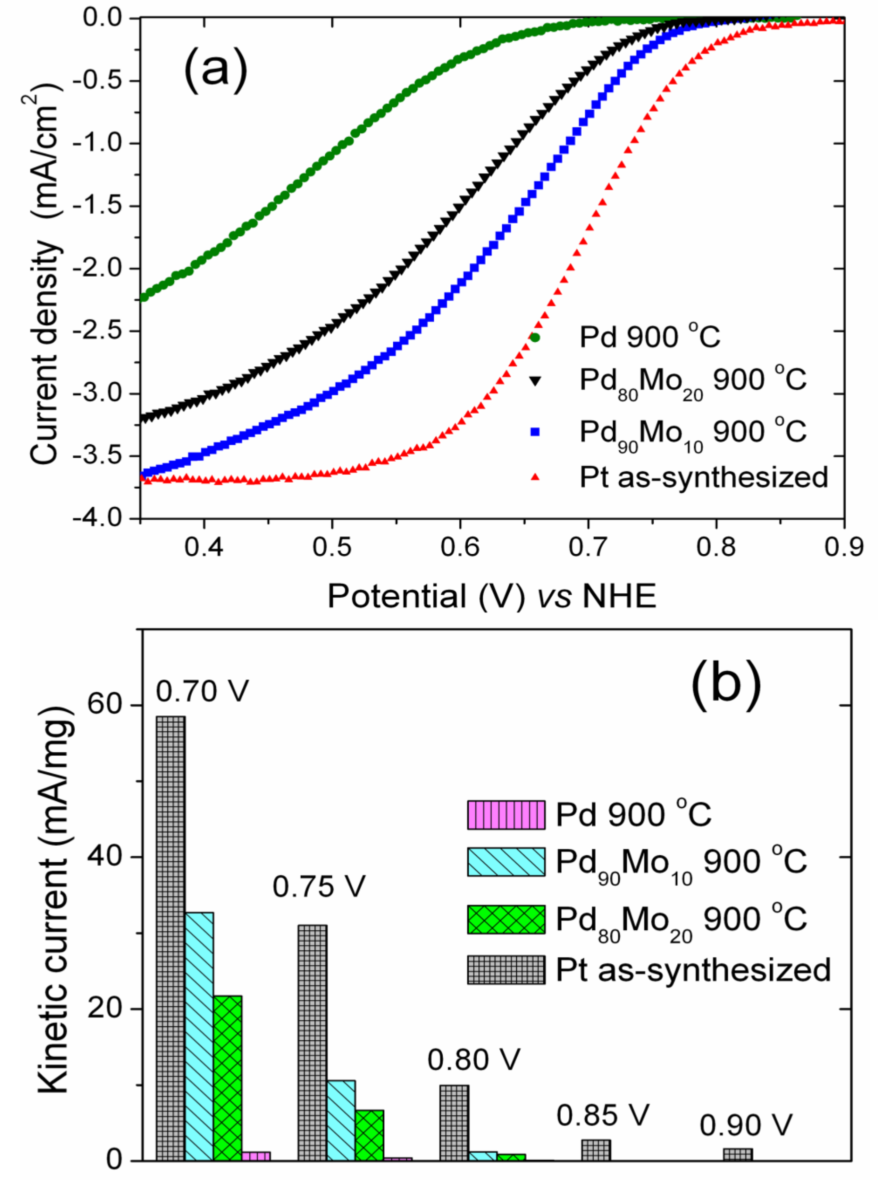

Figure 3.10. (a) Hydrodynamic polarization curves of Pd, $Pd_{90}Mo_{10}$, and $Pd_{80}Mo_{20}$ after heat treatment at 900 °C along with that for as-synthesized Pt. The ORR curves were obtained in O_2 saturated 0.5M H_2SO_4 with a rotation speed of 1600 rpm at room temperature (the current density refers to geometric area). (b) Mass transport corrected kinetic currents at various potentials (for Pd and $Pd_{80}Mo_{20}$ the limiting current values were taken at +300 mV).

3.3.2 Pd-W system

Figure 3.11 compares the XRD patterns of the carbon-supported $Pd_{100-x}W_x$ ($0 \leq x \leq 30$) catalysts after heat treating at various temperatures. It can be observed that there are no shifts in the positions of the $Pd_{100-x}W_x$ reflections compared to those of Pd even after heating at 800 °C possibly due to the similar atomic sizes of Pd and W. Thus, the formation of a solid solution alloy between Pd and W could not be established directly from the XRD data. However, Pd crystallizes as face centered cubic structure (*fcc*) and W crystallizes as body centered structure (*bcc*), and thus a phase separation at certain Pd to W atomic ratio is probable. Indeed, the literature Pd-W phase diagram clearly shows the formation of a face centered cubic solid solution up to 23 atom % W and a two-phase region consisting of a Pd-rich face centered cubic phase and a W-rich body centered cubic phase beyond 23 atom % W at 800 °C. Examination of the XRD data of the samples heat treated at 800 °C reveals that while W impurity reflections are present in the $Pd_{70}W_{30}$ sample, no such reflections are seen in $Pd_{80}W_{20}$. This suggests the formation of single phase solid solution up to about 20 atom % W, which is consistent with the published phase diagram data [134]. However, it is possible that a small amount of tungsten that is below the detection limit of XRD could be present as an impurity phase in $Pd_{80}Mo_{20}$ even after heat treatment at 800 °C. Also, no W impurity reflections are seen in $Pd_{70}W_{30}$ after heat treating at 700 °C, possibly due the presence of tungsten as poorly crystalline or amorphous oxide or unalloyed W.

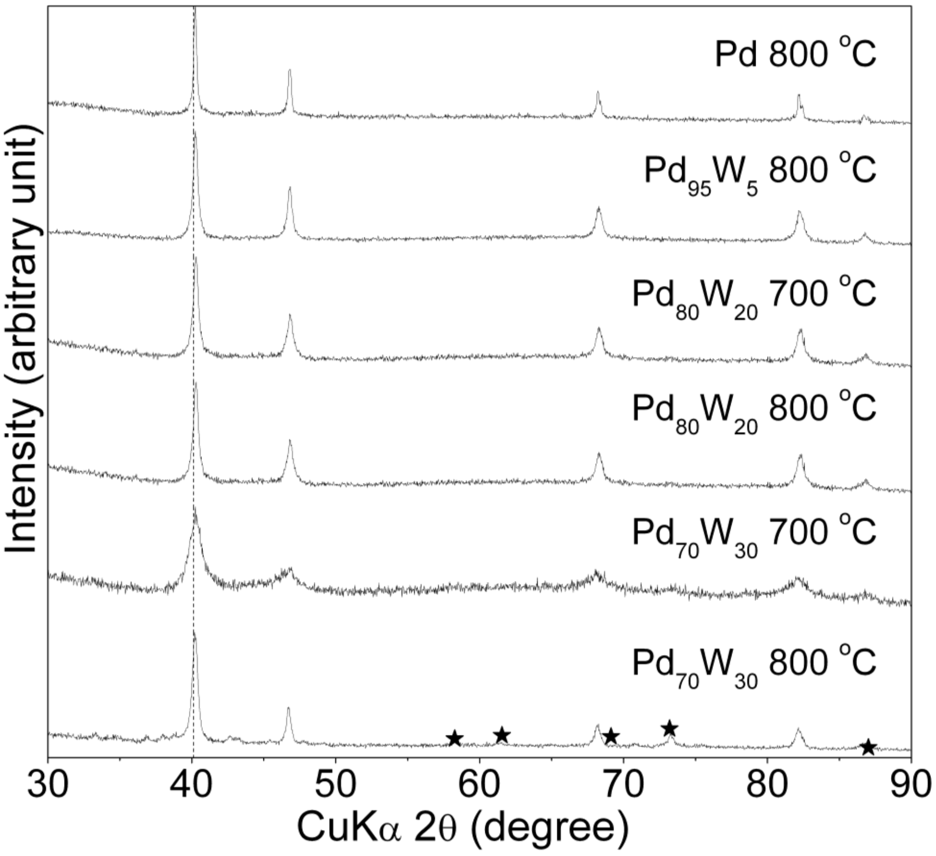

Figure 3.11. X-ray diffraction patterns of Pd, $Pd_{95}W_5$, $Pd_{80}W_{20}$, and $Pd_{70}W_{30}$ after heat treating at various temperatures. The dotted line refers to the expected position of the (111) reflection of Pd. The reflections marked with * in $Pd_{70}W_{30}$ after heat treating at 800 °C refer to the W impurity phase (PDF # 00-004-0806).

The TEM images and the particle size distributions of the as-synthesized and 800 °C heat treated $Pd_{95}W_5$ samples are compared in Fig. 3.12. The as-synthesized $Pd_{95}W_5$ sample has a mean particle diameter of 4.5 nm with a narrow size distribution, which is similar to that of the as-synthesized Pd sample. However, the particle sizes of both Pd and $Pd_{95}W_5$ increase significantly, respectively, to 10.1 and 11.6 nm with a slightly broader size distribution after heat treatment at 800 °C.

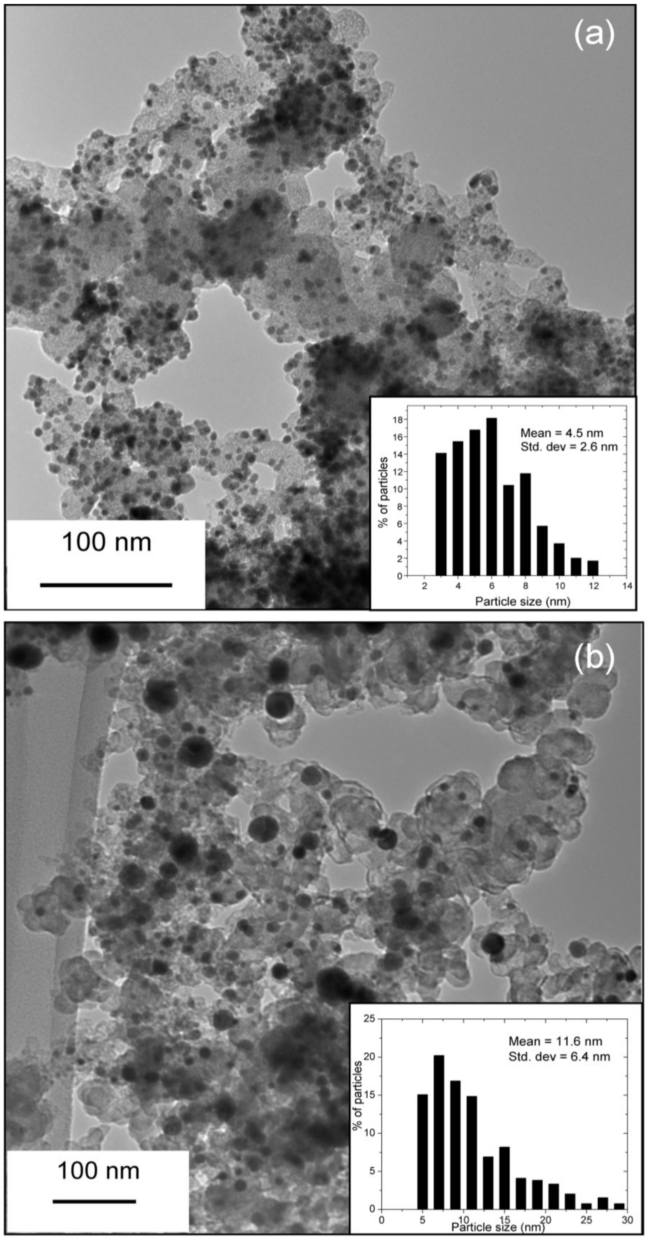

Figure 3.12. TEM images and particle size distributions of (a) as-synthesized $Pd_{95}W_5$ and (b) $Pd_{95}W_5$ after heat treating at 800 ^oC in flowing H_2 for 2 h.

Figures 3.13 (a)-(c) shows the Pd 3*d* and W 4*f* core level XPS profiles of Pd and $Pd_{95}W_5$ after heat treatment at 800 °C. All the XPS profiles were fitted by Gaussian – Lorentzian (30 % Gaussian) method after background subtraction using Shirley's method. Also, the peaks corresponding to Pd $3d_{5/2}$ and Pd $3d_{3/2}$ core levels were deconvoluted into Pd and PdO_y ($1 \leq y \leq 2$). As evident from Fig. 3.13 (a), palladium in the surface exists as both Pd metal and PdO_y in all the samples. Additionally, a small shift in the binding energy of the Pd $3d_{5/2}$ core level in $Pd_{95}W_5$ by + 0.2 eV compared to that in Pd (335. 3 eV) was observed [135,136]. This suggests a change in the electron density around Pd upon alloying with W. Figure 3.13 (c) shows the W 4*f* peaks. Two distinct $4f_{7/2}$ doublets centered at 35.3 and 32.3 eV corresponding to WO_z ($1 \leq z \leq 3$) and WC can be seen [137,138]. Based on the XPS data, it can be concluded that a small amount of surface carburization resulting in WC (less than 20 atom %) might have occurred during the heat treatment of the carbon-supported catalysts at 800 °C and the formation of WO_z and PdO_y moieties on the surface might have occurred due to the exposure of the samples to ambient. The Pd : W ratio in $Pd_{95}W_5$ as determined from the XPS peak areas was 93.7 : 6.3, which is close to the nominal composition. The XPS analysis in conjugation with the SEM-EDS data suggests that there is no surface segregation similar to that found with the Pd-Mo system. However, enrichment in the surface layers cannot be ruled out as the XPS technique has certain penetration depth.

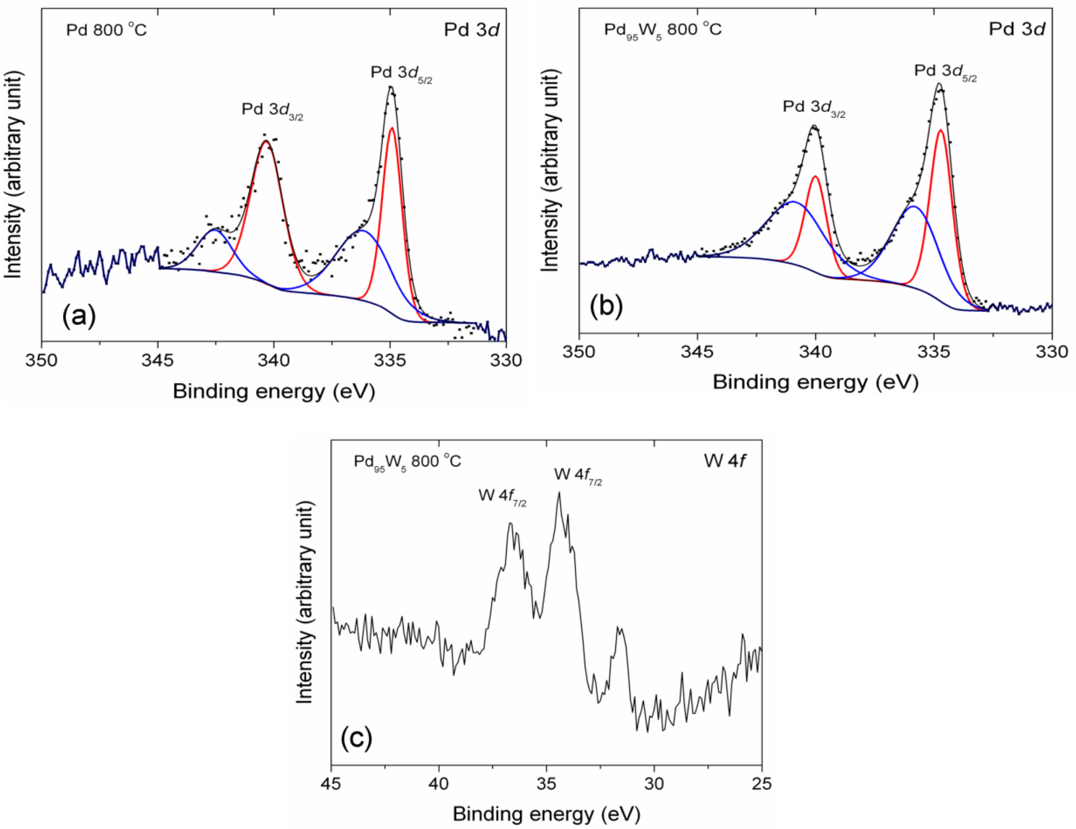

Figure 3.13. XPS profiles and fitting results of 800 °C heat treated Pd and $Pd_{95}W_5$: (a) Pd 3*d* core levels showing Pd [red lines] and PdO_y ($1 \leq y \leq 2$) [blue lines] and (b) W 4*f* core levels. Points refer to the experimental curves and solid lines refer to the fitted curves.

Figure 3.14 compares the cyclic voltammograms at 1st and 5th cycles of the as-synthesized carbon-supported Pd, $Pd_{90}W_{10}$, and $Pd_{80}W_{20}$ catalysts. For brevity, the CVs of $Pd_{95}W_5$ and $Pd_{85}W_{15}$ are not shown, but they closely follow the trend in Fig. 3.14. As seen in Fig. 3.14(a), the peak current density values for the surface oxide reduction (cathodic) peak increases with increasing tungsten content in the as-synthesized Pd-W samples and the peak shifts towards lower potentials compared to that in Pd. In the anodic surface oxide formation region, the tungsten incorporated samples show lower currents compared to Pd, suggesting reduced formation of $Pd(OH)_2$ (E^o = 0.897 V *vs* SHE) and PdO (E^o = 0.917 V *vs* SHE). Incorporation of tungsten also causes changes in the hydrogen adsorption and desoption regions of the CV. However, the tungsten incorporated samples show lower peak area compared to the as-synthesized palladium. Similar to the Pd-Mo system, Pd-W electrocatalysts also show an increase in water activation potential although the shift is not as large as in the case of Pd-Mo system. Thus, the delayed onset potential for water activation for both Pd-Mo and Pd-W systems suggest that incorporation of both Mo and W increases the nobility of Pd and prevent surface oxidation of Pd.

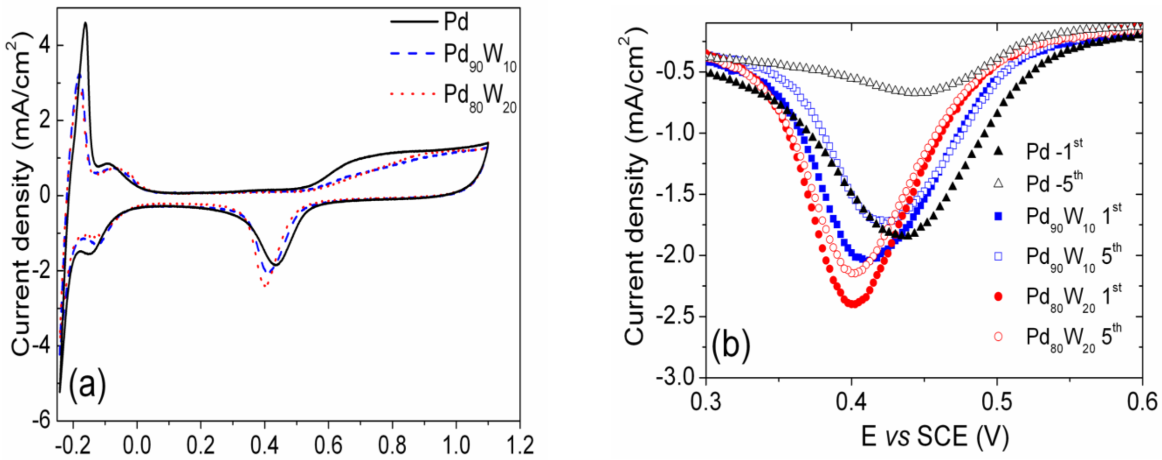

Figure 3.14. Comparison of the (a) cyclic voltammograms and (b) surface oxide reduction (cathodic) region of the voltammograms after 1st and 5th cycles of as-synthesized Pd, $Pd_{90}W_{10}$, and $Pd_{80}W_{20}$ electrocatalysts.

However, after 5 cycles, the peak current density (or active surface area) of both the Pd and the W incorporated samples drop substantially although the drop is less severe for the W incorporated samples as seen in Fig. 3.14(b). The decrease has been attributed to the formation and incipient growth of PdO and $Pd(OH)_2$ films and subsequent dissolution of Pd as Pd^{2+} in acidic solutions in the potential range of 0.5 - 1.3 V *vs* SHE, which also explains the anomalous observations in the anodic oxide formation and cathodic surface oxide reduction mentioned earlier. On heat treating at 300, 500, and 700 ^{o}C, no significant change was noticed in the stability although the peak current decreased and the cathodic peak potential shifted positive compared to the as-synthesized Pd due to an increase in particle size and corresponding decrease in surface area.

Figure 3.15(a) compares the voltammograms of the carbon-supported Pd, $Pd_{95}W_5$, $Pd_{90}W_{10}$, $Pd_{85}W_{15}$, and $Pd_{80}W_{20}$ catalysts after heat treatment at 800 ^{o}C. From the data, it is evident that the Pd-W solid solution alloys show much higher oxide reduction peak currents and hydrogen desorption areas than Pd. This suggests that alloying of Pd with W enhances the activity for surface oxide formation and its reduction. Among the Pd-W samples tested, $Pd_{95}W_5$ shows the maximum oxygen reduction peak current. Interestingly, alloying of Pd with W also suppresses the dissolution of Pd. As seen in Fig. 3.15(b), no significant reduction in peak areas is noticed for both the surface oxide reduction and hydrogen desorption peaks of $Pd_{95}W_5$ after 15 cycles. However, increasing the W content beyond $Pd_{85}W_{15}$ had an adverse effect on stability. Alloying of tungsten also modifies the hydrogen desorption region of the CV substantially. As seen in Fig. 3.15(a), the hydrogen desorption peak area is maximum for $Pd_{95}W_5$, and the area decreases substantially on increasing the W content further.

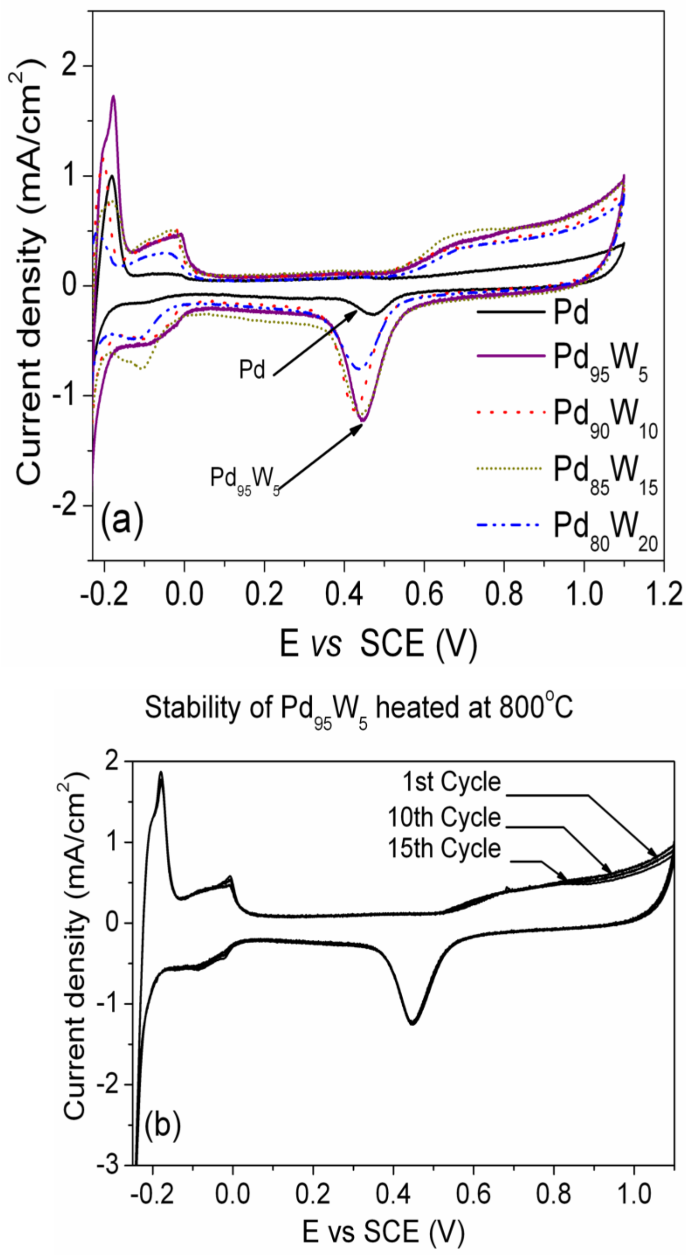

Figure 3.15. Comparison of (a) the cyclic voltammograms of the 800 °C heat treated Pd, $Pd_{95}W_5$, $Pd_{90}W_{10}$, $Pd_{85}W_{15}$, and $Pd_{80}W_{20}$ samples and (b) the cyclic voltammograms of $Pd_{95}W_5$ after 1st, 10th, and 15th cycles.

Figure 3.16 shows the CO stripping volatammetric profiles of $Pd_{95}W_5$ after heat treatment at 800 °C along with the base voltammogram in 0.5 M H_2SO_4. Similar to $Pd_{90}Mo_{10}$ and Pd after heat treatment at 900 °C, two distinct peaks were observed at 0.93 and 1.1 V vs NHE. However, unlike in Pd and $Pd_{90}Mo_{10}$, a small peak was observed at 0.83 V *vs* NHE for $Pd_{95}W_5$. As explained earlier, the XPS analysis revealed small amount of tungsten carbide (an isoelectronic species with Pt). The small peak might be a result of additional adsorption of CO on those tungsten carbide surface sites and subsequent oxidation of CO by adsorbed water [139]. Additionally, the electrochemical surface area evaluated for $Pd_{95}W_5$ after heat treatment at 800 °C was found to be 29 m^2/gm.

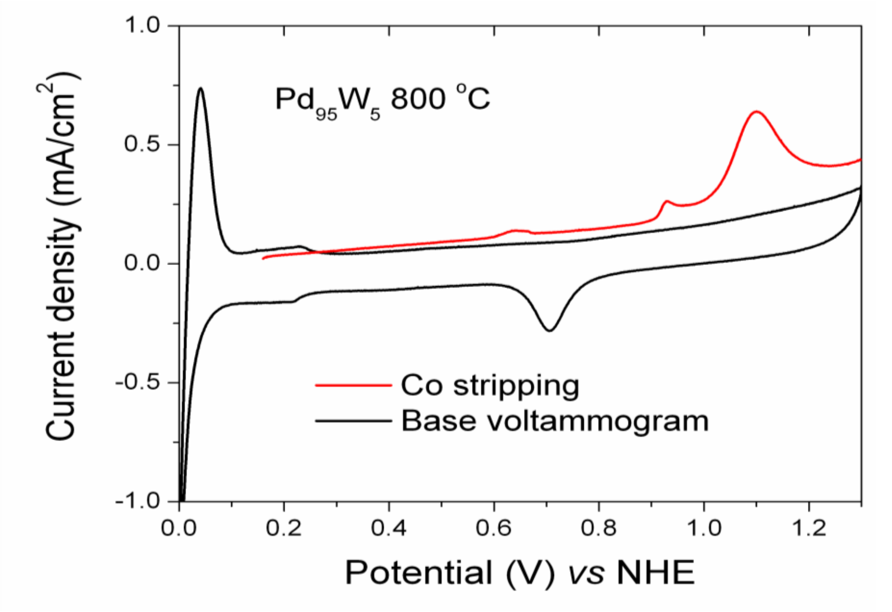

Figure 3.16. CO stripping voltammetry of $Pd_{95}W_5$ after heat treatment at 800 °C along with the base voltammogram.

Figures 3.17(a) and (b) present a comparison of the activities of selected Pd-W alloys and Pd after heat treatment at 800 ^{o}C with that of as-synthesized Pt for ORR based on rotating disk electrode (RDE) measurements in 0.5 M H_2SO_4. Alloying of Pd with W increases significantly the activity as can be seen with $Pd_{95}W_5$, $Pd_{90}W_{10}$, and $Pd_{85}W_5$ compared to Pd. In the case of $Pd_{95}W_5$, the onset potential for ORR was found to be 0.85 V and the limiting current was 4.2 mA/cm^2. Figure 3.17(b) presents the mass transfer corrected kinetic currents for the as-synthesized Pt and 800 ^{o}C heat treated Pd, $Pd_{95}W_5$, and $Pd_{90}W_{10}$ at various potentials obtained from equation 3.2. In the absence of a reliable active surface area value for Pd because of the absorption of hydrogen, the current densities were evaluated based on the geometric area. From the plots, it can be concluded that the activities of $Pd_{95}W_{5,}$ $Pd_{90}W_{10}$, and $Pd_{85}W_5$ for ORR are significantly higher than that of Pd and the ORR activity of $Pd_{95}W_5$ is comparable to the as-synthesized Pt although the particle size of $Pd_{95}W_5$ (11.6 nm ± 6.4 nm) is almost two times that of the as-synthesized Pt (5.6 nm ± 1.4 nm). As the initial and onset part of the curve will depend on real surface area, a decrease in real surface area will shift the curve to lower potentials irrespective of the catalytic activity. The higher catalytic activity of $Pd_{95}W_5$ compared to that of Pd despite a slightly smaller surface area for the former resulting from a slightly larger particle size indicate that alloying with W intrinsically enhances the activity of Pd.

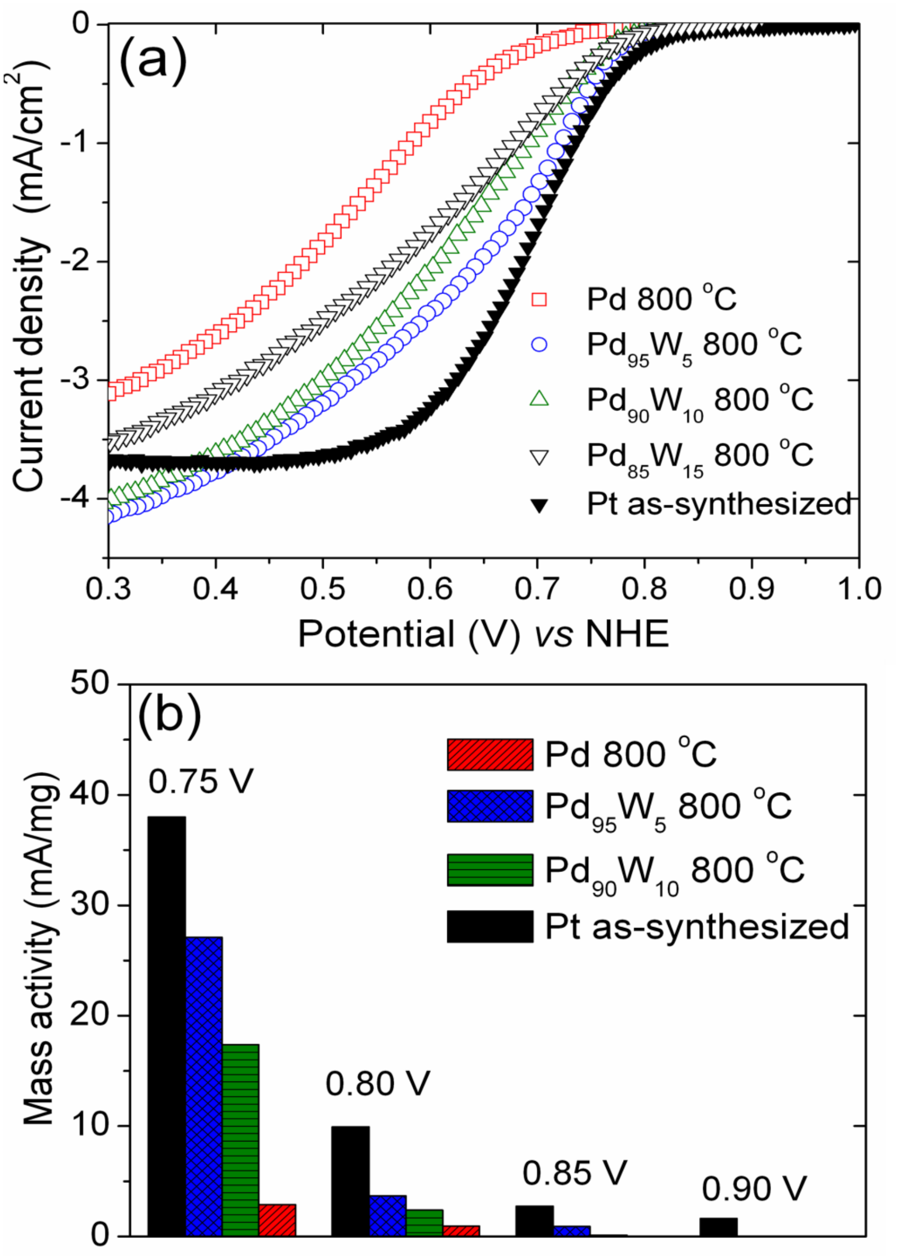

Figure 3.17. (a) Comparison of the hydrodynamic polarization curves of Pd, $Pd_{95}W_5$, and $Pd_{90}W_{10}$ after heat treatment at 800 °C with that of as-synthesized Pt. The ORR curves were obtained in O_2 saturated 0.5 M H_2SO_4 with a rotation speed of 1600 rpm at room temperature (the current density refers to geometric area). (b) Mass transport corrected kinetic currents at various potentials (the limiting current values were taken at +300 mV).

3.3.3 ORR activity comparison of Pd-Mo and Pd-W systems

With an alloying temperature of 900 °C, the composition $Pd_{90}Mo_{10}$ with 10 atom % Mo was found to exhibit the maximum activity for ORR in the case of Pd-Mo binary alloy system, while the composition $Pd_{95}W_5$ after heat treatment at 800 °C was found to be the best in the Pd-W alloy system. Figure 3.18 compares the RDE plots of selected Pd-Mo and Pd-W samples for ORR. From the hydrodynamic polarization curves, it is evident that the ORR activity of $Pd_{95}W_5$ is slightly higher than that of $Pd_{90}Mo_{10}$.

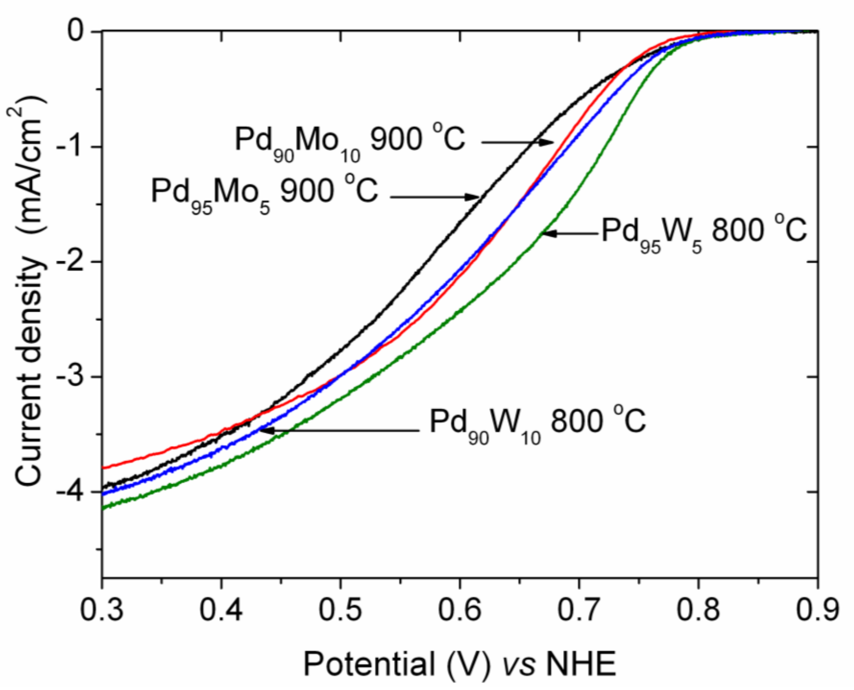

Figure 3.18. Comparison of the hydrodynamic polarization curves of 900 °C heat treated $Pd_{95}Mo_5$ and $Pd_{90}Mo_{10}$ with those of 800 °C heat treated $Pd_{95}W_5$ and $Pd_{90}W_{10}$. The ORR curves were obtained in O_2 saturated 0.5 M H_2SO_4 with a rotation speed of 1600 rpm at room temperature (the current density refers to geometric area).

3.3.4 Single cell proton exchange membrane fuel cell (PEMFC) tests

Figure 3.19 compares the polarization curves recorded in single cell PEMFC at 40 °C of as-synthesized Pt, $Pd_{90}Mo_{10}$ after heat treatment at 900 °C, and $Pd_{95}W_5$ after heat treatment at 800 °C. Since the $Pd_{90}Mo_{10}$ and $Pd_{95}W_5$ samples were after heat treatment at, respectively, 900 and 800 °C, they both have significantly larger particle sizes (11.6 ± 5.8 and 11.6 ± 6.4 nm, respectively, for $Pd_{90}Mo_{10}$ and $Pd_{95}W_5$) than Pt (5.6 ± 1.4 nm). Despite the larger particle size, the $Pd_{90}Mo_{10}$ and $Pd_{95}W_5$ samples exhibit activities for ORR close to that of as-synthesized Pt, confirming the cyclic voltammetry and RDE data that alloying of Pd with both Mo and W increases the electrocatalytic activity for ORR. Between $Pd_{90}Mo_{10}$ and $Pd_{95}W_5$, the latter exhibits slightly higher activity.

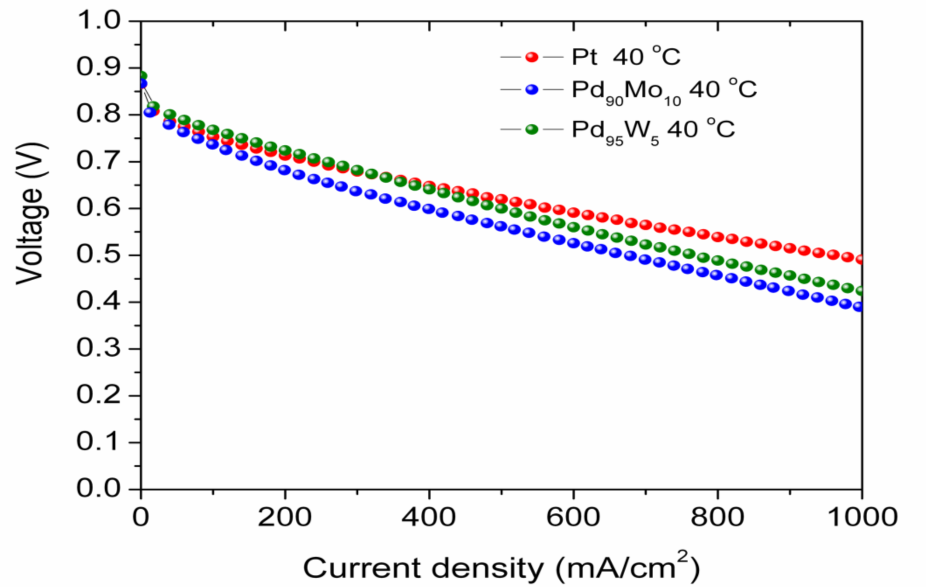

Figure 3.19. Comparison of the oxygen reduction reaction (ORR) activities of as-synthesized Pt, $Pd_{90}Mo_{10}$ after heat treatment at 900 °C, and $Pd_{95}W_5$ after heat treatment at 800 °C in single cell proton exchange membrane fuel cell (PEMFC) at 40 °C.

3.3.5 Methanol tolerance tests

It has been demonstrated before that the palladium-based alloy catalysts are not active for methanol oxidation and they show high tolerance to methanol that may crossover from the anode to the cathode through the Nafion membrane in a DMFC [140-142]. Indeed, the CV plot of $Pd_{95}W_5$ after heat treatment at 800 °C and $Pd_{90}Mo_{10}$ after heat treatment at 900 °C in a mixture of 0.5 M methanol and 0.5 M H_2SO_4 as shown in Fig. 3.20 does not show any current due to methanol oxidation compared to a significant activity of the as-synthesized platinum catalyst for methanol oxidation. The results suggest that both $Pd_{95}W_5$ as well as $Pd_{90}Mo_{10}$ can be a potential ORR electrocatalyst in DMFC.

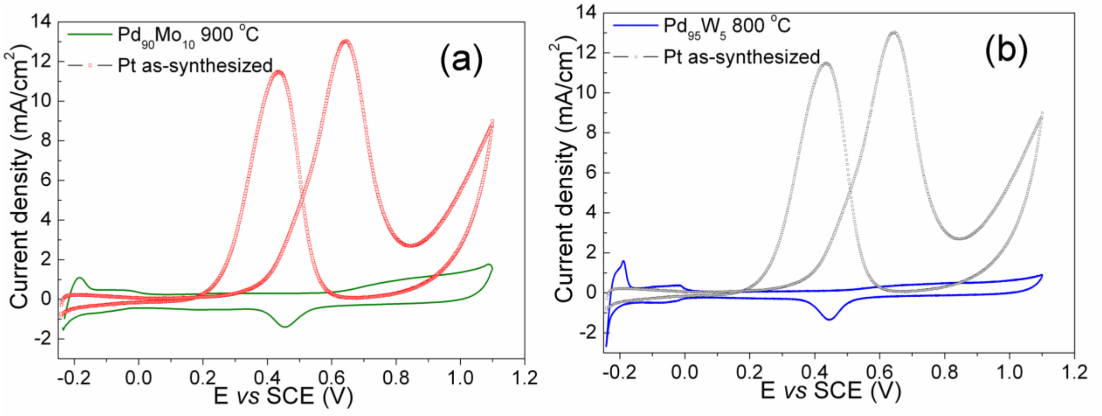

Figure 3.20. Cyclic voltammograms of (a) as-synthesized Pt and $Pd_{90}Mo_{10}$ after heat treatment at 900 °C and (b) as-synthesized Pt and $Pd_{95}W_5$ after heat treatment at 800 °C.

3.4 UNDERSTANDING THE ENHANCEMENT IN CATALYTIC ACTIVITY

Oxygen reduction is a multi-electron reduction process and involves a number of reaction steps, intermediates, and adsorbed species. The rate determining step and the kinetics are not only different for different electrocatalysts, but also dependent on the crystal faces of the same electrocatalyst [143]. It has been demonstrated that palladium-based alloy catalysts promote a four-electron pathway for the oxygen reduction reaction in acidic solution [144,145]. Therefore, it is reasonable to assume that the mechanisms proposed for the enhancement in activity on alloying Pt with other elements like Co can be applied for Pd-based alloy catalysts as well. The enhanced electrocatalytic activity of platinum alloys like Pt-Co, Pt-Ni, and Pt-Fe has been explained on the basis of the (i) modification of the electronic structure of Pt (5d-orbital vacancies), (ii) changes in the Pt-Pt bond distance and coordination number, and (iii) inhibition of adsorbed oxygen-containing species from the electrolyte onto Pt (section 1.5.1). More recently, it has been proposed that for Pt-M (M = Fe, Co, Ni, and Cu) alloy catalysts, selective dissolution of the alloying element from the top layers resulting in a Pt skin structure causes a change in the d-states of the surface atoms. As the filling of the antibonding states of O_2 2p determines the strength of interaction of the metal-oxygen bond, which is dependent on the position of the metal d states relative to the Fermi level, the dissociative chemisorption of oxygen changes with the alloying element [42-45]. A higher d band centre will result in stronger metal-oxygen bond. Theoretical calculations have shown that the location of metal d band of the surface for Pt, Pd, and Ni are, respectively, -1.98, -1.54 and, -1.21 eV [146]. Thus, oxygen binds more strongly on Pd compared to Pt. The kinetics of the net oxygen reduction reaction, however, depends on two competing processes: dissociative adsorption of O_2 and subsequent transfer of electrons and protons to the adsorbed O_2 and the removal of adsorbed OH and O species from the surface. A decrease in electron density in Pd on alloying with Mo and W as suggested by the XPS data may weaken the Pd-O bond and thus enhance the dissociative adsorption of O_2. Moreover, with increasing content of Mo and W, the removal of adsorbed OH and O species may become difficult, resulting in a decrease in the performance and stability at higher molybdenum or tungsten contents. However, it should be noted that unlike platinum where the dissolution rate is slow, dissolution of Pd itself can limit the application of the proposed mechanisms. Nevertheless, alloying of Pd with tungsten as well as molybdenum suppresses the dissolution of Pd.

Another factor that has been proposed for the enhancement in the catalytic activity for ORR on alloying Pt with other elements is the Pt-Pt nearest neighbor distance that promotes alternate reaction pathways [38]. However, this effect is anticipated to be negligible in the Pd-W or Pd-Mo system as the XRD data show no significant change in the lattice parameter values on alloying Pd with W or Mo.

3.5 CONCLUSION

A facile synthesis approach has been adopted to prepare carbon supported $Pd_{100-x}Mo_x$ ($0 \leq x \leq 40$) and $Pd_{100-y}W_y$ ($0 \leq y \leq 30$) electrocatalysts for the oxygen reduction reaction in fuel cells. XPS analysis shows a change in the chemical environment of Pd upon alloying with both Mo and W, which might have an important bearing on the increased activity for ORR. Alloying of Pd with Mo and W is found to increase both the catalytic activity for ORR and the catalyst durability. Although high heat treatment temperatures to realize the alloy formation increases the particle size of the Pd-Mo and Pd-W alloys significantly compared to that of as-prepared Pt catalyst, the mass activity of $Pd_{95}W_5$ is comparable to that of Pt. In addition, both the Pd-Mo and Pd-W alloy electrocatalysts offer an important advantage of high tolerance to methanol compared to Pt. The lower cost and higher tolerance to methanol of the Pd-based alloy catalysts compared to Pt may make them attractive for direct methanol fuel cells.

Chapter 4: Microwave synthesis of low-platinum, palladium-based ternary electrocatalysts

4.1 INTRODUCTION

As discussed in section 1.6.1, alloying of Pt with other transition metals have been actively pursued to increase the activity for ORR as well as to lower the cost. In this regard, various platinum-based alloy electrocatalysts for oxygen reduction reaction (ORR) have been widely investigated. Nanostructured platinum-based Pt-M (M = 3d transition metals like Fe, Co, Ni, and Cu) alloy electrocatalysts are of particular interest for fuel cells as they can have multi-fold increase in electrocatalytic activity compared to pristine platinum for ORR. Among the Pt-M alloys, Pt-Co has received maximum attention as many fold increase in the activity for ORR has been demonstrated [24-41]. Recent research efforts have focused on understanding the possible reason for the increase in specific ORR activity of Pt-M alloys by forming a "Pt-skeleton" after leaching out the transition metal M or by forming a "Pt-skin" (a Pt single atomic surface layer) after annealing [44,59]. However, Pt-Pd bimetallic alloys have not been explored extensively [147,148]. Although, it has been theoretically hypothesized and experimentally verified that Pt monolayer on Pd offers electrocatalytic activity several times higher than that of Pt [66-70].

Tremendous efforts have been made to synthesize multimetallic nanosize Pt- and Pd-based alloys by various synthesis approaches such as co-precipitation, impregnation, microemulsion, and microwave-assisted polyol methods [149-156]. However, these methods often require either long reaction times (2 – 24 h) or post heat treatment processing at temperatures as high as 900 ^{o}C in reducing gas atmosphere to achieve solid solution alloy formation, which could lead to increase in particle size and decrease in catalytic activity. Although, microwave-solvothermal (MW-ST) method has been used to synthesize various metal and metal oxide nanoparticles, the ORR activity of nanoalloy electrocatalysts prepared by the MW-ST method is yet to be studied [157-160].

This Chapter presents a rapid microwave-assisted solvothermal (MW-ST) approach to synthesize multimetallic nanoalloy ($Pt_{75}Co_{25}$, $Pt_{70}Pd_{20}Co_{10}$, and $Pt_{50}Pd_{30}Co_{20}$) electrocatalysts within a short reaction time at temperatures as low as 300 ^{o}C without requiring any post heat treatment in reducing gas atmospheres. This "metallurgy in a quartz vessel" approach offers a uniform heating of polar solvents by absorbing microwave energy and subsequent transfer of the heat selectively to the reactants, which reduces thermal gradients inside the reaction vessel and increases the reaction kinetics. The MW-ST method provides a uniform nucleation environment and offers highly crystalline monodispersed multimetallic nanoalloys with a high degree of alloying. For a comparison, the same bimetallic and tri-metallic alloys are also synthesized by a conventional reduction method with sodium borohydride, followed by heat treatment at 300 – 900 ^{o}C. Additionally, a series of Pt encapsulated Pd-Co electrocatalysts have also been synthesized by a two step microwave method and investigated for their activity for ORR.

The as-synthesized samples are characterized by XRD, TEM, EDS in SEM, XPS, CV, and electrochemical polarization measurements in RDE for ORR. Selected catalysts are also evaluated in a single cell PEMFC and compared with commercial Pt.

4.2 EXPERIMENTAL

4.2.1 Synthesis of Pt-Pd-Co alloy electrocatalysts

200 mg of carbon-supported $Pt_{75}Co_{25}$, $Pt_{70}Pd_{20}Co_{10}$, $Pt_{50}Pd_{30}Co_{20}$ catalysts with 20 wt. % metal loading were synthesized as described below. Required amounts of

$H_2PtCl_6.6H_2O$ (Strem Chemicals Inc.), $(NH_4)_2PdCl_4$ (Alfa Aesar), and $CoCl_2.6H_2O$ (Alfa Aesar) were first dissolved in 50 mL of tetraethylene glycol (TEG; b.p.= 328 ^oC, viscosity = 58.3 cP [161]) (Alfa Aesar) under constant stirring. After dissolving the metal salts completely, 160 mg of Vulcan XC-72R carbon black (Cabot Corp.) and 1.5 mL of 1 M NaOH (drop wise) were added under constant stirring. The mixture was then transferred to a quartz vessel and placed on a turntable for uniform heating in an Anton Paar microwave synthesis system (Anton Parr Synthos-3000) equipped with a wireless pressure and temperature sensor. With an operating frequency of 2.45 GHz and a power of 600 W, the sample temperature was ramped to and kept at 300 °C for 15 minutes while the pressure was raised to 80 bar. Precipitation of multimetallic nanoparticles and alloy formation took place inside the reactor during this solvothermal process. The resulting precipitate was repeatedly washed with acetone and de-ionized water to remove traces of TEG and other impurities and the powder was dried in an air-oven at 100 ^oC. The carbon-supported catalysts thus obtained were used for further characterization and electrochemical studies without any post heat treatment. The synthesis scheme is shown in Fig. 4.1.

For the conventional borohydride reduction method, 160 mg of Vulcan XC-72R carbon black was sonicated with 50 mL of water and 5 mL of isopropyl alcohol for 5 minutes to form a homogeneous dispersion. Required amounts of metal salts were then added to this mixture under constant stirring so that the total metal loading was 20 wt. %. A solution containing 150 mg of $NaBH_4$ (Fisher Scientific) in 25 mL of water was then added drop wise and the reduction reaction was conducted for 30 minutes under constant stirring. The suspension was then filtered and washed repeatedly with de-ionized water. The as-prepared samples thus obtained were then heat treated at 300, 500, 700, and 900

°C in a flowing 10 % H_2 – 90 % Ar mixture for 2 h in a tube furnace with a heating and cooling rates of 5 °C min^{-1}.

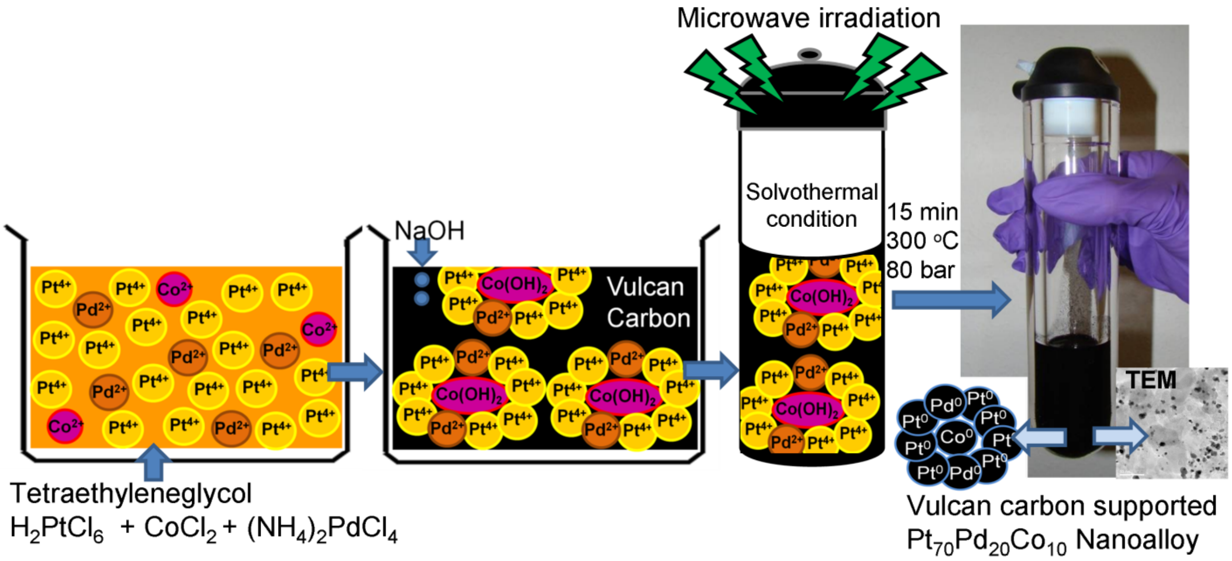

Figure 4.1. Schematic illustration of microwave-assisted, one-pot solvothermal synthesis of Pt-Pd-Co nanoalloy electrocatalysts.

4.2.2 Synthesis of Pt encapsulated Pd-Co alloy electrocatalysts

100 mg of carbon-supported Pt-encapsulated Pd-Co electrocatalysts with a 20 wt. % metal loading on carbon were synthesized by a two-step MW-ST process as described below. Required amounts of $(NH_4)_2PdCl_4$ (Alfa Aesar) and $CoCl_2.6H_2O$ (Alfa Aesar) were dissolved in 25 mL of tetraethylene glycol (TEG) (Alfa Aesar) under constant stirring to give Pd_xCo_{100-x} with $0 \leq x \leq 100$. After a complete dissolution of the salts, 1.5 mL of 1 M NaOH was added along with required amount of Vulcan XC-72R carbon

black (Cabot Corp.) was added under stirring. The mixture was then transferred to a quartz vessel, sealed, and placed on a turntable for uniform heating in an Anton Paar microwave synthesis. With an operating frequency of 2.45 GHz and a power of 600 W, the sample temperature was ramped to and kept at 300 °C for 15 minutes while the pressure was raised to 40 bar. The resulting precipitate was repeatedly washed with acetone and de-ionized water to remove traces of TEG and other impurities, and the powder was dried in an air-oven.

The carbon-supported Pd_xCo_{100-x} thus obtained was then added into 25 mL of a TEG solution containing required amount of $H_2PtCl_6.6H_2O$ (Strem Chemicals Inc.), followed by the addition of 1.5 mL of 1 M NaOH, to realize (100-y) wt. % Pd_xCo_{100-x} + y wt. % Pt (y = 25, 50, and 75) on Vulcan carbon; the total Pd_xCo_{100-x} + Pt metal loading was 20 wt. % on 80 wt. % carbon and the y = 25, 50, and 75 samples represent, respectively, 5, 10, and 15 wt. % Pt loading on carbon. The mixture was again subjected to the MW-ST process in the Anton Paar microwave synthesis system as described above, followed by washing the precipitate with acetone and de-ionized water and drying in an air-oven to obtain the Pt-encapsulated Pd-Co electrocatalysts supported on carbon. For a comparison, 100 mg each of 20 wt. % Pt and 20 wt. % $Pd_{80}Co_{20}$ on 80 wt. % carbon were also synthesized in a single step by the MW-ST process. Finally, all the carbon-supported (100-y) wt. % Pd_xCo_{100-x} + y wt. % Pt samples were heat treated at 900 ^oC in 10% H_2 + 90% Ar gas mixture for 2 h with a heating and the cooling rate of 5 ^oC/min.

4.2.3 Material and electrochemical characterizations

The samples were all characterized by XRD and the metal ratios in the synthesized samples were assessed by EDS. Morphological and particle distribution studies were carried out with TEM. Surface composition was determined using XPS. All the XPS profiles were fitted by Gaussian method after background subtraction using Shirley's method.

Cyclic voltammetry (CV) characterizations were carried out with a standard single compartment three electrode cell having a Pt mesh counter electrode, a glassy carbon (5mm in dia., Pine Instruments, U.S.A) working electrode, and a double junction Ag/AgCl reference electrode, employing an Autolab PGSTAT302N potentiostat (Eco Chemie B.V., Netherlands). All potentials are, however, reported against normal hydrogen electrode (NHE). In a typical experiment, 10 mg of the carbon supported catalyst was ultrasonicated with 5 mL of de-ionized water and 5 mL of 0.15 wt% Nafion solution (prepared from 5 wt% Nafion solution obtained from Electrochem Inc. by adding appropriate amount of ethanol) until a dark homogeneous dispersion was formed. 20 µL of the aliquot was drop casted onto the glassy carbon electrode to give an effective carbon supported catalyst loading of 20.37 µg metal cm^{-2}. Rotating disk electrode (RDE) experiments were conducted with a glassy carbon disk electrode (5 mm dia.) mounted onto an interchangeable RDE holder (Pine Instruments, USA) in O_2 saturated 0.5 M H_2SO_4 (solutions prepared from Fisher Scientific high purity Optima grade 18 M H_2SO_4). Before each experiment, the glassy carbon electrode was polished to a mirror-like finish with 0.05 µm alumina (Buehler). The catalyst coated working electrode was prepared in the same way as mentioned above. Before recording the hydrodynamic polarization curves, the catalyst surface was cleaned off adventitious organic impurities and thermally adsorbed oxygen by cycling 50 times between 0.0 and 1.2 V (vs NHE) at a scan rate of 50 mV s^{-1}. The potential was then scanned from 1.0 to 0.0 V (vs NHE) at 5 mV s^{-1}.

For fuel cell tests, the catalyst ink and membrane electrode assembly (MEA) were prepared exactly as mentioned in section 3.2.1. The catalyst loading was kept at 0.4 mg/cm^2 both for the anode (Alfa Aesar HiSpec 3000) and the cathode in PEMFC. The fuel cell testing was carried out at an operating temperature of 60 ^oC with hydrogen and oxygen pressures of, respectively, 10 psig (0.689 bar) and 12 psig (0.827 bar) and the humidifier temperature was same as the cell temperature. The gas flow rates were 0.2 L/min for H_2 and 0.4 L/min for O_2. The flow of H_2 and O_2 was varied with load as, respectively, 0.022 L/minA and 0.055 L/minA. For DMFC measurements commercial $Pt_{50}Ru_{50}$ (BASF 60 wt% metal) was used as anode catalyst. The metal loadings for anode and cathode were kept at 2 mg cm^{-2} and 0.8 mg cm^{-2} respectively. The MEA was made by sandwiching catalyst coated gas diffusion layer (GDL) on Nafion 115 membrane. The cell was operated at 80 ^oC with 2, 5, and 10 M methanol at a flow rate of 5 mL min^{-1}.

4.3 RESULTS AND DISCUSSIONS

4.3.1 Pt-Pd-Co alloy system

The high boiling, highly viscous tetraethylene glycol (TEG) used as the organic solvent not only acts as a reducing agent but also restricts agglomeration of the nanoparticles. Since the reduction potentials of Pt (+1.2 V vs. NHE) and Pd (+0.92 V) are higher than that of Co (-0.28 V), both Pt and Pd are reduced easily compared to Co. Moreover, the addition of NaOH to the reaction mixture results in the formation of $Co(OH)_2$ primary nano-particles as seen in Fig. 4.2, which may act as seeds for the nucleation and growth of Pt and Pd. The formation of the Pt-Pd-Co nanoalloy took place inside the reactor during the MW-ST process within 15 min at 300 ^oC and 80 bar.

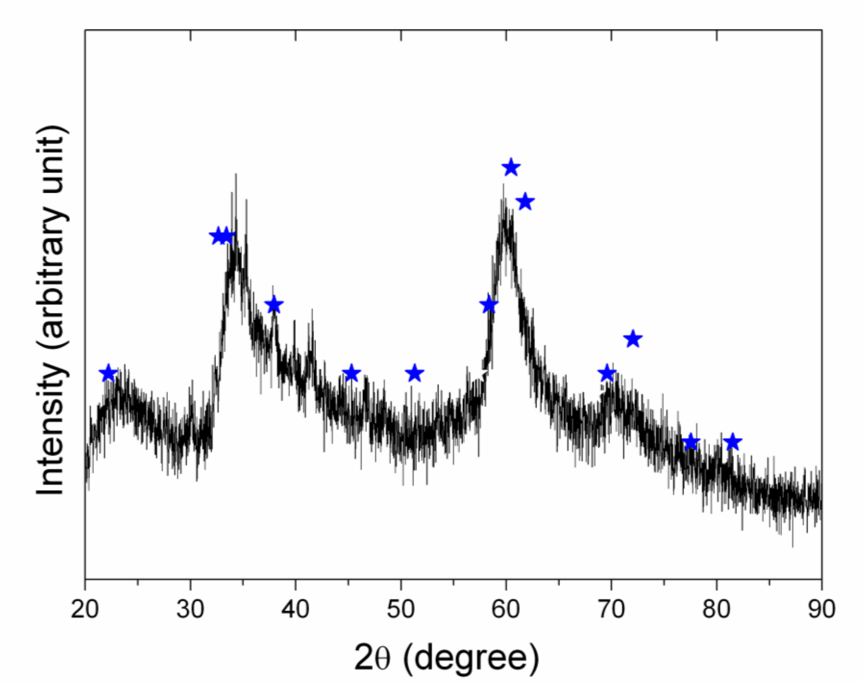

Figure 4.2. The XRD patterns obtained after the addition of NaOH to a solution of $CoCl_2.6H_2O$ in TEG, followed by centrifuging with excess acetone and drying. The blue star (*) refer to $Co(OH)_2$ (PDF#00-002-0925).

Figure 4.3 compares the XRD patterns of $Pt_{75}Co_{25}$, $Pt_{70}Pd_{20}Co_{10}$, and $Pt_{50}Pd_{30}Co_{20}$ synthesized by the MW-ST method at 300 °C for 15 minutes without any post-annealing. All the samples have a single phase fcc structure. The reflections shift to higher angles compared to that in Pt and the lattice parameter values decrease due to the substitution of smaller Co and Pd for Pt. However, the shift is smaller in the cases of $Pt_{70}Pd_{20}Co_{10}$ and $Pt_{50}Pd_{30}Co_{20}$ compared to that in $Pt_{75}Co_{25}$ as Pd is larger than Co. The XRD data reveal the formation of alloy catalysts with a high degree of alloying at lower temperatures within a short reaction time. The degree of alloying (Co content in the alloy lattice) in the binary $Pt_{75}Co_{25}$ and ternary $Pt_{70}Pd_{20}Co_{10}$ and $Pt_{50}Pd_{30}Co_{20}$ alloys was evaluated using the lattice parameter values based on the empirical Vegard's law (equation 4.1). For example, for the binary Pt-Co system, the lattice parameter of the alloy (denoted as a_{alloy}) can be described as a linear combination of the lattice parameters of Pt (denoted as a_{Pt}) and Co (denoted as a_{Co}) as

$$a_{alloy} = x a_{Co} + (1 - x) a_{Pt} \quad [4.1]$$

where x refers to the atom fraction of Co in the Pt-Co alloy.

For the ternary system consisting of Pt, Pd, and Co, a modified version as described in equation 4.2 was used to evaluate the degree of alloying (Co content in the alloy lattice). It was assumed that the atomic ratio of Pd (denoted as y) to Pt was same as that in the nominal composition since Pt-Pd forms homogenous solid solution at all atomic ratios.

$$a_{alloy} = x a_{Co} + y a_{Pd} + (1 - x - y) a_{Pt} \quad [4.2]$$

The lattice parameter and the degree of alloying for the $Pt_{75}Co_{25}$, $Pt_{70}Pd_{20}Co_{10}$, and $Pt_{50}Pd_{30}Co_{20}$ samples synthesized by the MW-ST method are listed in Table 4.1.

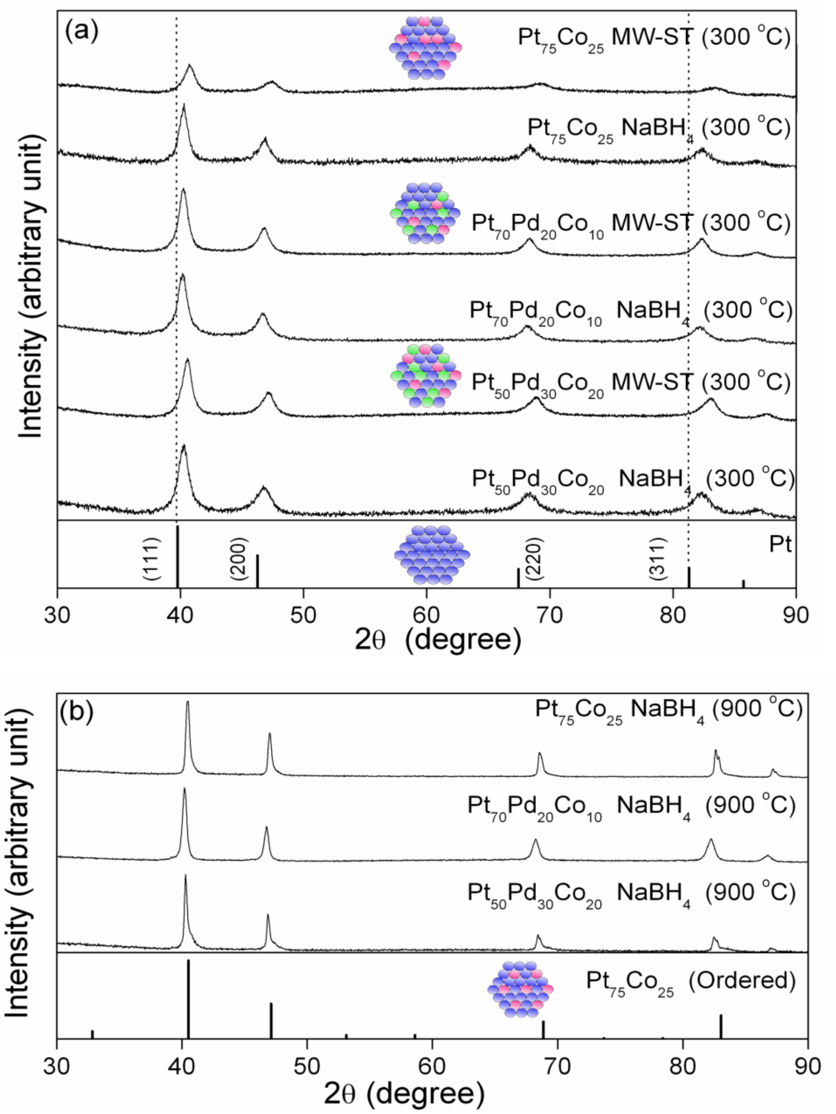

Figure 4.3. XRD patterns of the (a) $Pt_{75}Co_{25}$, $Pt_{70}Pd_{20}Co_{10}$, and $Pt_{50}Pd_{30}Co_{20}$ nanoalloys synthesized by the MW-ST method at 300 °C along with samples obtained by the conventional borohydride method, followed by heating at 300 °C and (b) $Pt_{75}Co_{25}$, $Pt_{50}Pd_{30}Co_{20}$, and $Pt_{70}Pd_{20}Co_{10}$ samples prepared by the conventional brohydride reduction method, followed by heat treatment at 900 °C. Also, the positions of the diffraction peaks expected for Pt (PDF #00-004-0802) and Pt_3Co (PDF #00-029-0499) are indicated at the bottom.

Table 4.1. Compositional analysis, lattice parameters, and degree of alloying of the samples synthesized by the MW-ST method.

Catalyst	Composition as determined by SEM-EDS	Lattice parameter (Å)	Cell volume (Å^3)	Atom % Co in the alloy
Pt		3.921	60.26	-
$Pt_{75}Co_{25}$	$Pt_{77.1}Co_{22.8}$	3.841	56.67	22.3
$Pt_{70}Pd_{20}Co_{10}$	$Pt_{67.3}Pd_{25.4}Co_{7.3}$	3.886	58.70	9.6
$Pt_{50}Pd_{30}Co_{20}$	$Pt_{49.7}Pd_{37.3}Co_{13.0}$	3.855	57.30	18.8

The XRD patterns of the MW-ST samples and the conventional borohydride samples heat treated at 300 ^{o}C and 900 ^{o}C are shown in Figs. 4.3 (a) and (b). The XRD patterns and the lattice parameter values of the samples heat treated at various temperatures up to 900 ^{o}C are compared in Table 4.2. However, it was found that the reflections of $Pt_{75}Co_{25}$ and $Pt_{50}Pd_{30}Co_{20}$ synthesized by conventional borohydride method after heat treatement at 700 - 900 ^{o}C were highly asymmetric, particularly at higher angles, and the reflections could be fitted with two phases having different lattice parameters as seen in Table 4.2. Although there is no clear trend, it was observed that the lattice parameter (3.889 Å) of $Pt_{70}Pd_{20}Co_{10}$ after heat treatment at 500 ^{o}C (Table 4.2) is comparable to the lattice parameter (3.886 Å) of $Pt_{70}Pd_{20}Co_{10}$ sample synthesized by the MW-ST method at 300 ^{o}C (Table 4.1). This suggests that the MW-ST method is much more effective to give samples with a high degree of alloying at lower temperatures

Table 4.2 Compositional analysis and structural characterization data of the $Pt_{75}Co_{25}$, $Pt_{50}Pd_{30}Co_{20}$, and $Pt_{70}Pd_{20}Co_{10}$ samples prepared by the conventional borohydride reduction method followed by heat treatment at various temperatures

Catalyst	Composition as determined by SEM - EDS	Heat treatment temperature (°C)	Structure type (space group)	Lattice parameter (Å)
$Pt_{75}Co_{25}$	$Pt_{76.7}Co_{23.3}$	As-synthesized	Pt (225)	3.899
		300	Pt (225)	3.880
		500	Pt (225)	3.882
		700	Pt (225)	3.875
			Pt_3Co(221)	3.858
		900	Pt (225)	3.874
			Pt_3Co(221)	3.869
$Pt_{70}Pd_{20}Co_{10}$	$Pt_{67.4}Pd_{23.1}Co_{9.5}$	As-synthesized	Pt (225)	3.908
		300	Pt (225)	3.896
		500	Pt (225)	3.889
		700	Pt (225)	3.889
		900	Pt (225)	3.890
$Pt_{50}Pd_{30}Co_{20}$	$Pt_{48.3}Pd_{37.1}Co_{14.6}$	As-synthesized	Pt (225)	3.891
		300	Pt (225)	3.892
		500	Pt (225)	3.879
		700	Pt (225)	3.879
			Pt_3Co (221)	3.835
		900	Pt (225)	3.872
			Pt_3Co (221)	3.875

Figure 4.4 shows the TEM images and particle size distributions of bimetallic $Pt_{75}Co_{25}$ and trimetallic $Pt_{70}Pd_{20}Co_{10}$ and $Pt_{50}Pd_{30}Co_{20}$ nanoalloys synthesized by the MW-ST method. The samples show narrow size distribution with particle sizes ranging from 7 – 20 nm. The TEM images also reveal the absence of any agglomeration of the alloy particles on the surface of carbon. The high resolution TEM images in Fig. 4.4 indicate the well-defined crystalline nature of the as-synthesized samples obtained by the MW-ST method.

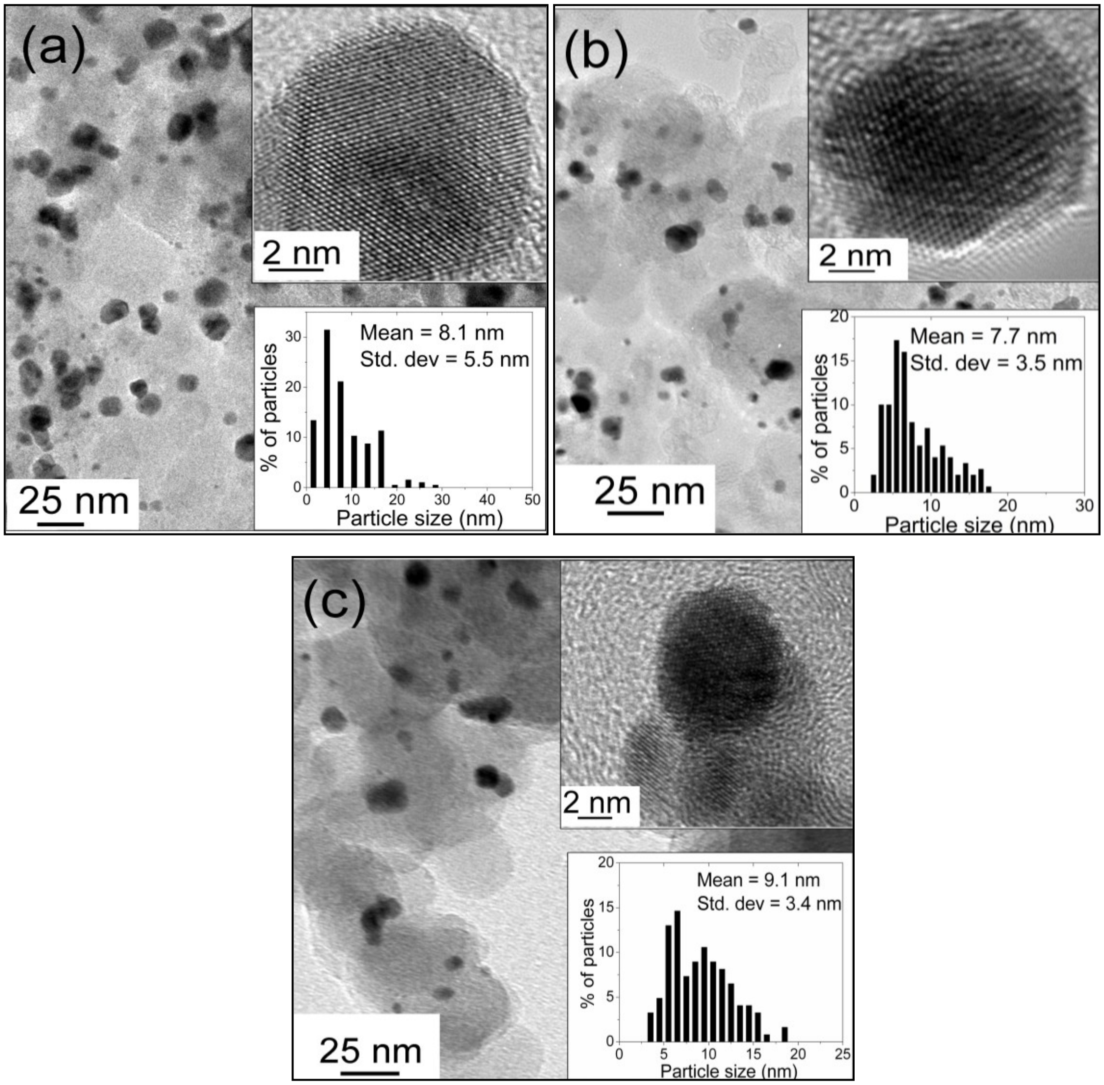

Figure 4.4 TEM images of the (a) $Pt_{75}Co_{25}$, (b) $Pt_{70}Pd_{20}Co_{10}$, and (c) $Pt_{50}Pd_{30}Co_{20}$ samples synthesized by the MW-ST method. The insets show the particle size distribution and HR-TEM images.

Figures 4.5(a) - (c) show the Pt 4*f*, Pd 3*d*, and Co 2*p* core level X-ray photoelectron spectroscopic (XPS) profiles of $Pt_{75}Co_{25}$, $Pt_{70}Pd_{20}Co_{10}$, and $Pt_{50}Pd_{30}Co_{20}$ synthesized by the MW-ST method. Deconvolution of the Pt profiles shows a lower binding energy (Pt $4f_{7/2}$: 70.9 eV) component of metallic Pt^0 and a higher binding energy (Pt $4f_{7/2}$: 72.4 eV) component corresponding to surface oxides of Pt such as PtO (Pt^{2+}) and PtO_2 (Pt^{4+}) as indicated in Fig. 4.5(a). Similarly, the data in Fig 4.5(b) reveal the presence of metallic Pd (Pd $3d_{5/2}$: 335.1 eV) and Pd oxides (Pd $3d_{5/2}$: 335.7 eV). The Pt : Pd ratios in $Pt_{70}Pd_{20}Co_{10}$ and $Pt_{50}Pd_{30}Co_{20}$ were evaluated to be, respectively, 82 : 12 and 66 : 33 from the integrated peak intensities. Interestingly, no detectable peaks corresponding to either metallic Co or Co oxides could be seen in Fig. 4.5(c). This suggests that the concentration of Co in the surface of these multimetallic nanoalloys is very low. However, the EDS elemental analysis in SEM clearly reveals the presence of Co in these multimetallic alloys (Table 4.1). The results suggest that the cobalt hydroxide formed initially acts as seeds for the precipitation of Pt and Pd during the MW-ST process to produce a "core-shell" structure with Pt and Pd enrichment on the surface. This is further supported by the fact that XPS peaks corresponding to Co could be readily observed with the as-synthesized samples obtained by the conventional borohydride method as seen in Fig. 4.5(d). Unlike in the MW-ST method, all the metals are formed more or less simultaneously during the conventional borohydride reduction, resulting in Co along with Pt and Pd on the surface as well.

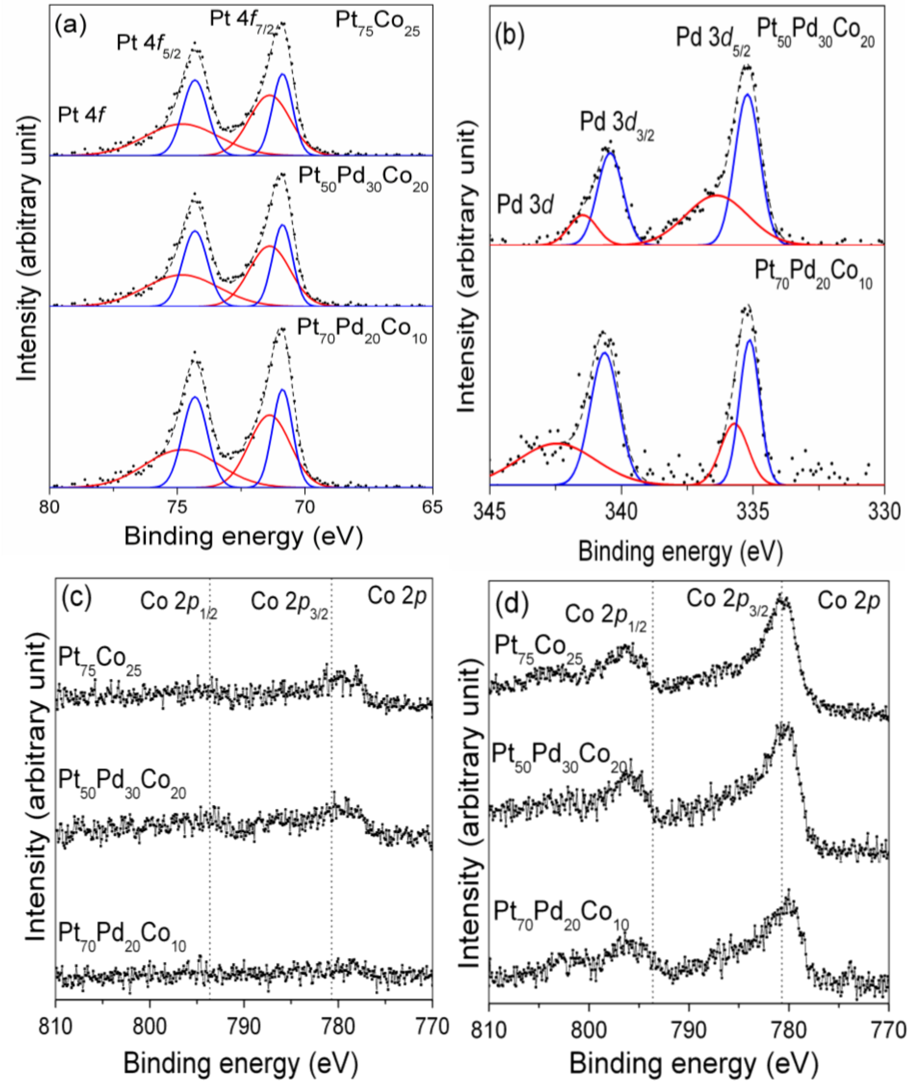

Figure 4.5. Core level XPS profiles (dots) of the (a) Pt 4f and (b) Pd 3d regions and the corresponding fitting results (dotted line) of the $Pt_{75}Co_{25}$, $Pt_{50}Pd_{30}Co_{20}$, and $Pt_{70}Pd_{20}Co_{10}$ samples obtained by the MW-ST method. A comparison of the Co 2p spectra of the samples synthesized by the (c) MW-ST and (d) the conventional $NaBH_4$ methods is also shown. The red and blue lines in (a) and (b) refer to metallic and oxide peaks respectively. The dotted lines in (c) and (d) refer to the expected positions of the Co 2p peaks.

The RDE data given in Fig. 4.6(a) compares the catalytic activity for ORR of the samples synthesized by the MW-ST method with that of commercial Alfa Aesar HiSpec 3000 sample having 20 wt. % Pt supported on carbon. The characteristic sigmoidal shape of the polarization curve of the $Pt_{70}Pd_{20}Co_{10}$ sample is shifted to more positive potentials compared to those of $Pt_{75}Co_{25}$ and $Pt_{50}Pd_{30}Co_{20}$, indicating the higher ORR activity of $Pt_{70}Pd_{20}Co_{10}$ with much lower over-potentials. The Tafel slopes in the region below 0.8 V for the as-synthesized $Pt_{75}Co_{25}$, $Pt_{70}Pd_{20}Co_{10}$, $Pt_{50}Pd_{30}Co_{20}$, and commercial Pt were evaluated to be, respectively, 119, 104, 97, and 112 mV dec^{-1} from the plots in the inset of Fig. 4.6(a). The slope corresponds to 2 x 2.3RT/F, where the reaction proceeds on oxide and hydroxide free surfaces and the adsorption of O_2 follows Langmuir conditions. Moreover, the kinetic current density values at 0.9 V (Fig. 4.6(b)) clearly show that the ORR activity of $Pt_{70}Pd_{20}Co_{10}$ is comparable to that of commercial Pt. Considering the electrochemical surface area values (51.78, 52.30, 47.80 cm^2 mg^{-1}, respectively, for $Pt_{75}Co_{25}$, $Pt_{70}Pd_{20}Co_{10}$, and $Pt_{50}Pd_{30}Co_{20}$) deduced from cyclic voltammetry (CV) plots (Fig. 4.7) and the activity for ORR per unit mass of Pt ($Pt_{70}Pd_{20}Co_{10} > Pt_{50}Pd_{30}Co_{20} > Pt_{75}Co_{25}$), the addition of Pd to Pt-Co alloys intrinsically enhances the activity for ORR. Although the electrochemical surface area (ECSA) of Pt-Pd-Co nanoalloy electrocatalysts are lower than commercial Pt, the enhancement in ORR activity of Pt-Pd-Co alloys clearly demonstrate the synergistic effect of alloy formation by the MW-ST method. Moreover, since the concentration of Pd in the nanoalloy electrocatalysts ($Pt_{70}Pd_{20}Co_{10}$) is low, the absorption of hydrogen which causes uncertainty in reliable estimate of electrochemical active surface area has been assumed negligible.

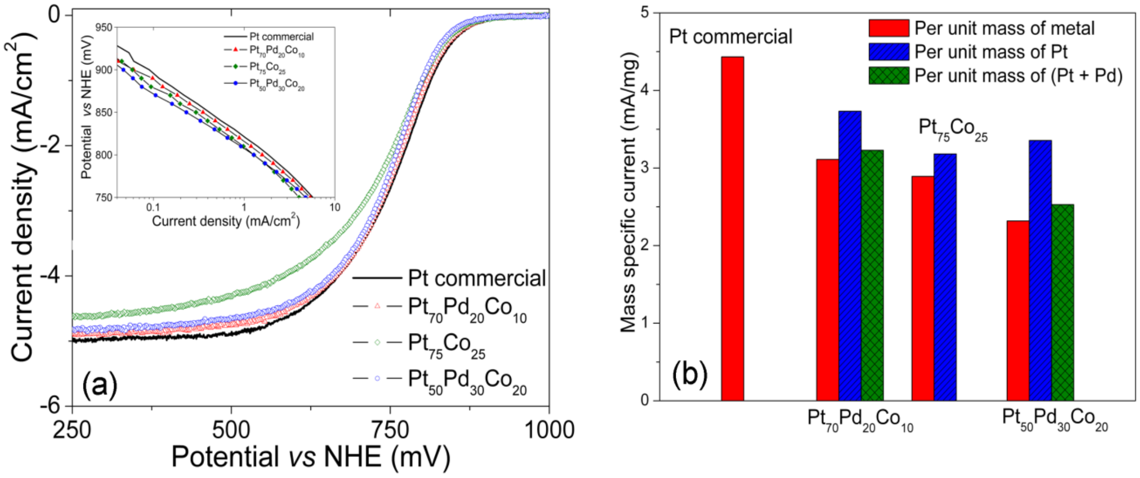

Figure 4.6. Hydrodynamic polarization curves of the $Pt_{75}Co_{25}$, $Pt_{70}Pd_{20}Co_{10}$, $Pt_{50}Pd_{30}Co_{20}$ samples synthesized by the MW-ST method and commercial Pt in 0.5 M H_2SO_4 at 1600 rpm with the insets showing the Tafel plots and (b) mass specific currents at 0.9 V *vs* NHE on per unit mass, per unit mass of Pt, and per unit mass of noble metal basis.

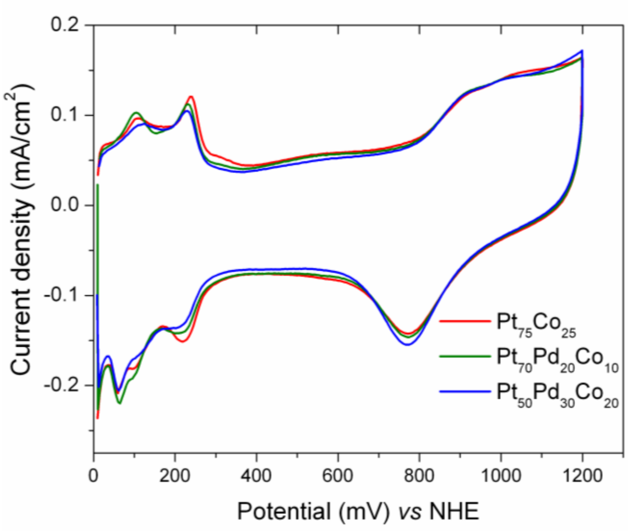

Figure 4.7. Cyclic voltammograms of the $Pt_{75}Co_{25}$, $Pt_{70}Pd_{20}Co_{10}$, and $Pt_{50}Pd_{30}Co_{20}$ samples synthesized by the MW-ST method at 50 mV/s in N_2 saturated 0.5 M H_2SO_4.

Koutecky–Levich plots derived from hydrodynamic polarization curves (Fig. 4.8) obtained at various rotation rates for $Pt_{70}Pd_{20}Co_{10}$ clearly illustrate that the oxygen reduction pathway in this multimetallic alloy system follows a four-electron transfer (n = 4). The Koutecky–Levich plots were obtained for $Pt_{70}Pd_{30}Co_{20}$ using equation (4.3) below:

$$\frac{1}{i_l} = \frac{1}{0.62nFA\,D^{\frac{2}{3}}\gamma^{\frac{-1}{6}}C_o\,\omega^{\frac{1}{2}}} \qquad [4.3]$$

where, i_l is the limiting current in A, n is the total number of electrons transferred, F is the Faraday constant (96485 C mol^{-1}), A is the area of the electrode (0.1963 cm^2), D is the diffusion coefficient of oxygen in cm^2 s^{-1}, C is the concentration of oxygen in mol cm^{-3}, υ is the kinematic viscosity in cm^2 s^{-1}, and ω is the rotation rate in rads^{-1}. The values of D,

C, and υ were taken to be, respectively, 18×10^{-6} cm^2 s^{-1}, 1.13×10^{-6} mol cm^{-3}, and 8.93×10^{-3} cm^2 s^{-1} [9,162]. The kinetic currents were evaluated from equation (4.4),

$$\frac{1}{i} = \frac{1}{i_l} + \frac{1}{i_k} \qquad [4.4]$$

where, i_l is the limiting current, i_k is the kinetic current, and i is the total current.

Also, all the points lying on a straight line passing through zero infer that the thin Nafion film is transparent to diffusion of oxygen during ORR.

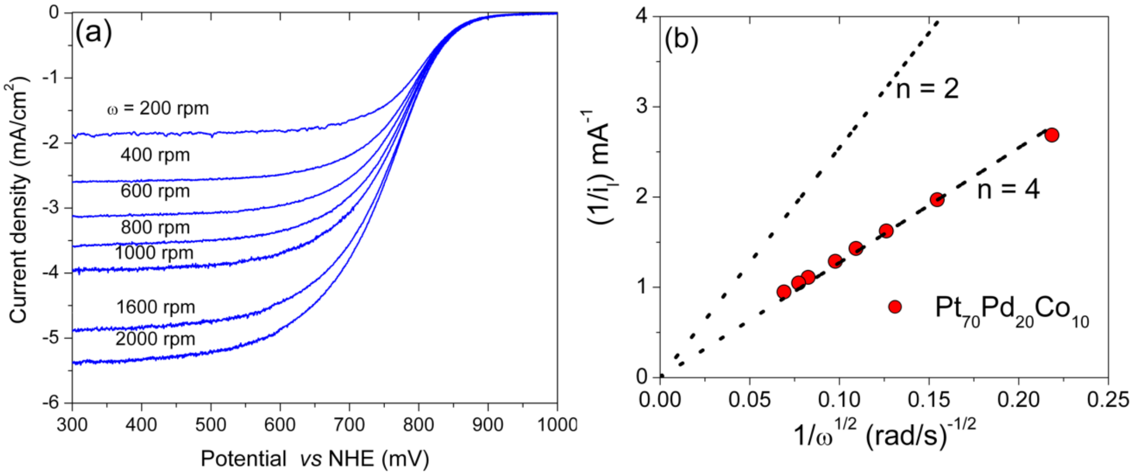

Figure 4.8. (a) Hydrodynamic polarization curves of $Pt_{70}Pd_{20}Co_{10}$ at various rotation rates and (b) the Koutecky-Levich plot (n refers to number of electrons transferred).

The ORR activities of the $Pt_{75}Co_{25}$, $Pt_{70}Pd_{20}Co_{10}$, and $Pt_{50}Pd_{30}Co_{20}$ samples synthesized by the conventional borohydride method after heat treatment at various temperatures (300 - 900 ^{o}C) were also determined. The polarization curves of the $Pt_{75}Co_{25}$, $Pt_{70}Pd_{20}Co_{10}$, and $Pt_{50}Pd_{30}Co_{20}$ samples synthesized by the conventional borohydride method after heat treatment at 300 ^{o}C is presented in Fig. 4.9(a) and a comparison between the MW-ST samples and the conventional borohydride samples after heat treatment at 300 – 900 ^{o}C is presented in Fig. 4.9(b). The kinetic current values at 0.8 V evaluated after correcting for mass transfer reveal that the ORR activities of the multimetallic samples synthesized by the MW-ST method are several times higher than those of the samples synthesized by the conventional borohydride method.

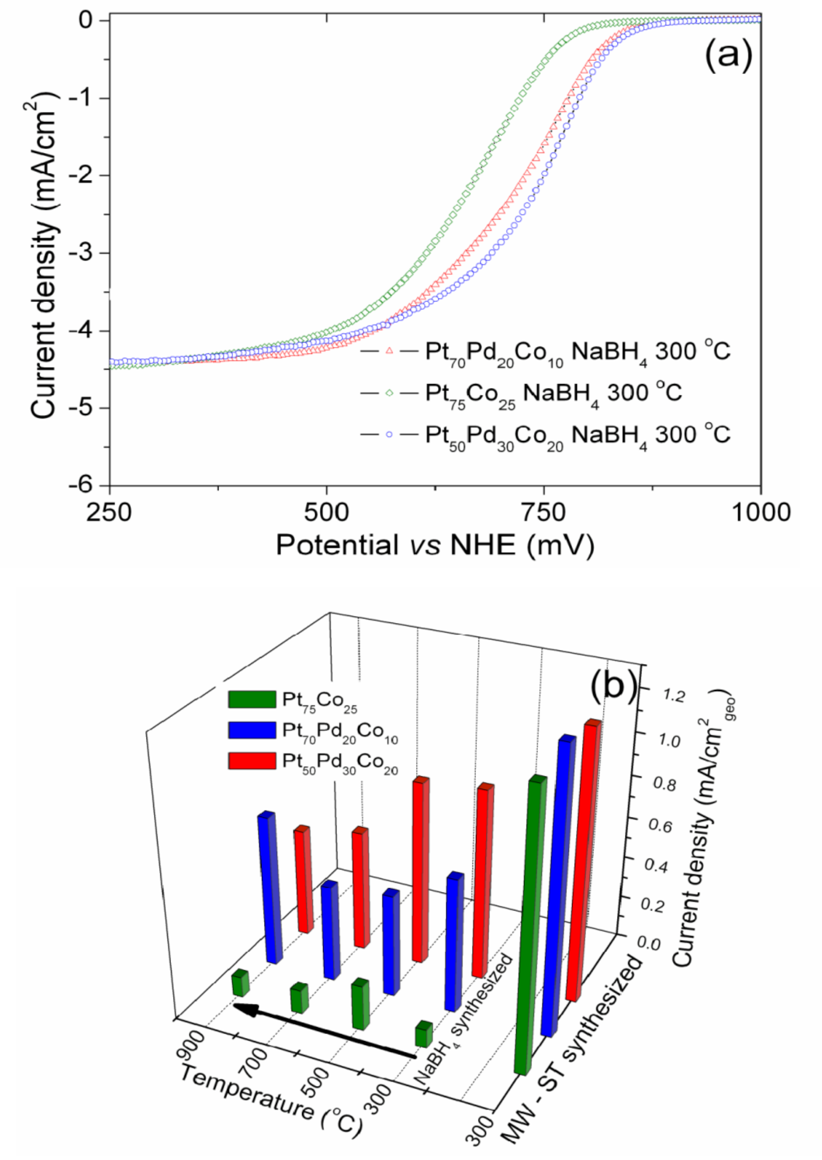

Figure 4.9. (a) Hydrodynamic polarization curves of the $Pt_{75}Co_{25}$, $Pt_{70}Pd_{20}Co_{10}$, $Pt_{50}Pd_{30}Co_{20}$ samples synthesized by the conventional $NaBH_4$ method and (b) comparison of the kinetic current density at 0.8 V *vs* NHE of the $Pt_{75}Co_{25}$, $Pt_{70}Pd_{20}Co_{10}$, and $Pt_{50}Pd_{30}Co_{20}$ samples synthesized by the MW-ST method at 300 °C and conventional borohydride method followed by heat treatment at 300 – 900 °C.

Figure 4.10 compares the single cell proton exchange membrane fuel cell (PEMFC) performances of commercial Pt, $Pt_{70}Pd_{20}Co_{10}$, and $Pt_{75}Co_{25}$ at 60 °C. Similar to the RDE results obtained earlier, the performances of $Pt_{70}Pd_{20}Co_{10}$ have been found to be close to commercial Pt and higher that of $Pt_{75}Co_{25}$.

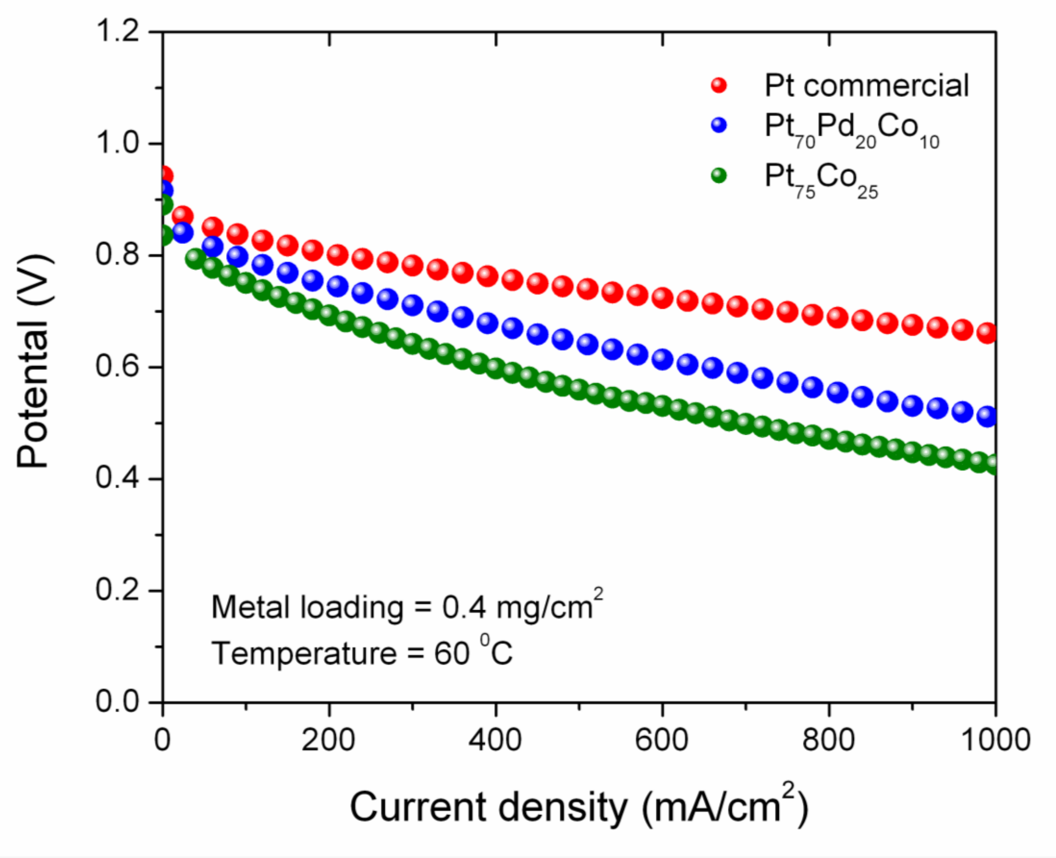

Figure 4.10. ORR activities of commercial the Pt, $Pt_{70}Pd_{20}Co_{10}$, and $Pt_{75}Co_{25}$ samples synthesized by the MW-ST method in a single cell proton exchange membrane fuel cell (PEMFC) at 60 °C.

Figure 4.11 (a) compares the CV plots of the $Pt_{75}Co_{25}$, $Pt_{70}Pd_{20}Co_{10}$, $Pt_{50}Pd_{30}Co_{20}$ samples synthesized by the MW-ST method and commercial Pt for the methanol oxidation reaction. The onset potential for methanol oxidation with the $Pt_{75}Co_{25}$ sample is found to be almost 0.45 V. Addition of Pd as in the case of $Pt_{70}Pd_{20}Co_{10}$ shifts the potential positive by almost 0.2 to 0.65 V. However, no noticeable current due to methanol oxidation is observed with the $Pt_{50}Pd_{30}Co_{20}$ sample even at 0.8 V. Thus, increase in Pd content can increase the tolerance to methanol poisoning. Particularly, the $Pt_{50}Pd_{30}Co_{20}$ sample shows high tolerance to methanol, which is not surprising, considering the well-known inactivity of Pd for methanol oxidation and the high surface concentration of Pd (almost 33 atom %) in $Pt_{50}Pd_{30}Co_{20}$ as revealed by XPS. Adsorption of methanol involves three adjacent Pt atoms, which becomes statistically difficult at higher surface concentrations of Pd. Figure 4.11(b) compares the catalytic activities of $Pt_{50}Pd_{30}Co_{20}$ and commercial Pt for ORR in DMFC. As seen, $Pt_{50}Pd_{30}Co_{20}$ shows superior activity at higher methanol concentrations compared to commercial Pt due to its remarkable tolerance to methanol.

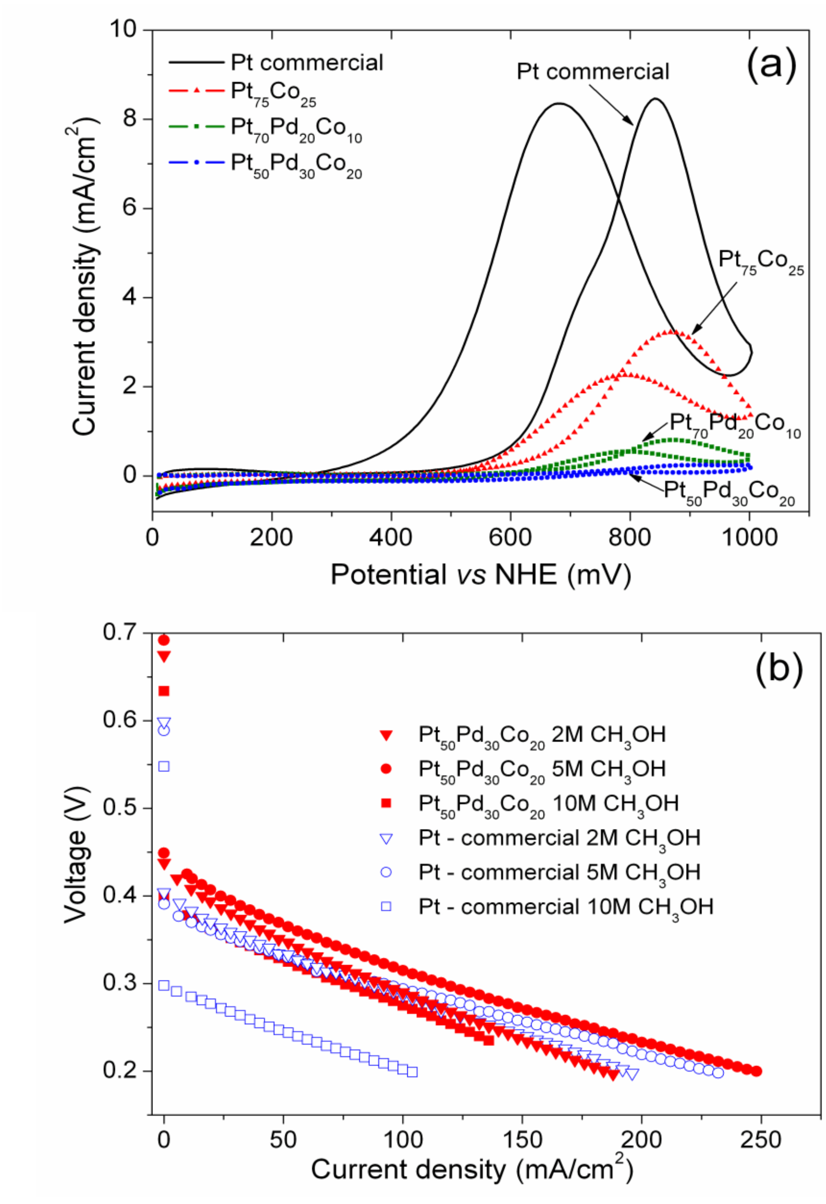

Figure 4.11 Comparison of the (a) cyclic voltammograms of the $Pt_{75}Co_{25}$, $Pt_{70}Pd_{20}Co_{10}$, and $Pt_{50}Pd_{30}Co_{20}$ samples synthesized by the MW-ST method and commercial Pt in N_2 saturated 0.5 M H_2SO_4 + 1 M CH_3OH solution and (b) ORR activities of the $Pt_{50}Pd_{30}Co_{20}$ sample synthesized by the MW-ST method and commercial Pt in single cell direct methanol fuel cell (DMFC) at 80 °C with various concentrations (2 – 10 M) of methanol fuel.

4.3.2 Pt encapsulated Pd-Co system

Figure 4.12 compares the XRD patterns of the as-synthesized (100-y) wt. % Pd_xCo_{100-x} + y wt. % Pt on 80 wt. % carbon samples prepared by the two-step MW-ST method at 300 ^oC and after heat treatment at 900 ^oC in a flowing 10% H_2 – 90% Ar mixture for 2 h. As seen in Fig. 4.12 (a), the as-synthesized 75 wt. % Co_{100} + 25 wt. % Pt exhibit reflections corresponding to mainly cobalt oxide (Co_3O_4). No reflections corresponding to metallic Pt or Pt-Co alloy are seen possibly due to the low concentration of Pt in the carbon-supported electrocatalyst or due to small particle size. Interestingly, incorporation of a small amount of Pd as in the case of 75 wt. % $Pd_{20}Co_{80}$ + 25 wt. % Pt results in reflections corresponding to a metallic fcc phase along with very weak reflections corresponding to Co_3O_4. Additionally, the significant differences in the XRD patterns of the 75 wt. % Co_{100} + 25 wt. % Pt and 75 wt. % $Pd_{20}Co_{80}$ + 25 wt. % Pt samples suggest that the presence of Pd catalyzes the reduction of cobalt ions and facilitates the formation of Pd-Co alloys.

More importantly, the peaks are highly asymmetric to lower two theta values for samples with increasing Pd (Pd : Co ratio > 4 : 6), and the peak positions shift to lower angles with increasing Pd content compared to those of both Pt and Pd, indicating an increase in the degree of alloying between Pd and Co. The highly asymmetric nature of the peaks suggests the presence of two or more phases with similar structures and close lattice parameters. Indeed, a deconvolution of the first 3 peaks located around $2\theta = 40^o$, 45^o, and 65^o, which correspond, respectively, to the (111), (200), and (220) planes of the *fcc* structure, clearly indicates the presence of a primary *fcc* phase with significantly smaller lattice parameter than Pd (a_{Pd} = 3.8902 Å) that corresponds to a Pd-Co alloy and a secondary *fcc* phase with lattice parameter close to that of Pt (a_{Pt} = 3.923 Å). In addition, the peak positions of the primary phase as well as the secondary phase shift gradually to lower 2θ values with increasing Pd content, indicating an expansion of the lattice due to the substitution of smaller Co atoms for larger Pd and Pt atoms. Table 4.3 gives the lattice parameter values of the various samples.

It needs to be pointed out that in the case of 75 wt. % $Pd_{80}Co_{20}$ + 25 wt. % Pt, the lattice parameter of the primary phase (3.844 Å) matches closely with that of 100 wt. % $Pd_{80}Co_{20}$ (3.861 Å) synthesized under the same condition in a single step. The small discrepancy in the lattice parameter could be due to further alloying in the second synthesis step of 75 wt. % $Pd_{80}Co_{20}$ + 25 wt. % Pt. Additionally, the lattice parameter of the secondary phase (3.924 Å) matches closely with that of Pt (3.923 Å). While it is possible that addition of Pt in the second synthesis step results in a primary phase with Pd-rich Pd-Co-Pt alloy and a secondary phase with Pt-rich Pt-Pd-Co alloy, it could not be resolved from the lattice parameter values because of the broad nature of the peaks and the inherent complexity of a trimetallic system. However, in the case of 75 wt. % Pd_{100} + 25 wt. % Pt, the asymmetric nature is much less pronounced and the primary phase has a larger lattice parameter compared to Pd, suggesting alloying between Pt and Pd.

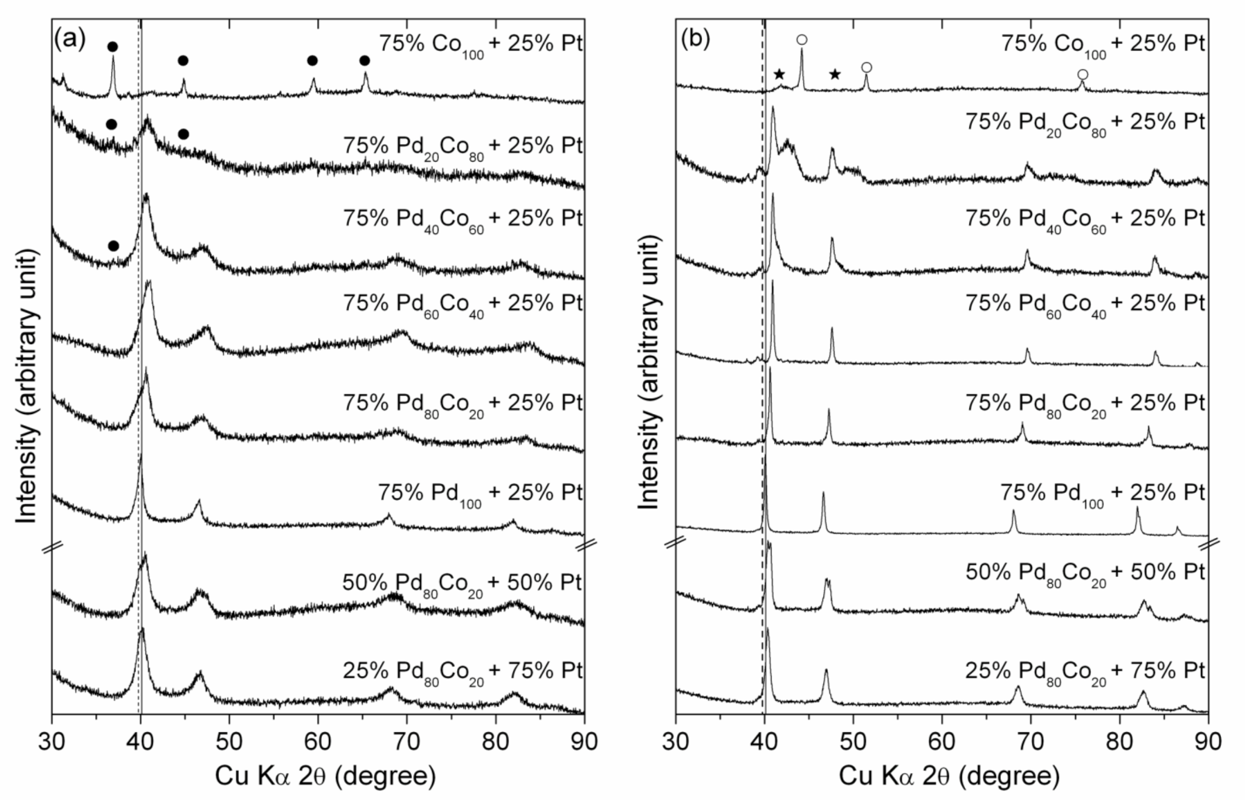

Figure 4.12. XRD patterns of the (a) as-synthesized (100-y) wt. % Pd_xCo_{100-x} + y wt. % Pt (y = 25, 50, and 75) samples obtained by the two-step MW-ST method and (b) 900 ^{o}C heat-treated samples. The solid and the dotted lines refer, respectively, to reflections corresponding to the (111) reflections of Pd and Pt. The reflections marked with ●, ○, and ★ refer, respectively, to Co_3O_4, Co, and ordered PtCo alloy. The % values in the legend refer to wt. %. All the samples have a total metal (Pd_xCo_{100-x} + Pt) loading of 20 wt. % on 80 wt. % carbon and the y = 25, 50, and 75 samples represent, respectively, 5, 10, and 15 wt. % Pt loading on carbon.

Table 4.3. Crystallographic data of the as-synthesized and 900 °C heat treated (100-y) wt. % Pd_xCo_{100-x} + y wt. % Pt samples (all the % values refer to wt. %).

Sample	Heat treatment temperature (°C)	Structure type (space group)	Lattice parameter (Å)
75% $Pd_{20}Co_{80}$ + 25% Pt	As-synthesized	Pd (225)	3.866
75% $Pd_{40}Co_{60}$ + 25% Pt	As-synthesized	Pt (225)	3.872
75% $Pd_{60}Co_{40}$ +25% Pt	As-synthesized	Pt (225)	3.907
		Pd (225)	3.820
75% $Pd_{80}Co_{20}$ + 25% Pt	As-synthesized	Pt (225)	3.924
		Pd (225)	3.844
75% Pd_{100} + 25% Pt	As-synthesized	Pd (225)	3.899
50% $Pd_{80}Co_{20}$ + 50% Pt	As-synthesized	Pt (225)	3.918
		Pd (225)	3.844
25% $Pd_{80}Co_{20}$ + 75% Pt	As-synthesized	Pt (225)	3.897
100% $Pd_{80}Co_{20}$	As-synthesized	Pd (225)	3.861
75% $Pd_{20}Co_{80}$ + 25% Pt	900	Pd (225)	3.811
		Co (225)	3.682
75% $Pd_{40}Co_{60}$ + 25% Pt	900	Pt (225)	3.822
		Co (225)	3.788
75% $Pd_{60}Co_{40}$ + 25% Pt	900	Pt (225)	3.817
75% $Pd_{80}Co_{20}$ + 25% Pt	900	Pd (225)	3.849
75% Pd_{100} + 25% Pt	900	Pd (225)	3.894
50% $Pd_{80}Co_{20}$ + 50% Pt	900	Pt (225)	3.870
		Pd (225)	3.840
25% $Pd_{80}Co_{20}$ + 75% Pt	900	Pt (225)	3.873

Increasing the Pt content while keeping the Pd : Co ratio constant at 4 : 1 on going from 75 wt. % $Pd_{80}Co_{20}$ + 25 wt. % Pt to 50 wt. % $Pd_{80}Co_{20}$ + 50 wt. % Pt results in a noticeable decrease in the asymmetry and a decrease in the lattice parameter of the Pt-rich secondary phase, suggesting a slight increase in the degree of alloying between Pt and Pd . However, the lattice parameter of the primary phase (Pd-rich Pd-Co alloy) remains constant at 3.844 Å. On increasing the Pt content further as in the case of 25 wt. % $Pd_{80}Co_{20}$ + 75 wt. % Pt, the two phases could not be resolved and only one lattice parameter could be obtained. Overall, a small decrease in the lattice parameter of the secondary phase and no increase in the lattice parameter of the primary phase (Table 4.3) on increasing the Pt content while keeping the Pd : Co ratio constant at 4 : 1 strongly suggest the possibility of Pt existing both as separate nanoparticles formed by the nucleation and growth of Pt alone and as Pt-encapsulating on the Pd-Co nanoparticles formed by the nucleation and growth of Pt on the surface of Pd-Co nanoparticles during the second synthesis step. Indeed, Adzic *et al.* [47, 68, 69] have reported a strong asymmetry in the XRD profiles observed for Au-Ni and Pd-Co nanoparticles after heat treatment due to surface segregation and formation of Au- and Pd-rich overlayers, respectively, for Au-Ni and Pd-Co nanoparticles. Similarly, we believe the strong asymmetry observed in the XRD patterns of most of our samples in Figure 1 is partly due to the growth of Pt overlayers on the Pd-Co nanoparticles.

The XRD patterns of the (100-y) wt. % Pd_xCo_{100-x} + y wt. % Pt samples after heat treatment at 900 ^{o}C are presented in Figure 4.12(b). The primary phase in all the samples belonging to the series 75 wt. % Pd_xCo_{100-x} + 25 wt. % Pt after heat treatment at 900 ^{o}C has smaller *fcc* lattice parameter values compared to Pd as evident from a large shift in the peak positions towards higher angles due to an increase in the degree of alloying with Co at higher temperatures. However, the 75 wt. % Co_{100} + 25 wt. % Pt sample consists of metallic *fcc* Co as the primary phase along with the ordered PtCo phase as a secondary phase. Particularly, the 75 wt. % $Pd_{20}Co_{80}$ + 25 wt. % Pt sample after heat treatment at 900 °C consists of two distinct *fcc* phases with lattice parameters of 3.811 Å and 3.682 Å and some impurity phases, which could not be identified. Clearly, the primary phase consists of a Pd-rich Pt-Pd-Co alloy and the secondary phase consists of a Co-rich Pt-Pd-Co alloy. Increasing the Pd content further causes a noticeable increase in the lattice parameter values of the secondary phase (Co-rich alloy) as well as the primary phase (Pd-rich alloy) due to a substitution of larger Pd atoms for smaller Co atoms. Indeed, a single phase with a lattice parameter value of 3.817 Å was observed for the 75 wt. % $Pd_{60}Co_{40}$ + 25 wt. % Pt sample. Increasing the Pd content still further causes an expansion of the primary phase as can be noticed in the XRD pattern of 75 wt. % $Pd_{80}Co_{20}$ + 25 wt. % Pt. Moreover, the 75 wt. % Pd_{100} + 25 wt. % Pt sample shows a lattice parameter of 3.894 Å, which is close to the expected lattice parameter value of 3.895 Å based on Vegard's law for a solid solution between 75 wt. % Pd_{100} and 25 wt. % Pt, indicating full degree of alloying.

Systematic increase in the concentration of Pt while keeping the Pd : Co ratio constant at 4 : 1 results in an expansion of the lattice due to the substitution of larger Pt atoms as can be noticed on going from 75 wt. % $Pd_{80}Co_{20}$ + 25 wt. % Pt to 50 wt. % $Pd_{80}Co_{20}$ + 50 wt. % Pt to 25 wt. % $Pd_{80}Co_{20}$ + 75 wt. % Pt (Fig. 4.12(b)). Interestingly, the XRD pattern of the 50 wt. % $Pd_{80}Co_{20}$ + 50 wt. % Pt reveals the presence of two *fcc* phases with lattice parameters of 3.870 Å and 3.840 Å, indicating the presence of a miscibility gap in the ternary phase diagram of Pt-Pd-Co. To investigate further the phase behavior of the Pt-Pd-Co system with increasing amount of Pt while keeping the Pd : Co ratio constant at 4:1, the 75 wt. % $Pd_{80}Co_{20}$ + 25 wt. % Pt, 50 wt. % $Pd_{80}Co_{20}$ + 50 wt. % Pt, and 25 wt. % $Pd_{80}Co_{20}$ + 75 wt. % Pt samples were each heat treated at 500 and 700 ^{o}C, and the variations of the lattice parameters with heat treatment temperature are shown in Fig. 4.13. The data reveal that the 75 wt. % $Pd_{80}Co_{20}$ + 25 wt. % Pt and 25 wt. % $Pd_{80}Co_{20}$ + 75 wt. % Pt samples form a single phase solid solution with complete alloying after heat treatment at 700 ^{o}C. However, the 50 wt. % $Pd_{80}Co_{20}$ + 50 wt. % Pt sample shows two phases at all temperatures. Interestingly, the lattice parameters of the two phases of the 50 wt. % $Pd_{80}Co_{20}$ + 50 wt. % Pt (3.840 Å and 3.870 Å) match closely with the lattice parameter values of the 75 wt. % $Pd_{80}Co_{20}$ + 25 wt. % Pt (3.849 Å) and 25 wt. % $Pd_{80}Co_{20}$ + 75 wt. % Pt (3.873 Å). Therefore, it can be suggested that the 75 wt. % $Pd_{80}Co_{20}$ + 25 wt. % and 25 wt. % $Pd_{80}Co_{20}$ + 75 wt. % Pt samples are close to the phase boundaries in the Pt-Pd-Co system, and Pt gets redistributed into the Pt-rich phase and the Pt-poor phase.

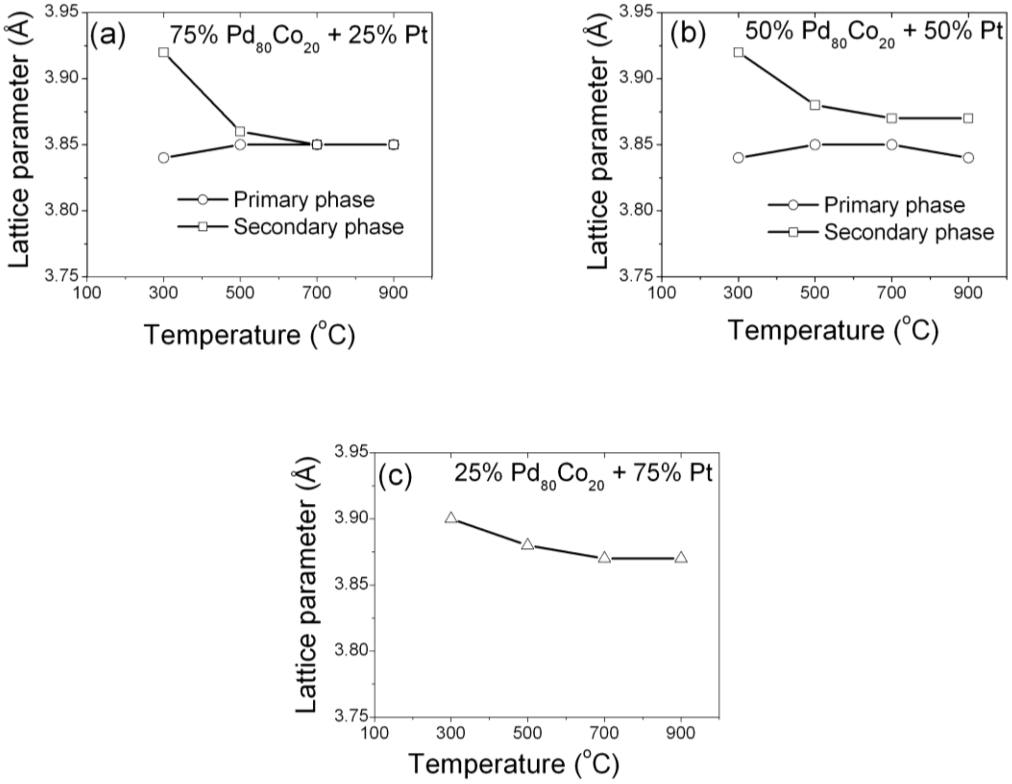

Figure 4.13. Variations of the lattice parameters of (a) 75% $Pd_{80}Co_{20}$ + 25% Pt, (b) 50% $Pd_{80}Co_{20}$ + 50% Pt, and (c) 25% $Pd_{80}Co_{20}$ + 75% Pt with heat treatment temperature. The % values in the legend refer to wt. %.

The particle size and distribution were characterized by TEM and are presented in Figures 4.14(a) and (b). As seen, the as-synthesized 75 wt. % $Pd_{80}Co_{20}$ + 25 wt. % Pt has a mean particle diameter of 11.2 ± 3.6 nm with a narrow particle size distribution without much agglomeration of the nanoparticles. Moreover, the high resolution TEM as shown in the inset of Figure 4.14(a) demonstrates the well crystalline nature of the nanoparticles. However, the Pt nanoparticles synthesized by a one step MS-ST show slightly larger mean particle size of 13.9 ± 3.9 nm. Although, the 75 wt. % $Pd_{80}Co_{20}$ + 25 wt. % Pt sample has been synthesized by a two-step method compared to Pt, the unimodal nature of the particle size distribution indicates either a rapid growth of the individual Pt nanoparticles compared to bimetallic PdCo nanoparticles during the second synthesis step or a nucleation and growth of Pt on the surface of already formed Pd-Co nanoparticles. The closeness of the mean particle sizes suggests that both the above particle growth mechanisms might be occurring simultaneously. Figure 4.14(b) shows the TEM image and the particle size distribution of the 75 wt. % Pd_{100} + 25 wt. % Pt sample after heat treatment at 900 ^{o}C. The data indicate a considerable increase in the mean particle diameter and a broadening of the particle size distribution.

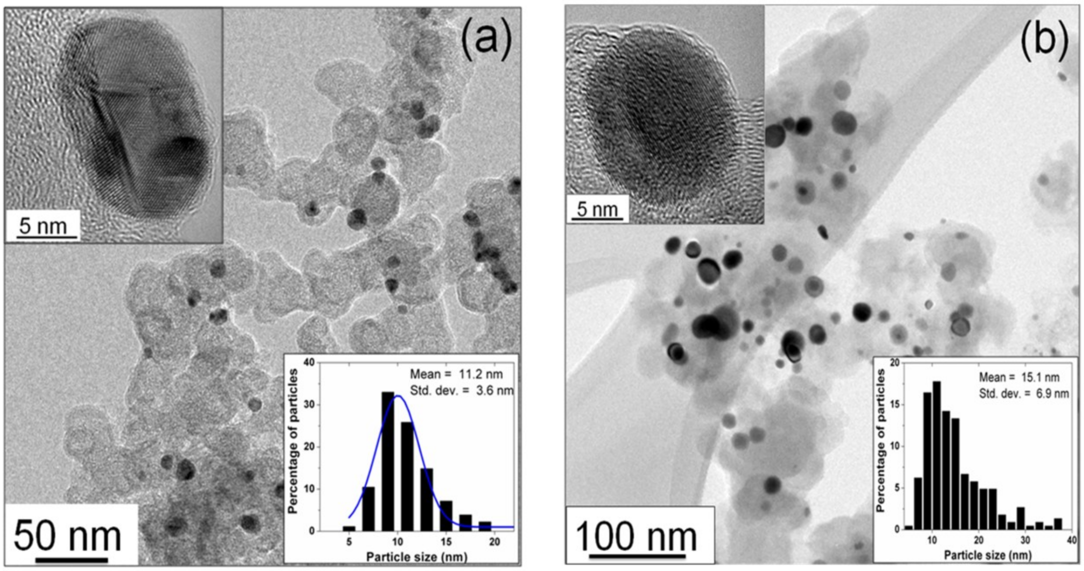

Figure 4.14. TEM images of the (a) as-synthesized and (b) 900 ^{o}C heat-treated 75 wt. % $Pd_{80}Co_{20}$ + 25 wt. % Pt samples. The insets show the particle size distributions and HR-TEM images.

Figures 4.15(a) – (c) shows the Pt 4*f*, Pd 3*d*, and Co 2*p* core level XPS profiles of 75 wt. % Co_{100} + 25 wt. % Pt, 75 wt. % $Pd_{80}Co_{20}$ + 25 wt. % Pt, and 25 wt. % $Pd_{80}Co_{20}$ + 75 wt. % Pt. A decovolution of the Pt 4f profiles as shown in Fig. 4.15(a) clearly indicates a lower bonding energy component corresponding to Pt^0 and higher binding energy components corresponding to surface oxides of Pt such as PtO (Pt^{2+}) and PtO_2 (Pt^{4+}). Similarly, the samples containing Pd reveal the presence of metallic Pd along with oxides on the surface. Interestingly, the XPS signals corresponding to Co or Co oxides are weak in the case of 75 wt. % $Pd_{80}Co_{20}$ + 25 wt. % Pt and no detectable Co signals are observed in 75 wt. % $Pd_{80}Co_{20}$ + 25 wt. % Pt. However, the Co signals could be clearly observed in 75 wt. % Co_{100} + 25 wt. % Pt as seen in Figure 4.15(c). These observations suggest that at both high concentrations of Pt and Pd, the surface is predominantly Pt- and Pd-rich. The absence of Co on the samples with high Pd and Pt contents also suggests that the addition of NaOH in the first synthesis step results in the formation of nanoparticles of cobalt hydroxide that act as nucleation centers for the precipitation of Pd and subsequently the Pd-Co particles act as seeds for the nucleation of Pt. Table 4.4 gives the surface concentrations for all the samples. A comparison of the relative surface concentrations of Pt, Pd, and Co reveals significantly higher surface concentration of Pt, particularly with samples containing higher Pd content. This can be attributed to either large number of smaller Pt particles or formation of Pt surface layers on the already formed Pd-Co nanoparticles during the second synthesis step. Moreover, the XRD data, which shows presence of a secondary phase having a lattice parameter close to that of Pt, as well as the TEM data, which shows the absence of bimodal particle size distribution, strongly support the existence of Pt-encapsulated Pd-Co particles. We would also like to emphasize that XPS is not purely a surface technique and the photoelectrons originate from layers of several atoms thick.

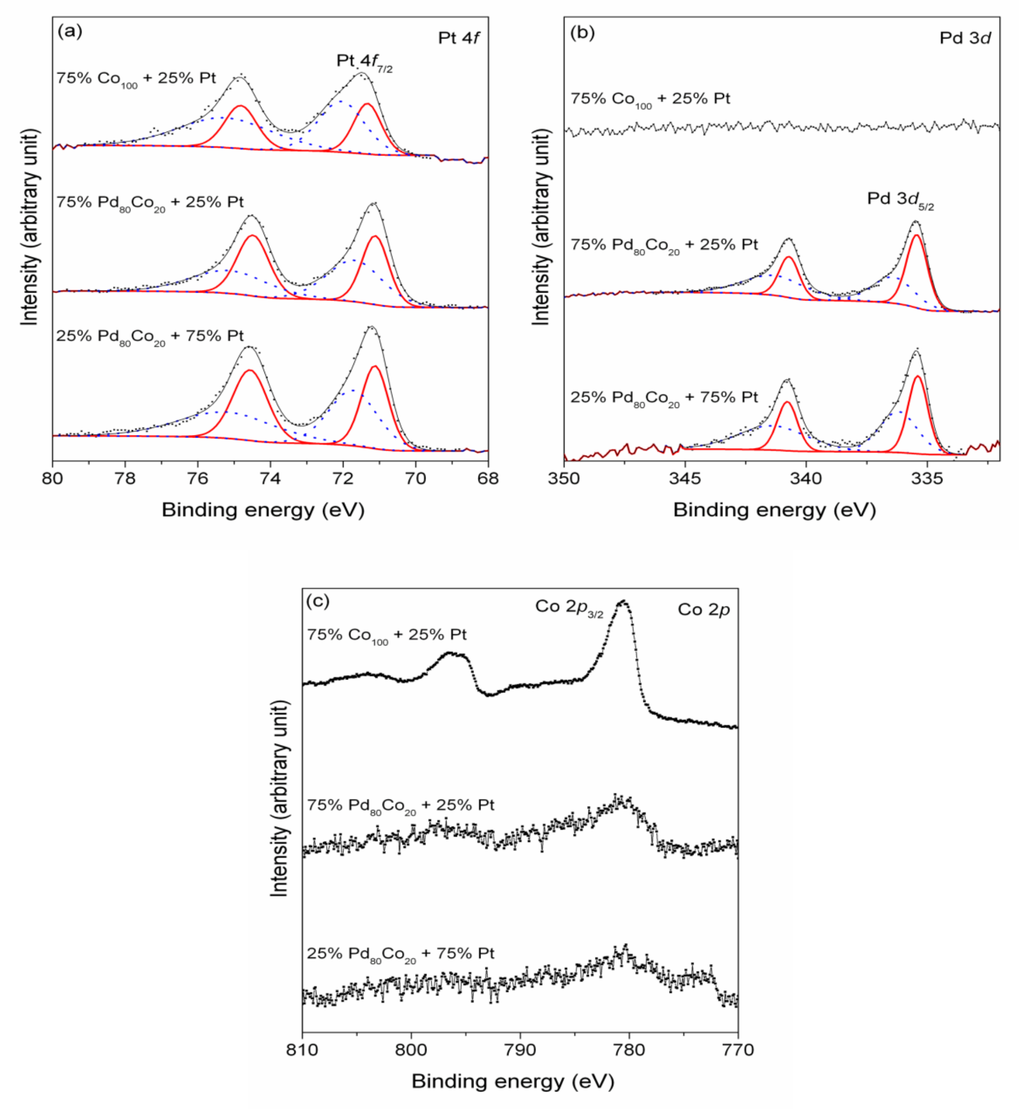

Figure 4.15. Core level XPS profiles (dots) of the (a) Pt 4f, (b) Pd 3d, and (c) Co 2p regions and the corresponding fitting results (dotted line) of the 75 wt. % Co_{100} + 25 wt. % Pt, 75 wt. % $Pd_{80}Co_{20}$ + 25 wt. % Pt, and 25 wt. % $Pd_{80}Co_{20}$ + 75 wt. % Pt samples obtained by the MW-ST method. The red and blue lines in (a) and (b) refer to metallic and oxide peaks respectively.

Table 4.4. Nominal compositions and surface compositions determined from the XPS profiles of the as-synthesized (100-y) wt. % Pd_xCo_{100-x} + y wt. % Pt samples.

Sample[a]	Nominal atomic composition	Surface composition determined by XPS
75% Co_{100} + 25% Pt	$Pt_{9.1}Co_{90.9}$	$Pt_{8.7}Co_{91.3}$
75% $Pd_{20}Co_{80}$ + 25% Pt	$Pt_{10.5}Pd_{17.9}Co_{71.6}$	$Pt_{20.2}Pd_{16.6}Co_{63.2}$
75% $Pd_{40}Co_{60}$ + 25% Pt	$Pt_{11.8}Pd_{35.3}Co_{52.9}$	$Pt_{11.6}Pd_{31.0}Co_{57.4}$
75% $Pd_{60}Co_{40}$ + 25% Pt	$Pt_{13.0}Pd_{52.2}Co_{34.8}$	$Pt_{23.4}Pd_{50.0}Co_{26.6}$
75% $Pd_{80}Co_{20}$ + 25% Pt	$Pt_{14.2}Pd_{68.6}Co_{17.2}$	$Pt_{30.2}Pd_{59.0}Co_{10.8}$
75% Pd_{100} + 25% Pt	$Pt_{15.4}Pd_{84.6}$	$Pt_{30.4}Pd_{69.6}$
50% $Pd_{80}Co_{20}$ + 50% Pt	$Pt_{33.2}Pd_{53.4}Co_{13.4}$	$Pt_{58.7}Pd_{41.3}$
25% $Pd_{20}Co_{80}$ + 75% Pt	$Pt_{59.8}Pd_{32.2}Co_{8.0}$	$Pt_{64.5}Pd_{35.5}$

[a] All the % values refer to wt. %.

Figure 4.16 presents the CVs of selected as-synthesized (100-y) wt. % Pd_xCo_{100-x} + y wt. % Pt samples prepared by the two-step MW-ST method at 300 °C and after heat treatment at 900 °C in a flowing 10% H_2 + 90% Ar mixture for 2 h. As seen in Fig. 4.16(a), absorption of hydrogen in palladium causes significant interference in the CV profiles of 75 wt. % Pd_{100} + 25 wt. % Pt. However, the absorption is significantly less in samples containing Co possibly due to the alloying of Pd with Co.

Additionally, the nearly identical CV profiles observed for the 75 wt. % $Pd_{80}Co_{20}$ + 25 wt. % Pt, 50 wt. % $Pd_{80}Co_{20}$ + 50 wt. % Pt, and 25 wt. % $Pd_{80}Co_{20}$ + 75 wt. % Pt samples suggest that the electrochemical active surface area does not increase with increasing Pt content. Consequently, it may be concluded that the increase in Pt content does not significantly increase the number of individual nanoparticles but results in thicker Pt layers on the Pd-Co nanoparticles. Moreover, after heat treatment at 900 ^{o}C, significantly less hydrogen absorption is seen due to the alloying of Pd with both Co and Pt. In addition, the CV profile of 75 wt. % Pd_{100} + 25 wt. % Pt after heat treatment at 900 ^{o}C shows significantly higher surface oxide reduction peak compared to the other samples. As in the case of as-prepared samples, the CV profiles of 75 wt. % $Pd_{80}Co_{20}$ + 25 wt. % Pt, 50 wt. % $Pd_{80}Co_{20}$ + 50 wt. % Pt, and 25 wt. % $Pd_{80}Co_{20}$ + 75 wt. % Pt are found to be similar. However, no specific trend is observed from the CVs of the as-synthesized or 900 ^{o}C heated samples. Because of the uncertainty in the accurate determination of the adsorption characteristics of hydrogen on Pd [163], Pd alloys [164,165], and Pd/Pt core/shell nanoparticles [166], the electrochemical surface area, which assumes monolayer coverage of hydrogen, could not be determined.

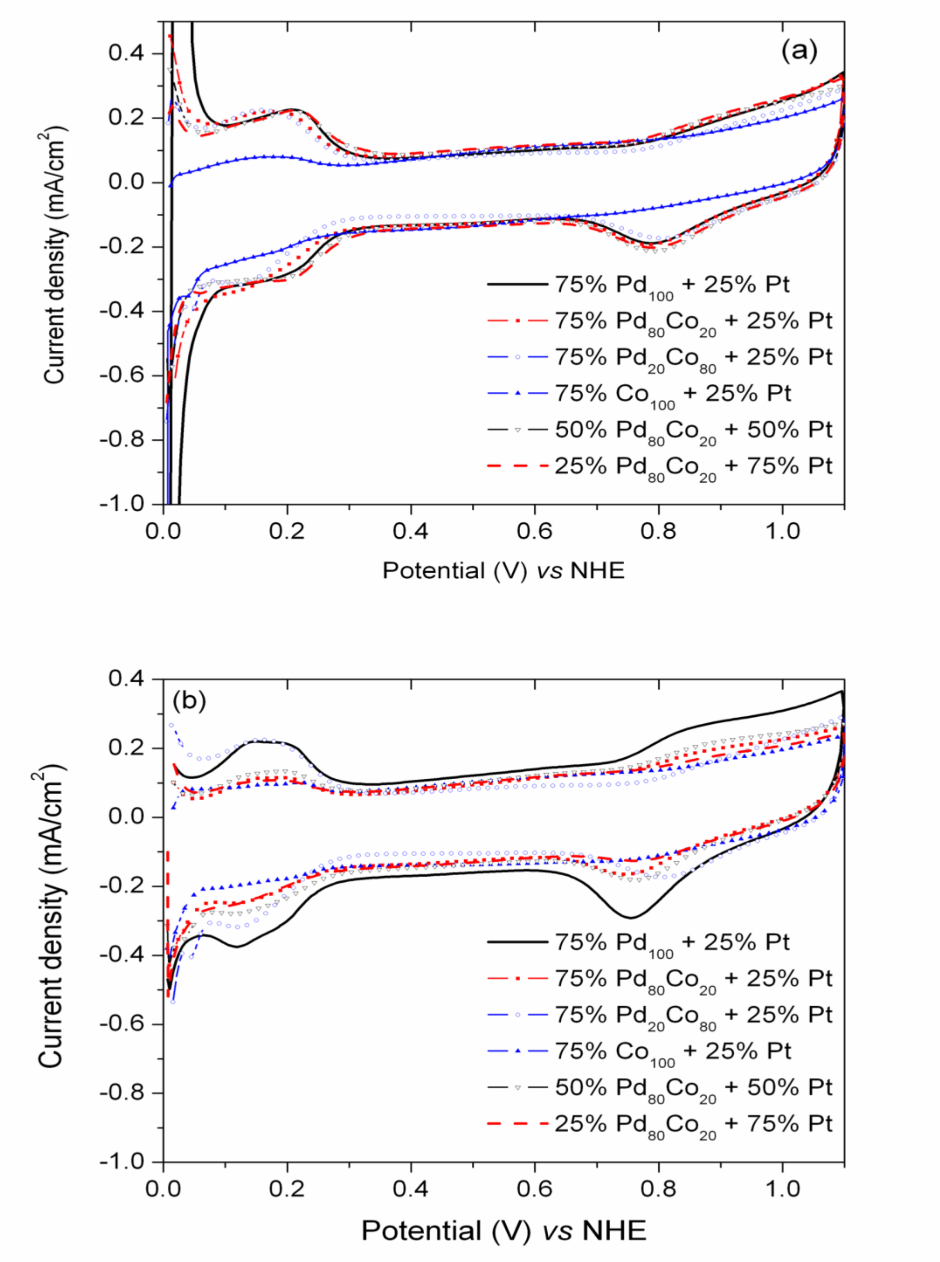

Figure 4.16. Cyclic voltammogramms of selected (a) as-synthesized and (b) 900 °C heat treated (100-y) wt. % Pd$_x$Co$_{100-x}$ + y wt. % Pt samples. The data were collected in N$_2$ saturated 0.5 M H$_2$SO$_4$ at room temperature with a scan rate of 50 mV/s. The % values in the legend refer to wt. %.

The RDE data given in Fig. 4.17(a) compares the ORR activities of the (100-y) wt. % Pd_xCo_{100-x} + y wt. % Pt series of electrocatalysts synthesized by the MW-ST method at 300 ^{o}C along with commercial (Alfa Aesar HiSpec 3000) 20 wt. % Pt supported on carbon. As seen, a clear limiting current is obtained for all the samples. Additionally, as seen in Fig 4.17(a), the characteristic polarization curves shift towards higher potentials with increasing Pd content in the electrocatalyst, indicating an increase in activity with Pd. Indeed the mass-transfer corrected Tafel plots as shown in Fig. 4.17(b) and the variation of the kinetic current density at 0.8 V *vs* NHE with composition as shown in the inset of Fig. 4.17(b) clearly demonstrate a monotonic increase in the activity for ORR with increasing Pd content up to a Pd: Co ratio of 4: 1, and a decrease in activity thereafter. The 75 wt. % $Pd_{80}Co_{20}$ + 25 wt. % Pt sample that has a total metal loading of 20 wt % or a Pt loading of 5 wt. % on carbon shows the maximum activity for ORR. Moreover, the activity of the 75 wt. % $Pd_{80}Co_{20}$ + 25 wt. % Pt sample is significantly higher (~ 10 times) than that of the $Pd_{80}Co_{20}$ sample synthesized by the same method. This clearly indicates that the ORR activity is influenced by the Pt-encapsulation on the $Pd_{80}Co_{20}$ nanoalloys. A comparison of the activities for ORR (kinetic current density at 0.8 V *vs* NHE) of the 75 wt. % $Pd_{80}Co_{20}$ + 25 wt. % Pt sample, the Pt sample synthesized by the single-step MW-ST method, and commercial Pt on the basis of per unit mass of metal is presented in Figure 4.17(c). As seen, the activity for ORR of the 75 wt. % $Pd_{80}Co_{20}$ + 25 wt. % Pt sample is significantly higher than that of 100 % Pt sample synthesized by the single-step MW-ST method. Although the mass based activity of the 75 wt. % $Pd_{80}Co_{20}$ + 25 wt. % Pt sample is lower than that of commercial Pt (Alfa Aesar HiSpec 3000) because of the larger particle size, the activity per unit mass of Pt is considerably higher.

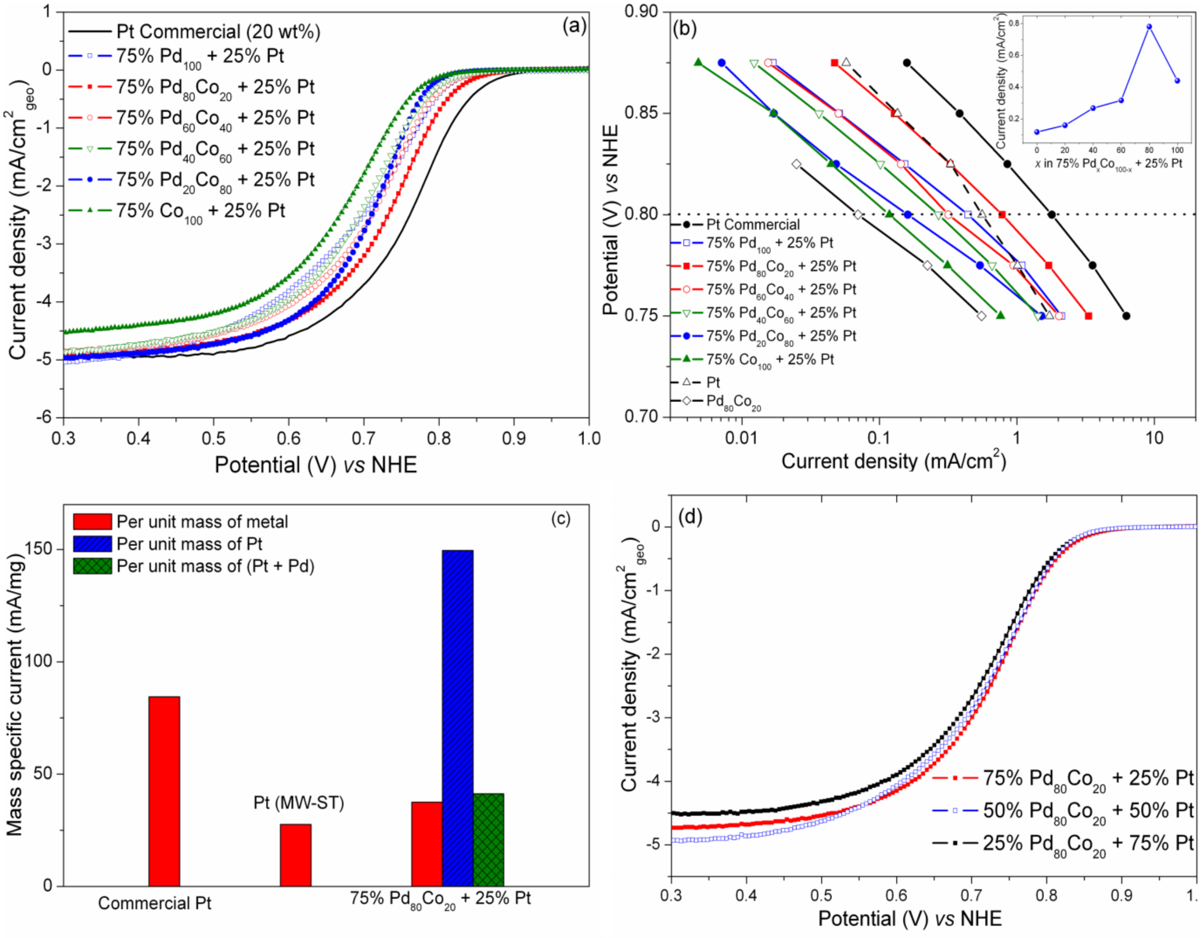

Figure 4.17. (a) Hydrodynamic polarization curves of the as-synthesized (100-y) wt. % Pd_xCo_{100-x} + y wt. % Pt samples along with commercial Pt, (b) mass transfer corrected Tafel plots of the as-synthesized (100-y) wt. % Pd_xCo_{100-x} + y wt. % Pt samples along with as-synthesized Pt, as-synthesized $Pd_{80}Co_{20}$, and commercial Pt, with the inset showing the variation of kinetic current density at 0.8 V *vs* NHE with Pd content, (c) mass specific current density at 0.8 V *vs* NHE on the basis of per unit mass, per unit mass of Pt, and per unit mass of noble metal, and (d) hydrodynamic polarization curves of the as-synthesized 75 wt. % $Pd_{80}Co_{20}$ + 25 wt. % Pt, 50 wt. % $Pd_{80}Co_{20}$ + 50 wt. % Pt, and 25 wt. % $Pd_{80}Co_{20}$ + 75 wt. % Pt samples. The % values in the legend refer to wt. %.

Additionally, increasing the Pt content while keeping the Pd : Co ratio at 4: 1 did not increase the activity for ORR as can be seen in Figure 4.17(d). Although the TEM data do not show the “core-shell” morphology, the XRD and XPS data strongly suggest the presence of Pt-encapsulated Pd-Co nanoparticles along with Pt nanoparticles. Thus, an increase in Pt concentration possibly results in a thicker Pt layer on $Pd_{80}Co_{20}$ nanoparticles, accompanied by a small increase in particle size. This explains the almost identical CV profiles and similar activities for ORR of the 25 wt. % $Pd_{80}Co_{20}$ + 75 wt. % Pt, 50 wt. % $Pd_{80}Co_{20}$ + 50 wt. % Pt, and 25 wt. % $Pd_{80}Co_{20}$ + 75 wt. % Pt samples.

The polarization curves for ORR of the samples after heat treatment at 900 ^{o}C are presented in Figure 4.18. As seen, the electrocatalytic activities for ORR of most of the samples decrease considerably after heat treatment at 900 ^{o}C compared to the as-synthesized samples due to the increase in particle size. The increased activity for ORR of the 75 wt. % Co_{100} + 25 wt. % Pt sample after heat treatment at 900 ^{o}C compared to the as-synthesized sample is possibly due to the formation of ordered PtCo phase as revealed by the XRD data. Addition of Pd to Co increases the activity as seen in the 75 wt. % $Pd_{20}Co_{80}$ + 25 wt. % Pt sample compared to the 75 wt. % Co_{100} + 25 wt. % Pt sample. However, increasing the Pd content further decreases first the activity until a Pd: Co ratio of 3: 2 is attained and then increases the activity until the Co-free Pt-Pd alloy is attained. Overall, the maximum activity for ORR is observed with the 75 wt. % Pd_{100} + 25 wt. % Pt sample. A comparison of the ORR activities of the 75 wt. % Co_{100} + 25 wt. % Pt and 75 wt. % $Pd_{20}Co_{80}$ + 25 wt. % Pt samples illustrates the synergistic effect of the addition of a small amount of Pd to the Pt-Co alloy system. Additionally, similar to the results obtained for the as-synthesized samples, the activity for ORR does not change appreciably on increasing the Pt content while keeping the Pd : Co ratio constant at 4: 1. However, unlike the as-synthesized samples, the origin of similar activities can be traced to the phase structure of the samples. As the 50 wt. % $Pd_{80}Co_{20}$ + 50 wt. % Pt sample consists of two phases having compositions similar to 75 wt. % $Pd_{80}Co_{20}$ + 25 wt. % Pt and 25 wt. % $Pd_{80}Co_{20}$ + 75 wt. % Pt, the activity for ORR is probably a mass based average of the activities of both the phases.

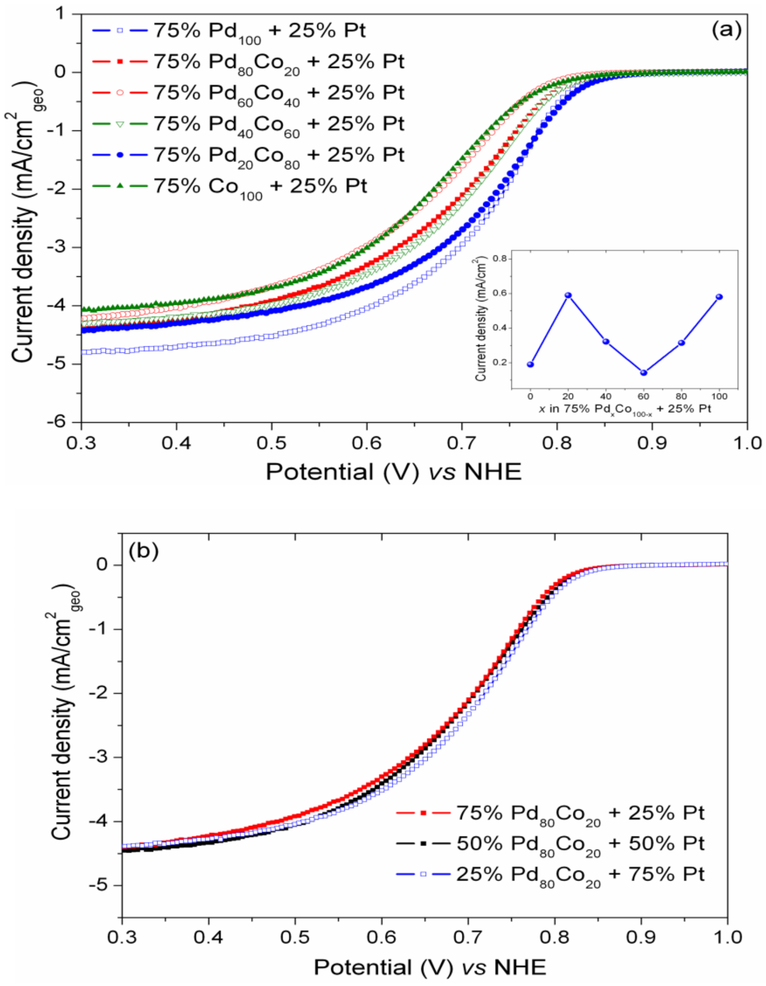

Figure 4.18. (a) Hydrodynamic polarization curves of the (100-y) wt. % Pd_xCo_{100-x} + y wt. % Pt samples after heat treatment at 900 °C, with the inset showing the variation of kinetic current density at 0.8 V *vs* NHE with Pd content and (b) hydrodynamic polarization curves of the 75 wt. % $Pd_{80}Co_{20}$ + 25 wt. % Pt, 50 wt. % $Pd_{80}Co_{20}$ + 50 wt. % Pt, and 25 wt. % $Pd_{80}Co_{20}$ + 75 wt. % Pt samples after heat treatment at 900 °C. The % values in the legend refer to wt. %.

Figure 4.19 compares the performance in single cell proton exchange membrane fuel cell (PEMFC) at 60 °C of commercial Pt, as-synthesized 75% $Pd_{80}Co_{20}$ + 25% Pt, and Pt synthesized by the MW-ST method. Although the performance of 75% $Pd_{80}Co_{20}$ + 25% Pt is lower than that of commercial Pt, it is higher than the Pt sample synthesized by the same method and having similar particle size. The single cell data are consistent with the RDE data presented earlier. The electrochemical data thus demonstrate that encapsulating the Pd_xCo_{100-x} nanoalloys within Pt offers an attractive approach to lower the Pt loading and overall catalyst cost, while the Pd-Co core may have an important influence in enhancing the activity of the outer Pt layer.

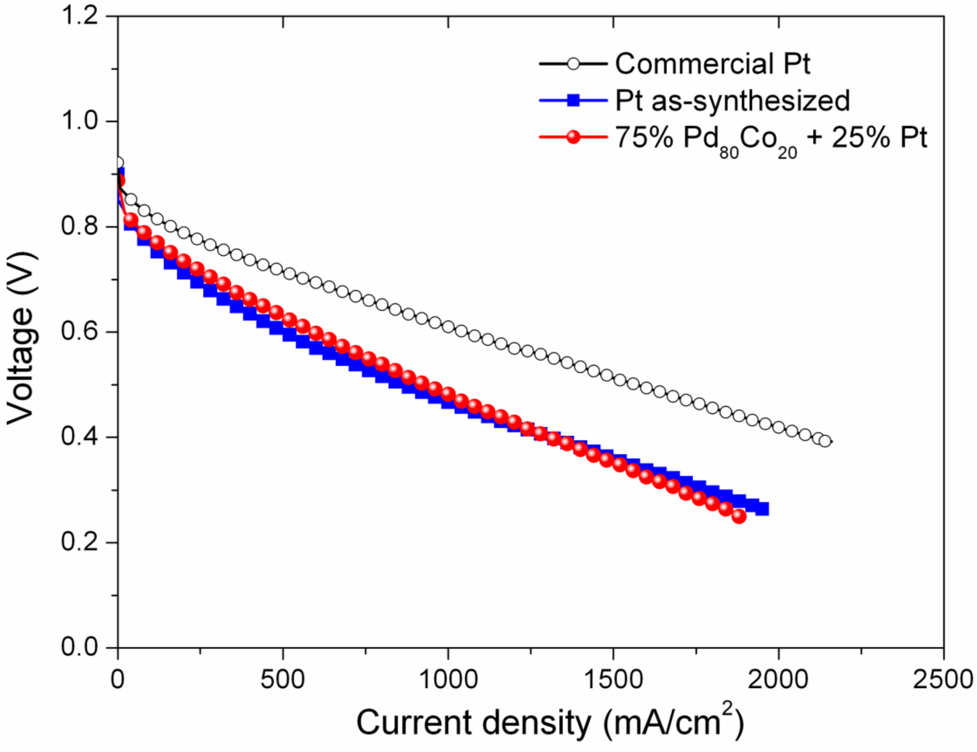

Figure 4.19. Comparison of the ORR activities at 60 °C of the commercial Pt, as-synthesized Pt, and as-synthesized 75 wt. % $Pd_{80}Co_{20}$ + 25 wt. % Pt samples in single cell proton exchange membrane fuel cell. The % values in the legend refer to wt. %.

4.4 CONCLUSIONS

A rapid MW-ST synthesis process taking advantages of both the microwave and solvothermal effects has been pursued to obtain a seed-mediated growth of multimetallic Pt-Pd-Co nanoalloy electrocatalysts with a high degree of alloying and controlled particle size within a short reaction time (15 min) at $< 300\ ^oC$ without any post annealing in reducing gas atmospheres. The multimetallic alloy compositions synthesized by the MW-ST method show much higher activity for ORR compared to their counterparts synthesized by the conventional borohydride reduction method. Particularly, the ternary electrocatalyst $Pt_{70}Pd_{20}Co_{10}$ synthesized by the MW-ST method shows ORR activity comparable to that of commercial Pt while lowering the cost significantly. Due to an added advantage of the high tolerance of Pd-containing alloy catalysts to methanol, the activity of $Pt_{50}Pd_{30}Co_{20}$ for ORR in DMFC is superior to that of commercial Pt at higher methanol concentrations. Moreover, possible "surface strain effects" developed on the outermost Pt and Pd atomic layers due to the low concentration of Co on the surface compared to that in the alloy core as facilitated by the pressure effects under the MW-ST conditions may play a role in enhancing the catalytic activity.

Additionally, a rapid two-step MW-ST synthesis has been pursued to obtain carbon-supported Pt-encapsulated Pd-Co nanoparticles with high crystallinity and controlled particle size. A detailed analysis by XRD, TEM, and XPS of the as-synthesized samples confirm the presence of Pt overlayers on the surface of Pd-Co nanoparticles. RDE experiments show that the 75% $Pd_{80}Co_{20}$ + 25% Pt sample with a Pt loading of 5 wt % exhibits higher catalytic activity for ORR compared to either $Pd_{80}Co_{20}$ or Pt synthesized by the same method (all having the same total metal loading of 20 wt. %), demonstrating the influence of Pd-Co core on the outermost Pt layer in enhancing the catalytic activity. Single cell PEMFC data confirm the RDE data and affirm the enhancement in catalytic activity per unit mass of Pt on encapsulating Pd-Co by Pt. The activity for ORR, however, decreases on heat treating at 900 ^{o}C due to the changes in phase compositions and particle growth. The study demonstrates that encapsulation of lower cost metals or alloys with Pt by novel synthesis approaches such as the MW-ST method presented here represents an attractive strategy to lower the Pt loading and catalyst cost without sacrificing the catalytic activity.

Chapter 5: Galvanic Displacement of Cu by Pt and Pd ions and its Application as Electrocatalyst

5.1 INTRODUCTION

Recently, a novel class of electrocatalyst has been developed by selective voltammetric dealloying of Cu from Pt-Cu alloys [51,52,73, 167,168]. The dealloying of Cu from the carbon-supported Pt-Cu alloy electrocatalyst was carried out by subjecting the Pt-Cu alloy to potential cycling repeatedly to dissolve the less noble Cu from the catalyst surface. Moreover, it had been postulated that dissolution of Cu from Pt-Cu alloy at high potential leads to a “core-shell” structure consisting of a Pt-Cu alloy core encapsulated by a Pt shell. The enhancement in activity for ORR has been attributed to geometric effects where a favorable Pt-Pt bond distance facilitates the electro-reduction of oxygen. This Chapter presents synthesis and characterization of a series of Pt@Cu “core-shell” nanoparticles with a Cu or Pt-Cu core and Pt shell supported on carbon by a galvanic displacement reaction between Pt^{4+} and Cu to achieve a structure similar to that obtained by voltammetric dealloying. Additionally, Pt-Pd@Cu “core-shell” nanoparticles having Pt and Pd shells with a Cu core have been synthesized and characterized for their activity towards ORR.

Galvanic displacement reactions have been extensively used for the synthesis of noble metal core-shell nanoparticles, nanocubes, nanocages, and tetrahedrons using silver nanoparticles as sacrificial template [169-173]. Recently, hollow Pt spheres synthesized by galvanic displacement of Ag by Pt^{4+} have been found to offer enhanced activity for oxygen reduction reaction [174]. However, because of the tendency of copper to form oxides in neutral or basic media, there are very few reports on the galvanic displacement of Cu by noble metals and formation of core-shell nanoparticles [175]. Nevertheless, Pt@Cu "core-shell" nanoparticles synthesized by sequential polyol reduction of Cu and Pt have shown greater selectivity and activity for NO_x reduction and galvanic displacement of electrochemically deposited Cu by Pt has been reported [176,177]. Also, metallic Cu has been used to reduce Au and Pt in dendrimer templates and explored as CO oxidation catalysts [175]. However, the synthesis and characterization of Pt@Cu core shell nanoparticles in aqueous media by galvanic displacement reaction between Pt^{4+} and Cu and its application as cathode electrocatalysts in a fuel cell are yet to be studied.

The characterization of the Pt@Cu core shell samples by XRD, EDS analysis in a SEM, TEM, CV, hydrodynamic polarization measurements for ORR in RDE, and single cell PEMFC measurements is presented in this Chapter.

5.2 EXPERIMENTAL

5.2.1 Synthesis of Cu nanoparticles, Pt@Cu "core-shell" nanoparticles, and Pt_xPd_{1-x}@Cu nanoparticles

The synthesis of Cu nanoparticles was achieved by a reduction of $CuSO_4.H_2O$ with $NaBH_4$ in buffered aqueous media at room temperature. Briefly, 250 mL of buffer solution with pH = 3.0 – 6.0 and a buffer strength of 0.2 M was prepared by adding required amounts of sodium citrate and citric acid in de-ionized water. The concentrations of citric acid and sodium citrate were evaluated using the Henderson–Hasselbalch equation and the pK_a values for citric acid (3.13, 4.76 and 6.40) [178]. The pH of the buffer was measured using a Corning 315 pH meter and was found to be within ± 0.05 of the intended pH value. To determine the precise pH condition for the reduction of Cu and formation of Cu nanoparticles, 200 mg of $CuSO_4.5H_2O$ was dissolved in 250 mL of the buffer solution of various pH (3.0 – 6.0) and purged with N_2 gas for 30 minutes. 500 mg of $NaBH_4$ dissolved in 50 mL of water was then added drop wise and the reaction was continued for 2 h under constant stirring and nitrogen purging to reduce the Cu^{2+} ions to Cu. The reaction mixture was then centrifuged, the clear colorless supernatant liquid was discarded, and the precipitate was collected. Based on the XRD data of the precipitate, the optimum pH condition to obtain Cu was determined to be 3.0. Additionally, a sample was prepared in a manner as described above, but without pH control, for a comparison.

For the synthesis of Pt@Cu "core-shell" nanoparticles, 250 mL of buffer solution with a pH of 3 and buffer strength of 0.2 M was prepared by the method described earlier. Subsequently, 160 mg of Vulcan carbon and required amount of $CuSO_4.5H_2O$ was added into the buffer solution to give x wt. % Cu in carbon ($20 \leq x \leq 140$). The solution was then purged with N_2 gas for 0.5 h under constant stirring, 500 mg of $NaBH_4$ dissolved in 50 mL of water was added drop wise, and the reaction was conducted for 4 h under continuous stirring and N_2 purging to reduce the Cu^{2+} ions to Cu. After the 4 h of reaction, 106.2 mg of $H_2PtCl_6.6H_2O$ (corresponding to 40 mg Pt metal on 160 mg carbon or 20 wt. % Pt on 80 wt. % C) dissolved in 50 mL of water was added drop wise, and the galvanic displacement reaction was conducted for 2 h. The carbon supported Pt@Cu electrocatalysts thus obtained were filtered and washed repeatedly with de-ionized water. The powder was dried overnight in a convection oven at 80 ^{o}C. 100 mg of the powder thus obtained was digested in 50 mL of 9 M H_2SO_4 for 3 h to remove any unreacted copper on the surface. Finally, the mixture was filtered and washed repeatedly with de-ionized water. The electrocatalysts thus obtained with x wt. % of Cu in carbon are hereafter designated as Pt@Cu x%. To make it clear, all the Pt@Cu x% samples had 20 wt. % Pt in 80 wt. % C while considering only Pt and C, but additionally had varying amounts of Cu. In other words, the total metal (Pt + Cu) loading in the samples is higher than 20 wt. % and the total carbon content is accordingly lower than 80 wt. % depending on the Cu content in the final product.

To obtain an encapsulation of Pt_xPd_{1-x} ($0 \leq x \leq 100$) on Cu, 110% Cu (*i.e.* 176 mg Cu on 160 mg carbon) in carbon was synthesized by the same method as described earlier. Required amounts of $H_2PtCl_6.6H_20$ and Na_2PdCl_4 were then dissolved in 50 mL of water and added drop wise. The total weight of Pt and Pd was kept constant at 20 wt. % on 80 wt. % Vulcan carbon (40 mg of Pt + Pd on 160 mg carbon). After 2 h of reaction, the mixture was filtered and washed repeatedly with water. The samples were finally digested in 50 mL of 9 M H_2SO_4 for 3 h to remove any unreacted copper on the surface as in the case of Pt@Cu.

The samples were all characterized by XRD with Cu Kα radiation. XRD patterns were recorded with a counting time of 12 s per 0.02° between 30 and 90°. All the XRD patterns were fitted by a mix of Gaussian and Lorentzian profiles (50% Gaussian) after background subtraction using the Jade MDI software. For most of the samples, the lattice parameter values were evaluated using the first three reflections between $2\theta = 30^{o}$ and 85^{o}. The Pt : Cu ratio in the Pt@Cu x% system and Pt : Pd ratio in the Pt_xPd_{1-x}@110% Cu system were assessed by averaging the ratios obtained at four different spots in the EDS analysis with a JEOL-JSM5610 SEM having an Oxford instruments EDS attachment. Morphological and particle distribution studies were carried out with a JEOL 2010F high-resolution TEM operated at 200 keV.

The CV experiments were conducted in N_2 purged 0.5 M H_2SO_4 (solutions prepared from Fisher Scientific high purity Optima grade 18 M H_2SO_4) at a scan rate of 50 mV/s between 0.0 and 1.0 V (*vs* NHE) at ambient conditions and the catalyst coated glassy carbon electrode was prepared in the same way as discussed in section 4.2.3. The stable voltammograms obtained after the initial cycling are reported here. Thereafter, the

RDE experiments were conducted with a glassy carbon disk electrode (5 mm dia.) mounted onto an interchangeable RDE holder (Pine Instruments, USA) in O_2 saturated 0.5 M H_2SO_4.The potential was scanned from 0.0 to 1.0 V (*vs* NHE) at 5 mV/s.

For fuel cell tests, the catalyst ink was prepared as mentioned in section 4.2.3. The catalyst loading was kept at 0.4 mg/cm^2 both for the anode and the cathode in PEMFC. The fuel cell was run at 60 ^{o}C.

5.3 RESULTS AND DISCUSSIONS

5. 3.1 Pt@Cu system

The propensity of Cu to oxidation (both bulk and surface) is a significant barrier to the synthesis of Cu nanoparticles and subsequent galvanic displacement by Pt^{4+}. Although Cu/Cu^{2+} redox couple (E^0= + 0.340V *vs* NHE) is placed positive to the H_2/H^+ redox couple in the electrochemical series and copper inherits some nobility of its group (IB of the periodic table), Cu nanoparticles formed by a reduction of Cu^{2+} are susceptible to oxidation due to the alkalinity of the $NaBH_4$ solution. As evident from the XRD patterns shown in Fig. 5.1(a), by decreasing the pH to 3.0, it was possible to obtain phase-pure metallic Cu without any bulk oxide impurity. In addition, capping of Cu nanoparticles by citrate ions inhibit the particle growth as apparent from the broadening of the (111) reflection in all the Cu samples prepared in the buffered solution compared to the samples synthesized without any buffer.

After the synthesis of the Cu nanoparticles supported on Vulcan carbon, the second step involved galvanic displacement of Cu by Pt^{4+} according to the reaction $2Cu + [PtCl_6]^{2-} \rightarrow Pt + 2Cu^{2+} + 6Cl^-$. The difference between the E^o values of $Pt/[PtCl_6]^{2-}$ (0.742 V *vs* NHE) and Cu/Cu^{2+} (0.340 V *vs* NHE [178]) is adequate for the displacement reaction to be both thermodynamically as well as kinetically favorable. However, the stoichiometry of the reaction and the difference in the atomic radius values of Cu and Pt (r_{Cu} = 1.28 Å and r_{Pt} = 1.39 Å) suggest that displacement of Cu atoms on the outermost layer by Pt^{4+} would cause only a fraction of the top layer of the nanoparticles to be covered by Pt atoms, thus leaving the inner layers for further reaction. This would result in a formation of large number of steps and kinks on the outermost shell of Pt@Cu nanoparticles. Additionally, as the reaction proceeds, a concentration gradient of Pt is likely to develop with pure Pt on the outermost shell, pure Cu on the core, and a Pt-Cu alloy of varying composition sandwiched between pure Pt and pure Cu. It is also likely that both the displacement reaction and the nucleation and growth of Pt layers would initiate on low coordination sites of the Cu nanoparticles. Also, the Pt atoms resulting from the galvanic displacement reaction would be non-epitaxial because of the large difference between the atomic radii and lattice parameter values of Cu and Pt. [170].

With an increase in initial Cu content, keeping the reaction conditions the same, both the dispersion (number density of Cu nanoparticles) as well as the particle size are expected to increase. This would influence the surface sensitive displacement reaction as increase in dispersion would increase the surface area of the Cu nanoparticles while increase in particle size would decrease the surface area. In addition, as the number of Pt atoms participating in the reaction is kept constant, an increase in both particle size and dispersion would influence the Pt-Cu alloy composition sandwiched between the Cu core and the Pt shell. Especially, an increase in particle size would increase the concentration of Cu in the Pt-Cu layer.

Figure 5.1(b) presents the XRD patterns of Pt@Cu x% samples after the acid treatment. Interestingly, all the samples show evidence of an alloyed Pt-Cu structure instead of either pure Pt or Cu structure as apparent from the large shift in the (111) reflection towards higher angle compared to the(111) reflection of pure Pt. Indeed, evaluation of the lattice parameter values for all the samples (except the Pt@Cu 20% and Pt@Cu 40% samples as the XRD patterns of these samples were too diffused to be amenable for analysis) as shown in Table 5.1 and Fig. 5.2 suggest alloying between Pt and Cu or a substitution of smaller Cu for larger Pt. Moreover, the Cu : Pt atom ratio in the "core-shell" nanoparticles as determined from the SEM-EDS analysis and the lattice parameter values using Vegard's law (Table 1) agree closely with each other for samples with low initial nominal copper contents (< 80 wt. % as in Pt@Cu 60% and Pt@Cu 80%). This suggests that the Cu core is very small and the nanoparticles are composed of mostly Pt-Cu alloy core with Pt shells in these low Cu content samples. In contrast, with a further increase in initial nominal Cu content (Pt@Cu 100 % or higher), the Cu contents obtained from the lattice parameter values are significantly higher than those obtained from the SEM-EDS analysis. This suggests a higher Cu content in the Pt-Cu alloy formed below the Pt shell. For samples with higher initial nominal Cu content, the number of Pt atoms may not be sufficient to displace all the surface Cu atoms and significant number of Cu particles may not form a "core-shell" structure. As a result, the unreacted Cu may get leached out during the acid treatment with 9 M H_2SO_4, and the Cu content obtained from SEM-EDS analysis becomes nearly constant for samples with higher initial nominal Cu contents as seen in Table 5.1 and Fig. 5.2.

Table 5.1. Lattice parameters and composition analysis of the Pt@Cu x% ($20 \leq x \leq 140$) samples.

Catalyst[a]	Lattice parameter (Å)	Cu : Pt atom ratio from SEM-EDS	Cu : Pt atom ratio from lattice parameter values[b]
Pt@Cu 20%	-	3.3 : 96.7	
Pt@Cu 40%	-	6.5 : 93.5	
Pt@Cu 60%	3.887	10.5 : 89.5	11.6 : 88.4
Pt@Cu 80%	3.884	11.2 : 88.8	12.6 : 87.4
Pt@Cu 100%	3.834	19.2 : 80.8	29.0 : 71.0
Pt@Cu 110%	3.815	24.2 : 75.8	35.1 : 64.9
Pt@Cu 120%	3.801	24.9 : 75.1	39.5 : 60.5
Pt@Cu 140%	3.802	24.1 : 75.9	39.4 : 60.6

[a] The % values refer to wt. % Cu in carbon in the initial reaction (see experimental section)

[b] determined using Vegards's law (x) [$a_{alloy} = x a_{Cu} + (1-x) a_{Pt}$]

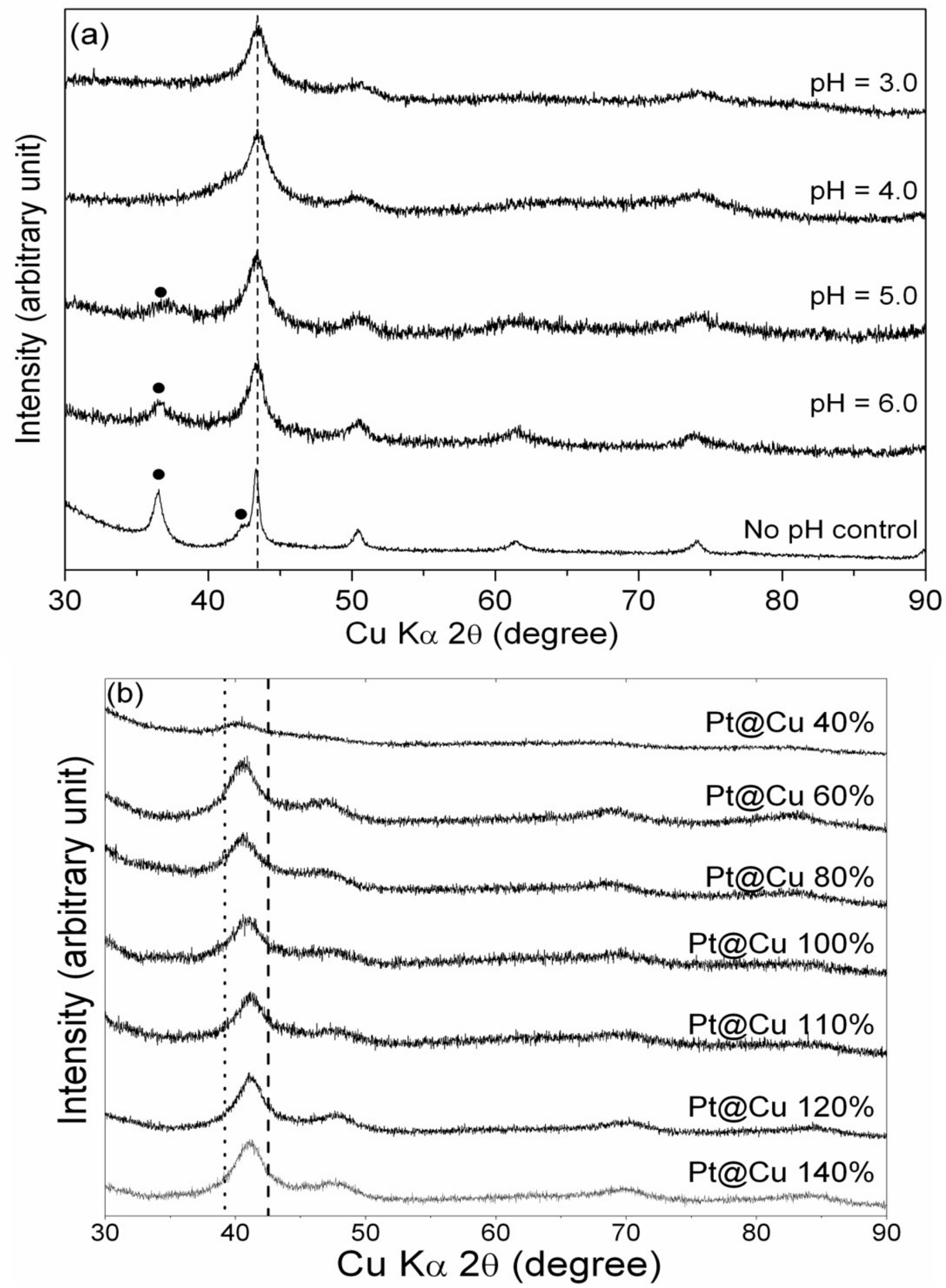

Figure 5.1. XRD patterns of (a) the Cu nanoparticles prepared at various pH values and without pH control and (b) the Pt@Cu x% ($40 \leq x \leq 140$) samples. The dashed line (---) and the dotted line (…) refer, respectively, to the expected positions of Cu (111) and Pt (111). The reflections marked with ● refer to Cu_2O.

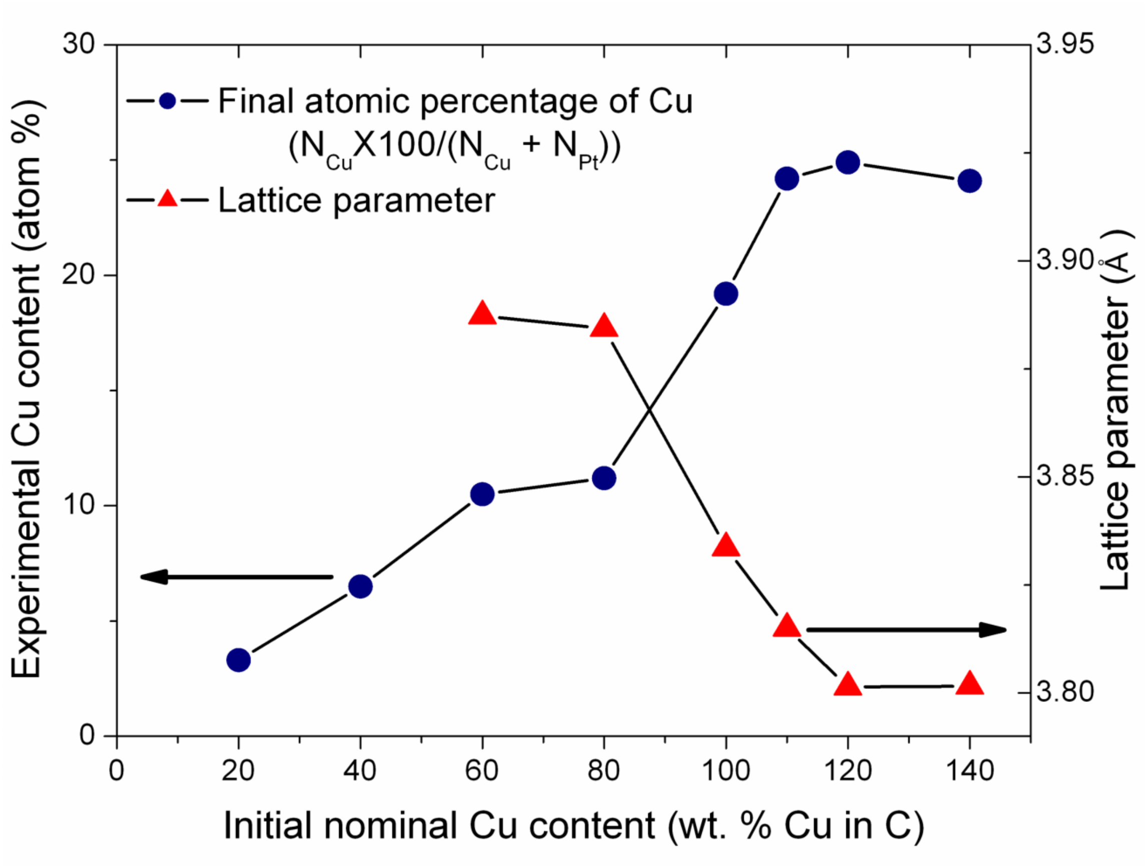

Figure 5.2. Variations of the (a) experimental Cu atom % as obtained from the SEM-EDS analysis (from Table 1) and (b) lattice parameter values with initial nominal wt. % Cu. The data were obtained after treating the Pt@Cu x% samples with 9 M H_2SO_4 to leach out the unreacted Cu.

Figures 5.3(a) and (b) present the particle size and distribution for the Pt@Cu 20% and Pt@Cu 110% samples after treatment with 9 M H_2SO_4 as characterized by the TEM measurements. As can be observed, the nanoparticles of Pt@Cu 20% have a mean particle diameter of 1.9 ± 0.4 nm with a narrow particle size distribution without much agglomeration. An increase in initial nominal Cu content resulted in significantly larger particle size as evident from the particle size distribution of the Pt@Cu 110% sample having a mean particle diameter of 7.3 ± 1.9 nm. Additionally, the high resolution TEM as shown in the insert of Figure 5.3(a) demonstrates the well crystalline nature of the nanoparticles. Surprisingly, we did not observe any hollow spheres or nanoshells even after acid treatment, which indicates that the Cu core is fully protected by Pt shells.

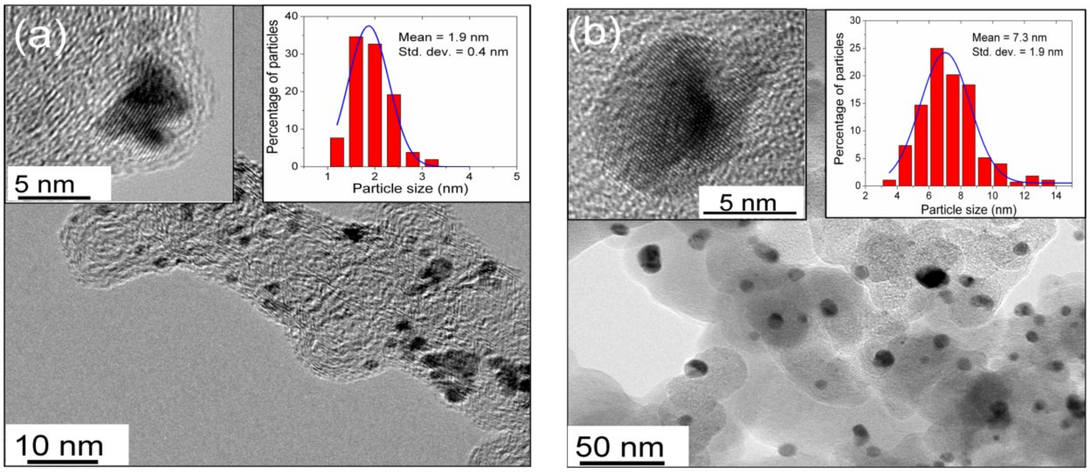

Figure 5.3. TEM images of the (a) Pt@Cu 20% and (b) Pt@Cu 110% samples. The insets show the particle size distribution and HR-TEM images.

Figure 5.4 presents the cyclic voltametry profiles of selected Pt@Cu samples in N_2 purged 0.5 M H_2SO_4 after treatment with 50 mL of 9 M H_2SO_4. The voltammograms resemble that of polycrystalline Pt, which suggests that the surface of the nanoparticles is composed of Pt atoms only. Moreover, we did not observe any anodic currents due to the dissolution of Cu from the lattice upon cycling. This confirms the core shell structure of the nanoparticles having Cu atoms in the core and Pt atoms forming the shell.

However, significant differences particularly in the hydrogen region of the CV could be noticed. The voltammetric profiles of polycrystalline platinum nanoparticles in

0.5 M H_2SO_4 contains contributions from all the surface planes, terraces, steps, and kinks that are present on the surface. Each of these features give a characteristic signal due to both hydrogen and anion (bisulphate ion as in 0.5 M H_2SO_4) adsorption [179-181]. The hydrogen desorption region of the voltammetric profile of polycrystalline Pt nanoparticles as shown in the Fig. 5.4 shows peaks located around 0.1 V *vs* NHE (can be associated with Pt(110) planes) and 0.17 V (probably due to step sites) and a broad shoulder at 0.21 V superimposed on a featureless Pt(111) signal [180,181]. Similar features were obtained for the Pt@Cu 20%, Pt @Cu 40%, and Pt@Cu 60% samples as well although the signals were weaker. However, at high initial nominal contents of Cu (80% and above), the peak occurring at 0.1 V diminished significantly and a broad featureless shoulder region developed between 0.1 and 0.2 V. This suggests the presence of high number of stepped surfaces and kink sites. This is not unexpected, considering the synthesis scheme we adopted for the preparation of the Pt@Cu "core-shell" particles. As mentioned earlier, the stoichiometry of the displacement reaction dictates the release of 2 Cu atoms per Pt^{4+} ion as Cu atoms are oxidized to Cu^{2+} and Pt^{4+} ions are reduced to Pt. Although Pt atoms are larger than Cu atoms, displacement of 2 Cu atoms by one Pt atom would expose inner Cu layers beneath the surface Cu layer, which can undergo further displacement reaction leading to a large number of kinks and steps. Nonetheless, the electrochemical active surface area (ESA) can be estimated from the total charge due to hydrogen desorption ($Q_{H\text{-}des}$). Table 5.2 gives the electrochemical active surface area (ESA) evaluated after subtracting the contribution due to the double layer capacitance and assuming a conversion factor of 210 $\mu C/cm^2$.

Interestingly, the onset potential for the formation of Pt-hydroxide ($Pt + H_2O \rightarrow Pt\text{-}OH + H^+ + e^-$) during the anodic sweep was shifted by as much as 50 mV for all the Pt@Cu samples compared to commercial Pt. A delayed formation of Pt-OH has been frequently observed for Pt alloys and it has been considered a major reason for the enhanced electrocatalytic activity for ORR [43-46, 50, 51, 58, 182, 183]. Although the electrocatalysts synthesized here at room temperature may not be perfectly alloyed, the delayed onset potential for Pt-OH formation signifies electronic modification of Pt surface layer by the inner Pt-Cu core. For quantification purposes, the total charge ($Q_{OH}^{0.85\ V}$) due to Pt-OH formation was determined by integrating the CV profiles for all the samples from 0.6 to 0.85 V vs NHE after correcting for the background and normalizing with respect to the scan rate. The coverage due to Pt-OH (θ_{OH}) was then evaluated by dividing the total charge due to Pt-OH formation by the charge due to hydrogen desorption ($\theta_{OH} = Q_{OH}^{0.85V} / Q_{H\text{-}des}$). Table 5.2 gives the values thus obtained for all the samples. As seen in Table 5.2, the coverage θ_{OH} is significantly lower for all the Pt@Cu samples compared to commercial Pt although no specific trend could be observed.

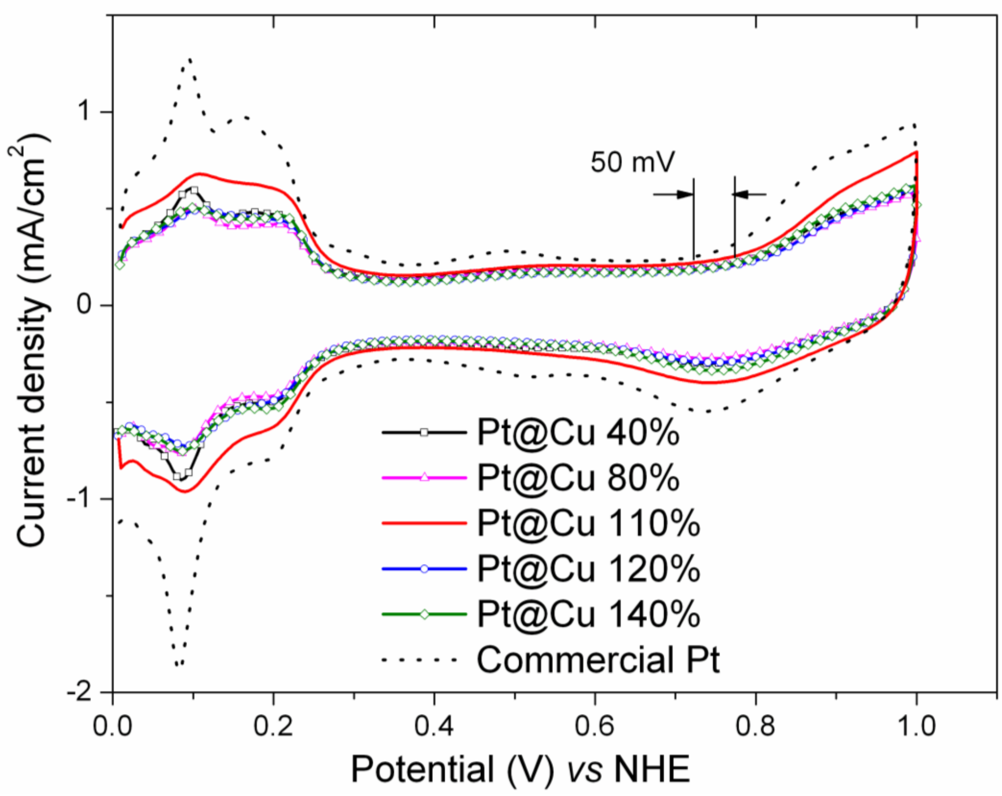

Figure 5.4. Cyclic voltammogramms of selected Pt@Cu samples obtained in N_2 saturated 0.5 M H_2SO_4 at room temperature with a scan rate of 50 mV/s.

Table 5.2. Electrochemical active surface area (ESA) and the coverage by OH_{ads} (θ_{OH}) determined from CV.

Catalyst	Electrochemical active surface area (ESA) (m^2/gm)	Coverage by OH_{ads} due to Pt-OH formation (θ_{OH}) upto 0.85 V *vs* NHE
Commercial Pt (Alpha Aesar HiSpec 3000)	78.03	0.1066
Pt@Cu 20%	33.34	0.1240
Pt@Cu 40%	38.82	0.0686
Pt@Cu 60%	34.76	0.0768
Pt@Cu 80%	34.52	0.0768
Pt@Cu 100%	46.45	0.0641
Pt@Cu 110%	54.11	0.0635
Pt@Cu 120%	37.05	0.0611
Pt@Cu 140%	40.16	0.0658

The catalytic activity of the Pt@Cu electrocatalysts for ORR was evaluated by linear sweep voltammetric measurements at 5 mV/s in O_2 saturated 0.5 M H_2SO_4 electrolyte using a rotating disk electrode (RDE) at 1600 rpm, and the data are compared with that of commercial Pt (Alfa Aesar Hispec 3000) in Fig. 5.5. As seen in Fig. 5.5(a), a clear limiting current of 5.0 ± 0.25 mA/cm^2 is obtained for all the samples. Additionally, the characteristic polarization curves shift towards low over-potential with increasing Cu content, indicating an increase in activity for ORR. Interestingly, the samples with initial nominal Cu content higher that 80% (Pt@Cu 100%, Pt@Cu 110%, Pt@Cu 120%, and Pt@Cu 140%) show significantly higher activities than commercial

Pt. Indeed, the mass transfer corrected Tafel plots as shown in the inset of Fig. 5.5(a) and the variation of the kinetic current density at 0.85 V *vs* NHE with initial nominal Cu content as shown in Fig. 5.5(b) clearly demonstrate a "volcano" type plot for the ORR activity vs initial nominal Cu content. The sample Pt@Cu 110% (with an initial Cu content of 110 wt. % in carbon) shows the maximum activity for ORR, which is almost 1.8 times higher than that of commercial Pt at 0.85V *vs* NHE. However, further increase in initial nominal Cu content results in a decrease in the ORR activity.

While it is possible to increase the ORR activity by increasing the dispersion and by extensive surface roughening that increases the surface area and introduces kinks and steps, we believe the observed increase in the ORR activity of the "core-shell" Pt@Cu samples is partly due to the electronic modification of the Pt shell by the Pt-Cu core. Figure 5.5(c), which shows the electrochemical surface area specific activity for ORR (kinetic current density at 0.85 V divided by electrochemical active surface area), clearly demonstrates a linear increase in activity with increasing initial nominal Cu content. As discussed earlier, an increase in the Cu content essentially increases the dispersion and causes an increase in the Cu concentration in the Pt-Cu alloy (sandwiched between the Cu core and the Pt shell) in the "core-shell" nanoparticles. However, the electrochemical surface area measurements (Table 5.2) as well as the surface area specific activity (Fig. 5.5(c)) clearly demonstrate that the increase in activity for ORR is not purely due to surface roughening effects or increase in dispersion. Consequently, the enhancement is due to the electronic effects.

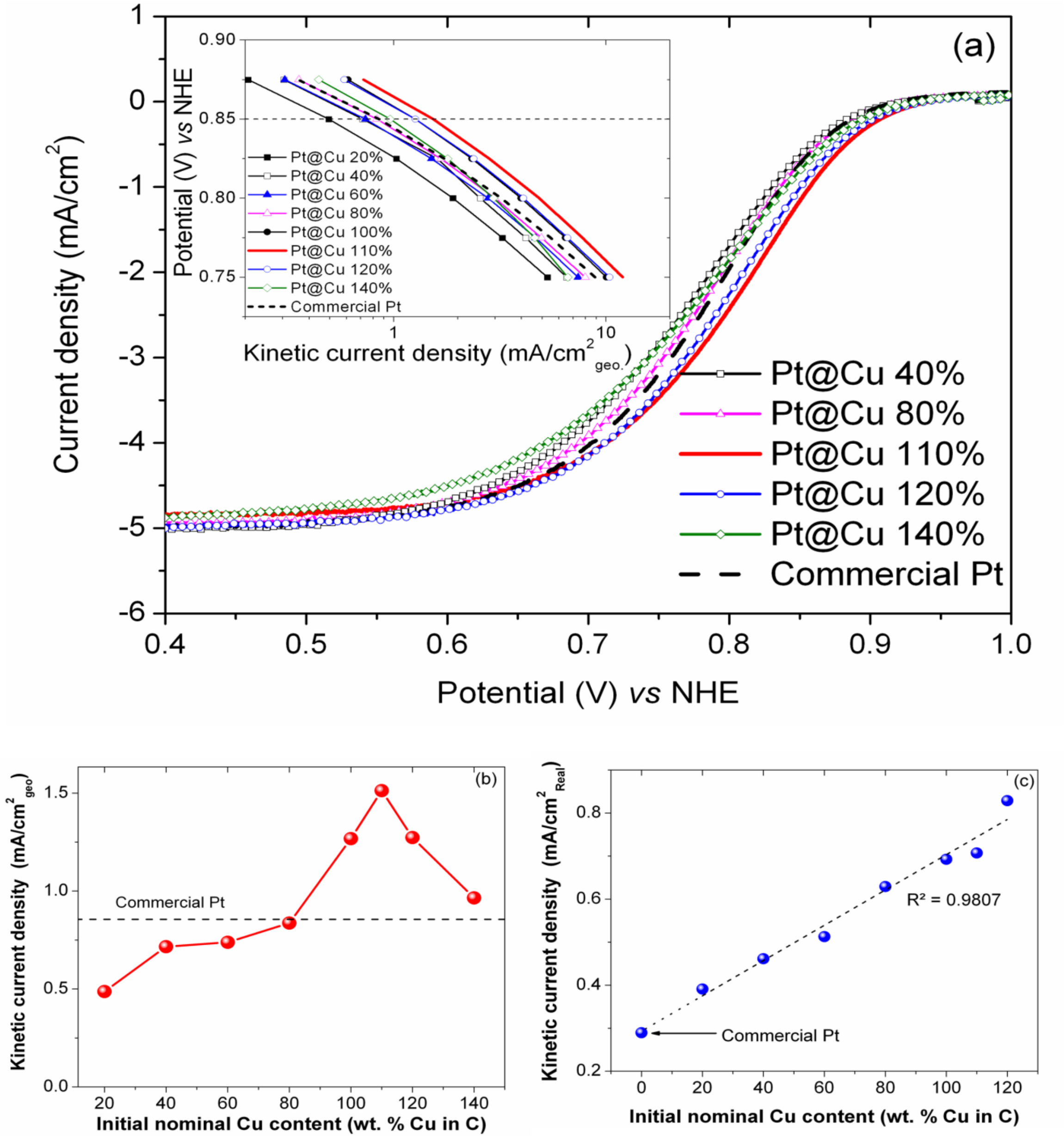

Figure 5.5. (a) Hydrodynamic polarization curves of selected Pt@Cu samples and commercial Pt in O_2 saturated 0.5 M H_2SO_4 at room temperature and 1600 rpm, with the insert showing the mass transfer corrected Tafel plots for Pt@Cu x% ($20 \leq x \leq 140$), (b) variation of the kinetic current density at 0.85 V *vs* NHE (obtained from Tafel plots) with initial nominal Cu content, and (c) variation of the surface area specific current density at 0.85 V *vs* NHE with initial nominal Cu content.

The delay in onset potential for the formation of Pt-OH as mentioned earlier also points to intrinsic enhancements. The strains introduced in the outer shell caused by an inner core with smaller lattice parameter may also influence the electrocatalytic activity by changing the Pt-Pt nearest neighbor distance and might be one of the possible reasons for the enhanced activity of Pt@Cu "core-shell" nanoparticles. Nevertheless, the strains introduced by galvanic displacement will be significantly less compared to voltammetric dealloying of a Pt-Cu alloy.

In order to investigate the catalytic activity of the Pt@Cu "core-shell" nanoparticles in acidic solid Nafion electrolytes, the catalysts were also tested in single cell proton exchange fuel cell (PEMFC). Figure 5.6 compares the performances of commercial Pt and Pt@Cu 110% at 60 ^{o}C in a single cell PEMFC. Similar to the RDE experimental results obtained in 0.5M H_2SO_4, the performance of Pt@Cu 110% is found to be higher than that of commercial Pt.

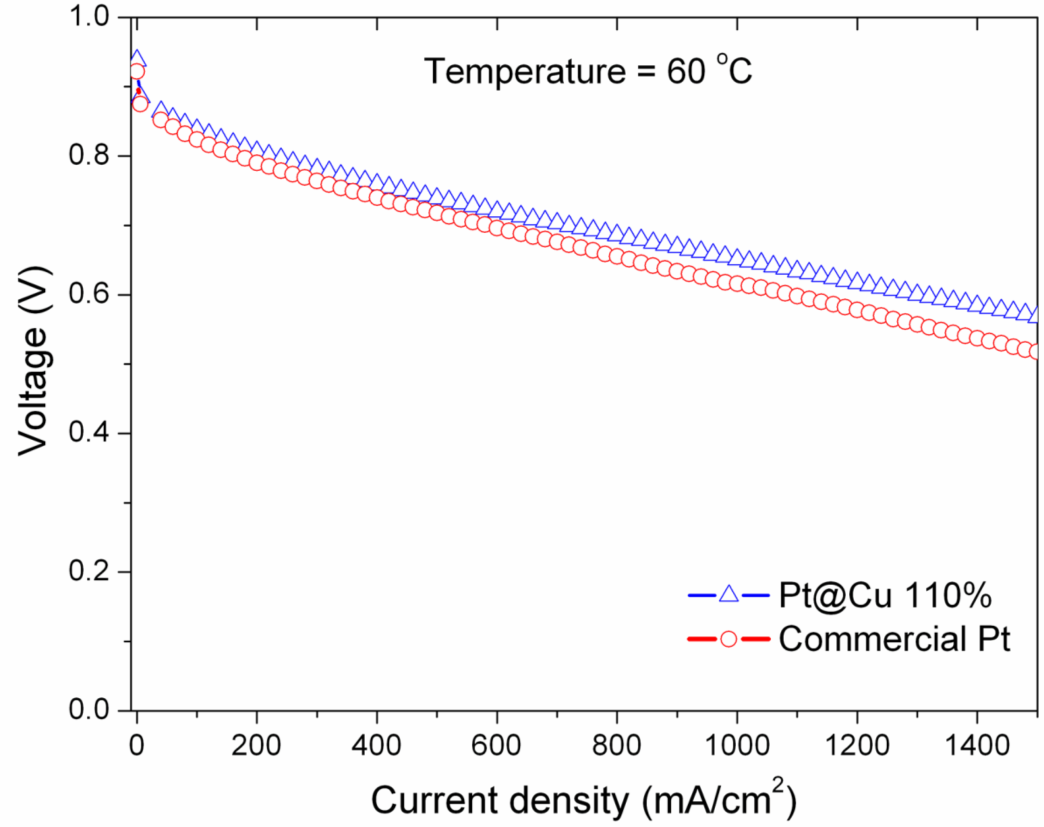

Figure 5.6. Comparison of the ORR activities of the commercial Pt and Pt@Cu 110% at 60 °C in a single cell proton exchange membrane fuel cell.

5.2.2 Pt_xPd_{1-x}@Cu 110% ($0 \le x \le 100$) system

Figure 5.7 shows the XRD patterns of the Pt_xPd_{1-x}@Cu 110% sample after the acid treatment. Although the lattice parameter values could not be evaluated because of the diffused nature of the XRD patterns, it can be observed that there is a systematic shift in the (111) reflection to lower 2θ angles with increasing palladium content. This suggests a displacement of Cu atoms by Pd^{2+} ions as well along with Pt^{4+} ions. Also, subsequent acid treatment causes significantly more copper to be leeched out and the final copper content decreases with increase in palladium content. Interestingly, unlike Pt@Cu 110%, which showed a large shift of the reflections towards higher angles (Fig. 5.1), Pd@Cu110% shows no shift. The peak positions correspond to those of pure Pd having a lattice parameter of 3.891 Å (a_{Pd} = 3.8902 Å). This suggests that the nanoparticles of Pd@Cu 110% contain negligible amount of copper in the core, which is consistent with the EDS analysis data (Table 5.3). Surprisingly, the Cu content in the "core-shell" nanoparticles decreases with increasing Pd concent although the stoichiometry of the displacement reaction dictates the release of only one Cu atom per Pd^{2+} as Cu is oxidized to Cu^{2+} and Pd^{2+} is reduced to Pd unlike the reaction between Cu and Pt^{4+}. Thus, it can be expected that the concentration of Cu in the nanoparticles of Pd@Cu 110% will be substantially more than that of Pt@Cu 110%. The reasons for this anomalous behavior are not clear, but this might be a consequence of the post synthesis acid treatment or the reaction dynamics.

Table 5.3. Composition analysis of the Pt_xPd_{1-x}@Cu 110% ($0 \leq x \leq 100$) samples by SEM-EDS

Catalyst	Atomic percentages of Cu, Pd, and Pt		
	Cu	Pd	Pt
Pd@Cu 110%	4.8	95.2	-
$Pt_{20}Pd_{80}$@Cu 110%	-	74.6	25.4
$Pt_{40}Pd_{60}$@Cu 110%	8.7	53.1	38.2
$Pt_{60}Pd_{40}$@Cu 110%	15.5	32.7	51.8
$Pt_{80}Pd_{20}$@Cu 110%	24.7	21.6	53.7
Pt@Cu 110%	24.2	-	75.8

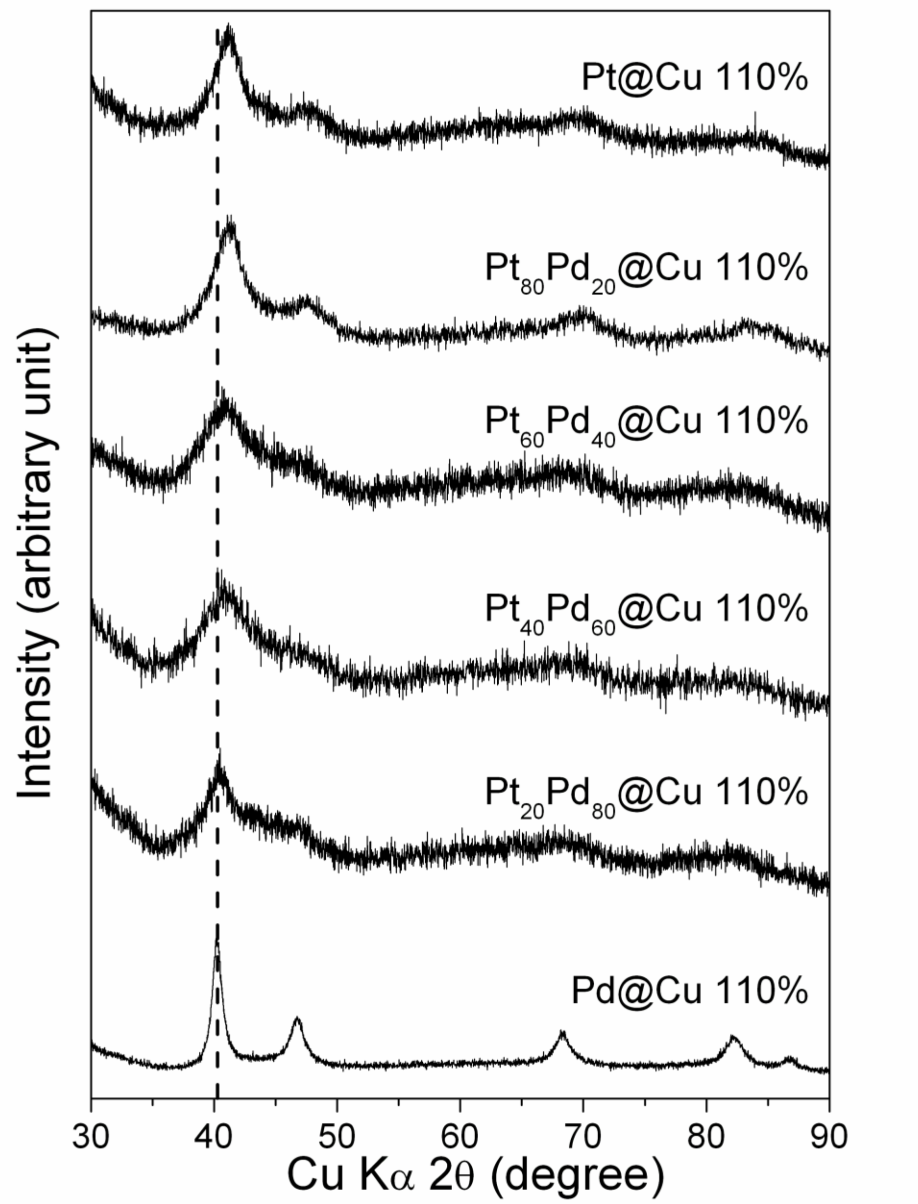

Figure 5.7. XRD patterns of Pt$_x$Pd$_{1-x}$@Cu 110% ($0 \leq x \leq 100$) after acid treatment. The dashed line corresponds to the expected position of the (111) reflection in Pd (#00-046-1043).

Figure 5.8 presents the cyclic voltammograms of the Pt_xPd_{1-x}@Cu 110% ($0 \leq x \leq 100$) samples along with that of the Pt@Cu 110% sample. Significant differences are observed in the hydrogen region of the CV. Presence of Pd on the surface causes modification of the hydrogen desorption peak in the region between 0.1 and 0.2 V *vs* NHE. A new peak appears at 0.15 V *vs* NHE and becomes sharper with increasing Pd content as can be seen with the $Pt_{20}Pd_{80}$@Cu 110% sample. The appearance of these peaks suggests that adsorption of hydrogen both on Pt atoms as well as on Pd atoms on the surface. Similar features have been observed by Clavilier *et al.*[184,185] in the CVs of co-precipitated Pt-Pd nanoparticles. The CV of Pd, however, displays the characteristic features of Pd. It was also observed that the double layer capacitance in case of Pd@Cu 110% was substantially smaller than those of other Pt_xPd_{100-x}@Cu 110% samples. Additionally, a decrease in the water activation potential was observed for the Pd-containing samples compared to the Pt@Cu 110% sample and the current density due to water activation increases with increasing Pd content. Thus, it can be postulated that the presence of Pd along with Pt atoms on the surface causes substantially more coverage due to hydroxide formation compared to the presence of Pt atoms alone.

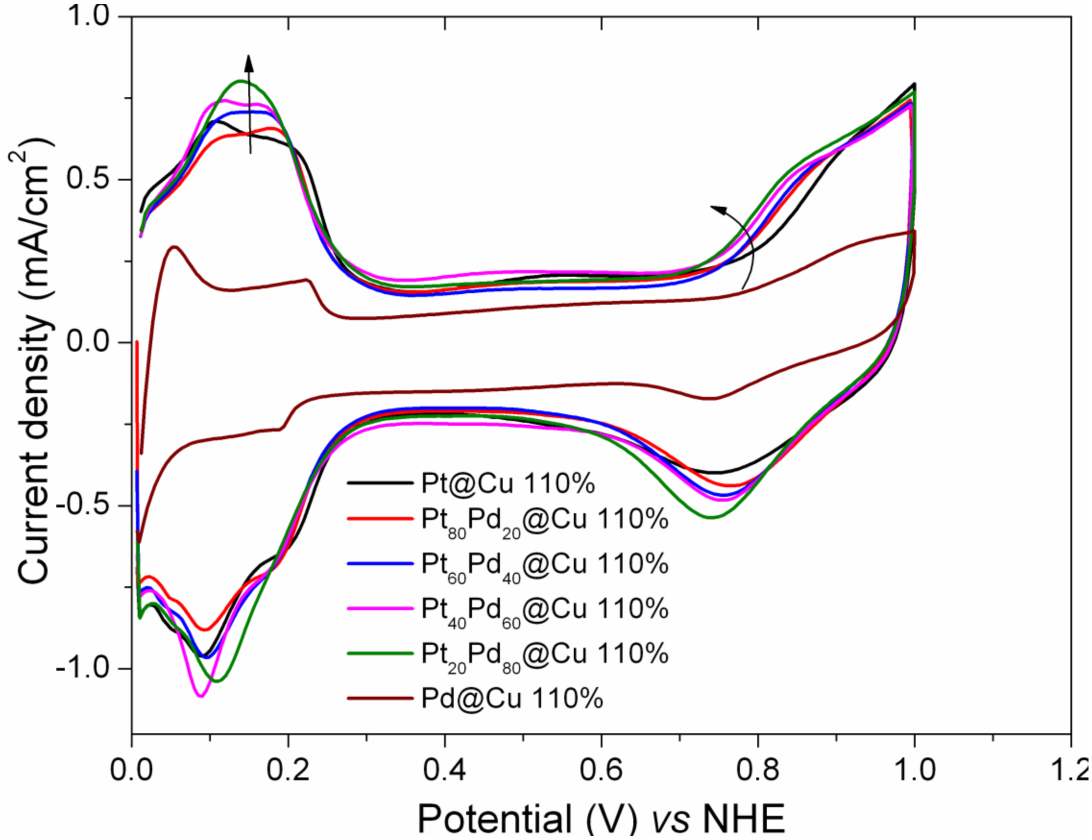

Figure 5.8. Cyclic voltammograms of Pt_xPd_{1-x}@Cu 110% ($0 \leq x \leq 100$) after acid treatment in N_2 saturated 0.5 M H_2SO_4 at 50 mV/s.

The oxygen reduction activities for the Pt_xPd_{100-x} samples are shown in Fig. 5.9. It is evident from the data in Fig. 5.9 that the ORR activity decreases with increasing Pd content. The decrease in activity is most likely due to the higher coverage of OH^- as discussed earlier. Indeed, the CV profiles show that Pd incorporation causes a negative shift in water activation potential (towards lower value compared to that in Pt@Cu 110%). The coverage for the Pt_xPd_{100-x}@Cu 110% has not been determined due to the uncertainty in the estimation of electrochemical active surface area. Additionally, it was observed that the inclusion of a small amount of Pt (as in the $Pt_{20}Pd_{80}$@ Cu 110%

sample) results in multifold increase in activity for ORR compared to that found with Pd@Cu 110% (Fig. 5.9(c).

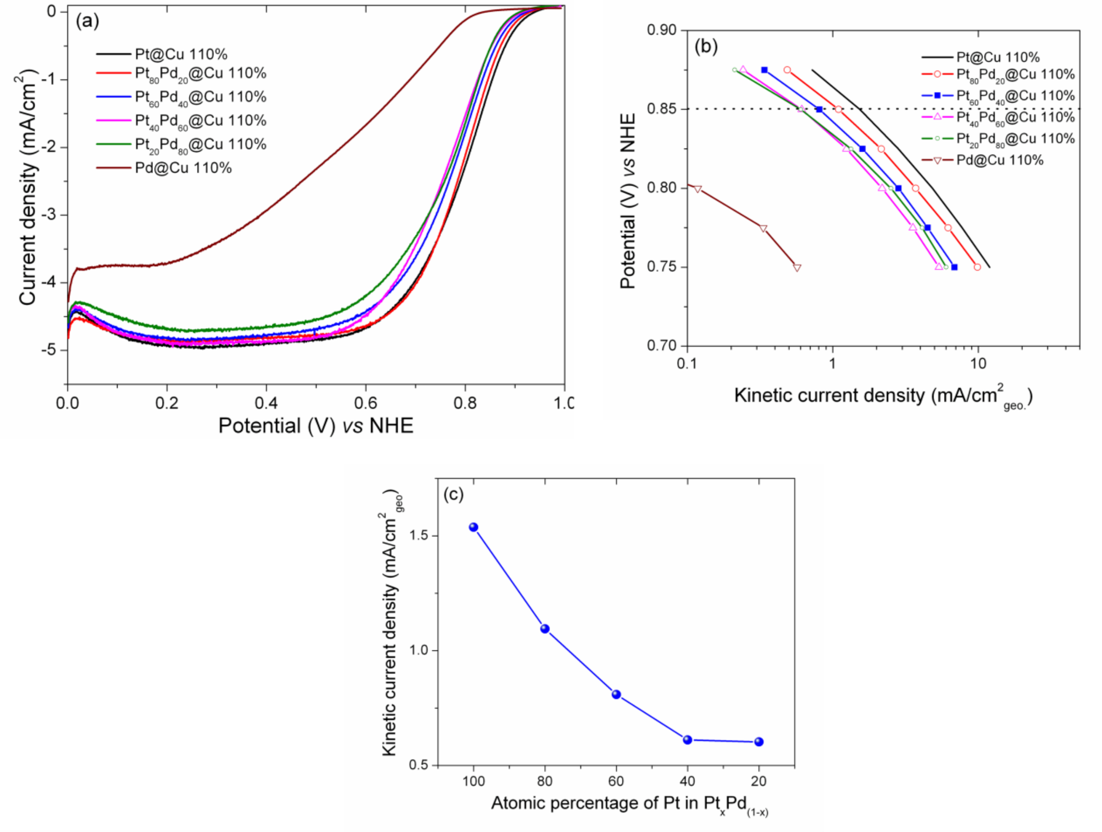

Figure 5.9. (a) Hydrodynamic polarization curves of selected Pt$_x$Pd$_{100-x}$@Cu 110% samples along with commercial Pt in O$_2$ saturated 0.5 M H$_2$SO$_4$ at room temperature and 1600 rpm, (b) mass transfer corrected Tafel plots for Pt$_x$Pd$_{100-x}$@Cu 110% ($0 \leq x \leq 110$), and (c) variation of kinetic current density at 0.85 V *vs* NHE (obtained from Tafel plots) with atomic percentage of Pt.

4. CONCLUSIONS

A galvanic displacement reaction between pre-fabricated carbon-supported Cu nanoparticles and Pt^{4+} has been pursued to obtain a "core-shell" structure having a Pt-Cu core with a Pt shell (Pt@Cu) and has been employed as electrocatalysts for ORR. XRD data and Pt : Cu atom ratios obtained from EDS analysis suggest the presence of a Pt-Cu alloy core underneath the Pt shell. The CV profiles of the carbon-supported Pt@Cu samples resemble that of polycrystalline Pt and no signals corresponding to the dissolution of Cu upon potential cycling could be detected. RDE and single cell PEMFC data demonstrate that the Pt@Cu 110% sample exhibits significantly higher activity for ORR compared to commercial Pt catalyst. Moreover, the surface area specific activities of the Pt@Cu samples show a linear increase with increasing initial nominal Cu content, and the observation could be attributed to an electronic modification of the Pt shell by the inner Pt-Cu core.

Subsequently, the reaction has been modified to synthesize a series of Pt_xPd_{100-x}@Cu 110% nanoparticles and the samples have been characterized for their structure and activity towards ORR. Interestingly, it is found that under similar conditions, the Pd@Cu 110% sample has remarkably different structure than the Pt@Cu 110% sample. The oxygen reduction activity was found to deteriorate with increasing Pd content in Pt_xPd_{100-x}@Cu 110% possibly due to a strong adsorption of OH^- on the surface.

Chapter 6: Summary

The objective of this dissertation was to develop low-platinum and non-platinum electrocatalysts for oxygen reduction reaction in fuel cells. In this regard, two palladium-based Pd-M (M= Mo and W) alloy systems have been investigated. A new synthetic procedure involving microwave irradiation has been used to synthesize a series of low Pt content electrocatalysts and explored for their activities towards ORR. Additionally, a new procedure involving a galvanic replacement reaction has been employed to synthesize "core-shell" nanoparticles with Pt or Pt-Pd shell and Cu core. The results are briefly summarized below.

A novel and facile synthesis approach involving decomposition of organo-metallic precursors has been adopted to prepare carbon-supported $Pd_{100-x}Mo_x$ ($0 \leq x \leq 40$) and $Pd_{100-y}W_y$ ($0 \leq y \leq 30$). The carbon-supported nanoparticles have been heat treated to achieve good alloying and investigated for their phase structure. Alloying of Pd with Mo and W is found to increase both the catalytic activity for ORR and the catalyst durability. XPS analysis shows a change in chemical environment of Pd upon alloying with both Mo and W, which might have an important bearing on the increased activity for ORR. The mass activity of $Pd_{95}W_5$ is comparable to that of as-synthesized Pt. In addition, both the Pd-Mo and Pd-W alloy electrocatalysts offer an important advantage of high tolerance to methanol compared to Pt.

A rapid synthesis process taking advantages of both the microwave and solvothermal effects has been pursued to obtain a seed-mediated growth of multimetallic Pt-Pd-Co nanoalloy electrocatalysts as well as Pt-encapsulated Pd-Co nanoparticles with a high degree of alloying and controlled particle size within a short reaction time (15 min) at < 300 ^{o}C without any post annealing in reducing gas atmospheres. Particularly, the ternary electrocatalyst $Pt_{70}Pd_{20}Co_{10}$ synthesized by the MW-ST method shows ORR activity comparable to that of commercial Pt while lowering the cost significantly. Due to an added advantage of the high tolerance of Pd-containing alloy catalysts to methanol, the activity of $Pt_{50}Pd_{30}Co_{20}$ for ORR in DMFC is superior to that of commercial Pt at higher methanol concentrations. Additionally, a systematic analysis of the as-synthesized Pt-encapsulalated Pd-Co system by XRD, TEM, and XPS of the as-synthesized samples confirm the presence of Pt overlayers on the surface of Pd-Co nanoparticles. RDE experiments show that the 75% $Pd_{80}Co_{20}$ + 25% Pt sample with a Pt loading of 5 wt % exhibits higher catalytic activity for ORR compared to either $Pd_{80}Co_{20}$ or Pt synthesized by the same method (all having the same total metal loading of 20 wt. %), demonstrating the influence of Pd-Co core on the outermost Pt layer in enhancing the catalytic activity. Single cell PEMFC data confirm the RDE data and affirm the enhancement in catalytic activity per unit mass of Pt on encapsulating Pd-Co by Pt.

Carbon-supported Pt@Cu "core-shell" nanoparticles with Pt-Cu alloy core and Pt shell have been synthesized by a galvanic displacement of Cu by Pt^{4+} at ambient conditions, followed by a leaching out of unreacted Cu on the surface by treating with 9 M H_2SO_4. XRD data and EDS analysis indicate the formation of a Pt-Cu alloy below the Pt shell. Both, the hydrodynamic polarization data in a RDE setup and single cell PEMFC data demonstrate an enhanced catalytic activity for the oxygen reduction reaction at optimum Pt@Cu compositions compared to that found with commercial Pt catalyst, both per unit mass of Pt and per unit active surface area basis. Moreover, the surface area specific activities of the Pt@Cu samples increase linearly with increasing initial nominal Cu content. The increase in activity for ORR is ascribed to an electronic modification of the outer Pt shell by the Pt-Cu core. However, inclusion of Pd on the surface of Pt@Cu "core-shell" nanoparticles deteriorates the activity for ORR.

Bibliography

[1] K. Kordesh and G. Simader, *Fuel Cells and their Applications*, VCH, 1996.

[2] A. J. Appelby and F. R. Foulkes, *Fuel cell Handbook*, Van Nostrand Reinhold, New York, 1988.

[3] National Energy Technology laboratory, U. S. Department of Energy, *Fuel cell Handbook (7th Edition)*, 2004.

[4] F. Barbir, *PEM Fuel Cells: Theory and Practice*, Elsevier Academic Press, 2005.

[5] J. Larminie and A. Dicks, *Fuel Cell Systems Explained*, John Wiley & Sons, Chichester, 2001.

[6] R. O. Hayre, W. Colella, S. K. Cha and F. B. Prinz, *Fuel Cell Fundamentals*, John Wiley & Sons, New York, 2006.

[7] K. B. Oldhan and J. C. Myland, *Fundamentals of Electrochemical Science*, Academic Press Inc., San Diego, USA, 1994.

[8] C. M. A. Brett and A. M. O. Brett, *Electrochemistry, Principles, Methods, and Applications*, Oxford University Press, New York, USA, 1993.

[9] A. J. Bard and L. R. Faulkner, *Electrochemical methods: Fundamentals and Applications*, John Wiley, New York, 2001.

[10] J. S. Newman and K. E. Thomas-Alyea, *Electrochemical Systems*, John Wiley & Sons, Inc., Hoboken, New Jersey. 2004.

[11] S. Srinivasan, *Fuel Cells: From Fundamentals to Applications*, Springer Varlag, 2005.

[12] Y. Shao-Horn, W.C. Sheng, S. Chen, P.J. Ferreira, E. Holby, and D. Morgan, *Top. Catal.* , **46**, 285 (2007).

[13] P.J. Ferreira and Y. Shao-Horn, *Electrochem. Solid-State Lett.*, **10**, B60 (2007).

[14] E. Guilminot, A. Corcella, F. Charlot, F. Maillard, and M. Chatenet, *J. Electrochem. Soc.***, 154**, B96 (2007).

[15] C. H. Paik, G. S. Saloka, and G. W. Graham, *Electrochem. Solid-State Lett.*, **10,** B39 (2007).

[16] K. Kinoshita, J. T. Lundquist and P. J. Stonehart, *Electroanal. Chem.*, **48**, 157 (1973).

[17] R. M. Darling and J. P. Meyers, *J. Electrochem. Soc.*, **150**, A1523 (2003).

[18] R. M. Darling and J. P. Meyers, *J. Electrochem. Soc.*, **152**, A242 (2005).

[19] R. Borup, J. Meyers, B.Pivovar, Y. S. Kim, R. Mukundan, N. Garland, D. Myers, M. Wilson, F. Garzon, D. Wood, P. Zelenay, K. More, K. Stroh, T. Zawodzinski, J. Boncella, J. E. McGrath, M. Inaba, K. Miyatake, M. Hori, K. Ota, Z. Ogumi, S. Miyata, A. Nishikata, Z. Siroma, Y. Uchimoto, K. Yasuda, K. Kimijima, and N. Iwashita, *Chem. Rev.*, **107**, 3904 (2007).

[20] E. J. Carlson, P. Kofp, J. Sinha, S. Srimalu, and Y. Yang*, Cost Analysis of PEM Fuel cell Systems for Transportation*, National Renewable Energy Laboratory, report NREL/SR-560-39104, 2005.

[21] H. Wroblowa, Y.C. Pan and J. Razumney, *J. Electroanal. Chem.,* **69**, 195 (1976).

[22] N. M. Markovic, T. J. Schmidt, V. Stamenkovic, and P. N. Ross, *Fuel Cell*s, **1**, 105 (2001).

[23] K. Kinoshita, *Electrochemical Oxygen Technology*, John Wiley & Sons, New York 1992.

[24] D. Thompsett, Pt alloys as oxygen reduction catalysts, in W. Vielstich, H. A. Gasteiger and A. lamm (eds.), Handbook of fuel cells- fundamentals, technology and applications, John Wiley &Sons, New York, 2003.

[25] S. Mukherjee and S. Srinivasan, *J. Electroanal. Chem.*, **357**,201 (1993).

[26] S. Mukherjee, S. Srinivasan, M. P. Soriaga, *J. Electrochem. Soc.*, **142**, 1409 (1995).

[27] L. Xiong and A. Manthiram, *J. Mater Chem.,* **14,** 1454 (2004).

[28] H. Yano, M. Kataoka, H. Yamashita, H. Uchida, and M. Watanabe, *Langmuir,* **23,** 6438 (2007).

[29] E. Antolini, J.R.C. Salgado, and E.R. Gonzalez, *J Electroanal Chem* **580,** 145 (2005).

[30] S.J. Seo, H.I. Joh, H.T. Kim, and S.H. Moon, *J Power Sources* **163**, 403 (2006).

[31] S. Mukherjee and S. Srinivasan O_2 reduction and structure-related parameters for supported catalysts, in W. Vielstich, H. A. Gasteiger and A. lamm (eds.), *Handbook of fuel cells- fundamentals, technology and applications*, John Wiley &Sons, New York, 2003.

[32] T. Toda, H. Igarashi, H. Uchida, and M. Watanabe, *J Electrochem Soc* **146**, 3750(1999).

[33] M.T. Paffett, J.G. Beery, and Sh Gottesfeld, *J Electrochem Soc* **135**, 1431 (1988).

[34] K. Kinoshita, *J. Electrochem. Soc.*, **137**, 845 (1990).

[35] U. Bardi, B. Beard, and P. N. Ross, *J. Vac. Sci. Technol. A*,, **6**, 665 (1988).

[36] U. Bardi, A. Atrei, P. N. Ross, E. Zanazzi, and G. Rovida, *Surf. Sci.*, **211,** 441 (1989).

[37] U. Bardi, B. Beard, and P. N. Ross, *J. Catal.*, **124**, 22 (1990).

[38] V. Jalan and E.J. Taylor, *J Electrochem Soc* **130**, 2299 (1983).

[39] E. Antolini, J.R.C. Salgado, M.J. Giz, and E.R. Gonzalez, *Int J Hydrogen Energ* **30**, 1213 (2005).

[40] B.C. Beard and P.N. Ross, *J Electrochem Soc* **137**, 3386 (1990).

[41] A. K. Shukla, M. Neergat, P. Bera, V. Jayaram, and M. S. Hegde, *J. Electroanal. Chem.*, **504**, 111 (2001).

[42] M. Min, J. Cho, K. Cho, and H. Kim, *Electrochim. Acta,* **45**, 4211 (2000).

[43] V. Stamenkovic, T. J. Schmidt, P. N. Ross and N. M. Markovic, *J. Phy. Chem. B.,* **106,** 11970 (2002).

[44] V. Stamenkovic, B. S. Mun, K. J. J. Mayrhofer, P. N. Ross, N. M. Markovic, and J. Rossmeisl, *Angew. Chem. Int. Eds.,* **45,** 2897(2006).

[45] M. Teliska, V. S. Murthi, S. Mukerjee, and D. E. Ramaker, *J. Electrochem. Soc.* **152,** A2159 (2005)

[46] J. Roques,A. B. Anderson, V. S. Murthi, and S. Mukerjee*, J. Electrochem. Soc.* **152,** E193 (2005)

[47] Y. Xu, M. Shao, M. Mavrikakis, and R. R. Adzic, Recent developments in the electrocatalysis of the O_2 reduction reaction, in A. Wieckowski and M. T. Kooper (eds.) *Fuel Cell Catalysis, A Surface Science Approach*, John Wiley & Sons, NJ 2009.

[48] V. S. Murthi, R. C. Urian, and S. Mukherjee, *J. Phys. Chem. B*, **108**, 11011 (2004).

[49] A. B. Anderson, *Electrocheim Acta,* **47**, 3759 (2002).

[50] A. B. Anderson, J. Roques, S. Mukerjee , Vivek S. Murthi, N. M. Markovic, and V. Stamenkovic*, J. Phys. Chem. B,* **109**, 1198(2005).

[51] S. Koh and P. Strasser, *J. Am. Chem. Soc.*, **129**, 12624 (2007).

[52] P. Mani, R. Srivastava, and P. Strasser, J. *Phy. Chem. C*, **112**, 2770, (2008).

[53] R. R. Adzic and J. X. Wang*, Electrochem Acta*, **45**, 4203 (2000).

[54] P. W. Faguy, N. Markovic, R. R. Adzic, C. Fierro, and E. Yeager, *J. Electroanal. Chem.*, **289**, 245 (1990).

[55] P. W. Faguy, N. S. Marinkovic, and R. R. Adzic, *J. Electroanal. Chem,.* **407**, 209 (1996).

[56] J. X. Wang, N. S. Marinkovic, R. R. Adzic*, J. Phy. Chem. B.*, **108**, 4127 (2004).

[57] J. X. Wang, J. L. Zhang, and R. R. Adzic, *J. Phy. Chem. A*. **111**. 12702 (2007).

[58] S. Mukerjee, S. Srinivasan, M. Soriaga, and J. McBreen, *J. Electrochem. Soc.*, **142**, 1409 (1995).

[59] S. Chen, P. J. Ferreira, W. Sheng, N. Yabuuchi, L. F. Allard and Y. Shao-Horn, *J. Am. Chem. Soc.*, **130**, 13818 (2008).

[60] J. Greeley, J. K. Norskov, and M. Mavrikakis, *Annu. Rev. Phy. Chem*., **53**, 319 (2002).

[61] N. M. Mavrikakis, B. Hammer, J. K. Norskov, *Phys. Rev. Lett.*, **81**, 2819 (1998).

[62] B. Hammer, J. K. Norskov, *Surf. Sci*. **343**, 211 (1995)

[63] S. R. Brankovic, J. X. Wang, and R. R. Adzic*, Surf. Sci.* **474**, L173 (2001).

[64] S. R. Brankovic, J. X. Wang, and R. R. Adzic, *Electrochem. Solid State. Lett.* **4**, A217 (2001).

[65] R. R. Adzic, in A. J. Bard and M. Stratmann (eds.) *Encyclopedia of electrochemistry*, Vol-1, Wiley-VCH New York.

[66] M. H. Shao, T. Huang, P. Liu, J. Zhang, K. Sasaki, M. B. Vukrimovic, and R. R. Adzic, *Langmuir*, **22**, 10409(2006).

[67] M. Shao, K. Sasaki, P. Liu, and R. R. Adzic, *Z. Phys. Chem*, **221**, 1175(2007).

[68] J. Zhang, M. B. Vukmirovic, K. Sasaki, A. U. Nilekar, M. Mavrikakis, and R. R. Adzic, *J. Am. Chem Soc*., **127**, 12480 (2005).

[69] J. Zhang, Y. Mo, M. B. Vukmirovic, R. Klie, K. Sasaki, and R. R. Adzic, *J. Phy. Chem. B*, **108**, 10955 (2004).

[70] M. Shao, K. Sasaki, N. S. Marinkovic, L. Zhang and R. R. Adzic, *Electrochem. Commun.*, **12**, 2848 (2007).

[71] J. Zhang, M. B. Vukrimovuic, Y. Xu, M. Mavrikakis, and R. R. Adzic, *Angew. Chem. Int. Eds*. **44**, 2132 (2005).

[72] R. R. Adzic, J. Zhang, K. Sasaki, M. B. Vukrimovic, M. Shao, J. X. Wang, A. U. Nilekar, M. Mavrikakis, J. A. Valeiro, and F. Uribe, *Top. Catal.* , **46**, 249 (2007).

[73] R. Srivastava, P. Mani, N. Hahn, and P. Strasser, *Angew. Chem. Int. Eds*. **46**, 8988 (2007).

[74] R. Jasinski, *Nature*, **201**, 1212 (1964),

[75] J. H. Zagal, Macrocycles, in W. Vielstich, H. A. Gasteiger and A. lamm (eds.), *Handbook of fuel cells- fundamentals, technology and applications*, John Wiley &Sons, New York, 2003.

[76] J. H. Zagal*, Coor. Che. Rev*. **119**, 89, 1992.

[77] H. Alt, M. Binder, and G. Sandstede, *J. Catal*., **28**, 8 (1973).

[78] P. H. Matter and U. S. Ozkan*, Catal. Lettr*., **109**, 115 (2006).

[79] R. Bashyan and P. Zalenay, *Nature*, **443**, 63 (2006).

[80] S. Ye, a. K. Vijh, *Electrochem. Commun*., **5**, 272 (2005).

[81] S. Gupta, D. Tyrk, I. Bae, W. Aldred, and E. Yeager*, J. Appl. Electrochem*, **19**, 19 (1989).

[82] H. Binder, A. Kohling, W. Kuhn, W. Linder, and G. Sandstede, *Nature*, **224**, 1299 (1969).

[83] L. H. Bennett, J. R. Cuthill, A. J. Alister, N. E. Erickson, *Science*, **184**, 56365 (1974).

[84] P. N. Ross and P. Stonehart, *J. Catal*, **39**, 298 (1975).

[85] P. N. Ross and P. Stonehart, *J. Catal*, **48**, 42 (1977).

[86] R. J. Colton, J. T. J. Huang, and R. W. Rabalias, *Chem. Phy. Lett*., **34**, 337 (1975).

[87] R. B. Levy and M. Boudart, *Science*, **181**, 547 (1973).

[88] J. Giner and L. Swette, *Nature*, **211**, 1291 (1966).

[89] H. Zhong, H. Zhang, G. Liu, Y. Liang, J. Hu, and B. Yi, *Electrochem. Commun*., **8**, 707 (2006).

[90] H. Zhong, H. Zhang, Y. Liang, J. Zhang, M. Wang, and X. Wang, *J. Pow. Source*, **164**, 572 (2007).

[91] N. Alonso-Vante and H. Tributsch, *Nature*, **323**, 431 (1986).

[92] N. Alonso-Vante, Chavel phases and chalcogenides, in W. Vielstich, H. A. Gasteiger and A. lamm (eds.), *Handbook of fuel cells- fundamentals, technology and applications*, John Wiley &Sons, New York, 2003.

[93] S. Campbell, Development of transition metal/chalcogen based cathode catalyst for PEM fuel cells, DOE hydrogen program, FY 2006 annual progress report (2006).

[94] K. Lee, L. Zhang, and J. Zhang, *Electrochem Commun*, **9**, 1704 (2007).

[95] O. Savadogo, K. Lee, K. Oishi, S. Mitsushimas, N. Kamiya, and K. I. Ota, *Electrochem. Commun.* 6, 105(2004).

[96] J. L. Fernandez, D. A. Walsh, A. J. Bard, *J. Am. Chem. Soc.* **127,** 357 (2005).

[97] J. L. Fernandez, V. Raghuveer, A. Manthiram, A. J. Bard, *J. Am. Chem. Soc.* **127**, 13100 (2005).

[98] V. Raghuveer, A. Manthiram, A. J. Bard, *J. Phys. Chem. B.*,**109**, 22909 (2005).

[99] V. Raghuveer, P. J. Ferreira, A. Manthiram, *Electrochem. Commun* .**8**, 807 (2006).

[100] A. J. Bard, R. Parsons, and J. Jordan (eds.) *Standard Potentials in Aqueous Solutions*, Marcel Dekker, New York, 1985.

[101] M. H. Shao, K. Sasaki, and R. R. Adzic*, J. Am. Chem. Soc*., **128**, 3526(2006).

[102] X. Wang, N. Kariuki, J. T. Vaughey, J. Goodpaster, R. Kumar, and D. Myers, *J. Electrochem. Soc.*, **155**, B602 (2008).

[103] G. Ramos-Sánchez, H. Yee-Madeira, and O. Solorza-Feria*, Int. J. Hydrogen Energy*, **33**, 3596 (2008).

[104] E. Antoline, *Energy Env. Sci*., 2009**, DOI:** 10.1039/b820837a

[105] B. D. Cullity, *Elements of X-ray diffraction*, 2nd Eds. Addison-Wesley, Reading, 1978

[106] X-ray crystallography, http://en.wikipedia.org/wiki/X-ray_crystallography, site accessed on 10th July 2009.

[107] J. Goldstein, D. Newbury, D. Joy, C. Lyman, P. Echlin, E. Lifshin, L. Sawyer, and J. Michael, *Scanning electron microscopy and x-ray microanalysis*, 3rd Eds. Kluwer Academic, New York, 2003.

[108] Y. W. Chung, *Practical Guide to Surface Science and Spectroscopy*, Academic Press, San Diego, 2001.

[109] J. F. Watts and J. Wolstenholme, *An introduction to surface analysis by XPS and AES*, John Wiley & Sons, Chichester, 2002.

[110] C. M. A. Brett and A. M. O. Brett, *Electrochemistry, Principles, Methods, and Applications*, Oxford University Press, New York, 1994.

[111] E. G. Compton and C. E. Banks, *Understanding voltammetry*, World Scientific Publishing Company, 2007.

[112] Cynthia G. Zoski (eds.), *Handbook of Electrochemistry*, Elsevier, Boston, 2007.

[113] V. S. Bogostky, *Fundamentals of Electrochemistry 2nd Eds*., Wiley-Interscience, Hoboken, 2006.

[114] J. Wang, *Analytical Electrochemistry*, Wiley-VCH, Hoboken, 2006.

[115] P. A. Christensen and A. Hamnett, *Techniques and Mechanisms of Electrochemistry,* Blackie Academic & Professional, London, 1994.

[116] M. Grden, M. Lukaszewski, G. Jerkiewicz, A. Czerwinski, *Electrochim. Acta*, **53**, 7583 (2008).

[117] L.D. Burke and M.B.C. Roche, *J. Electroanal. Chem.,* **186**, 139 (1985).

[118] K. Juodkazis, J. Juodkazyt, B. Sebeka, G. Stalnionis, and A. Lukinskas, *Russ. J. Electrochem.* **39,** 959 (2003).

[119] L.D. Burke and J.K. Casey, *J. Electrochem. Soc.*, **140**, 1284 (1993).

[120] K. Juodkazis, J. Juodkazyt, B. Sebeka, G. Stalnionis, and A. Lukinskas, *Russ. J. Electrochem.* **39**, 959 (2003).

[121] M. Łukaszewski and A. Czerwiński, *J. Electroanal. Chem.* **589** 38 (2006).

[122] A.E. Bolzán, *J. Electroanal. Chem.* **380**, 127 (1995).

[123] S.H. Cadle, *Anal. Chem,.*.**46**,547 (1974).

[124] L.D. Burke and J.K. Casey, *J. Electrochem. Soc.* **140**, 1284 (1993).

[125] S.H. Cadle, *J. Electrochem. Soc.* **121**, 645 (1974).

[126] D.A.J. Rand and R. Woods, *J. Electroanal. Chem.* **35**, 209 (1972).

[127] A. Bolzan, M.E. Martins and A.J. Arvia, *J. Electroanal. Chem.* **207**, 279, (1986).

[128] A. Bolzan, M.E. Martins and A.J. Arvía, *J. Electroanal. Chem.* **172**, 221 (1984).

[129] M. Tian and B.E. Conway, *J. Electroanal. Chem.* **581**, 176 (2005).

[130] J.A. Schimpf, J.R. McBride and M.P. Soriaga, *J. Phys. Chem.* **97, 10518** (1993).

[131] H. Okamoto, *J. Phase Equilib*., **13**, 332 (1992).

[132] A. V. Ruban, H. L. Skriver, J. K. Norskov, *Phys. Rev. B: Condens. Matter Mater. Phys.*, **59**, 15990 (1999).

[133] V. Climent, N. M. Markovic, and P. N. Ross, *J. Phys. Chem. B,*. 104. 3116 (2000).

[134] S. V. Nagendra Naidu and P. Rama Rao, *J. Alloy Phase Diagr.*, **6**, 67 (1990).

[135] K. S. Kim, A. F. Gossmann and N. Winograd, *Anal. Chem.*, **46**, 197(1974).

[136] K. Noack, H. Zbinden and R. Schlögl, *Catal. Lett.*, **4**, 145(1990).

[137] G. E. McGuire, G. Kk. Schweitzer and T. A. Carlson, *Inorg. Chem.*, **12,** 2451(1973).

[138] K. T. Ng and D. M. Hercules, *J. Phys. Chem.*, **80**, 2095, (1976).

[139] R. Venkataraman, H. R. Kunz, and J. M. Fenton, *J. Electrochem. Soc*., **150**, A278 (2003).

[140] H. Li, Q. Xin, W. Li, Z. Zhou, L. Jiang, S. Yang and G. Sun, *Chem. Commun.*, 2004, 2776.

[141] J. Yang, J. Y. Lee, Q. Zhang, W. Zhou and Z. L. Yang, *J. Electrochem. Soc.*, **155,** B776, **(**2008).

[142] W. Wang, Q. Huang, J. Liu, Z. Zou, Z. Li and H. Yang, *Electrochem. Commun.*, **10**, 1396, (2008).

[143] M. D. Macia, J. M. Campina, E. Herrero, and J. M. Feliu, *J. Electroanal. Chem.* **564,** 141 (2004).

[144] W. E. Mustain, K. Keith and J. Prakash, *Electrochem. Commun.*, 8, 406 (2006).

[145] L. Zhang, L. Kunchan and J. Zhang, *Electrochim. Acta*, **52**, 3088 (2007).

[146] A. Eichler, F. Mittendorfer, J. Hafner, *J. Phys. Rev. B: Condens. Matter Mater. Phys*. **62¸**4744 **(**2000).

[147] W. Wang, Q. Huang, J. Liu, Z. Zou, Z. Li, H. Yang, *Electrochem. Commun*., **10**, 1396(2008).

[148] G. Vijayaraghavan and K. J. Stevenson in J. Weidner, N. Dudney, S. Minteer, K. Zaghib, (eds.) *Electrochemistry of Novel Electrode Materials for Energy Conversion and Storage*, Pennington, NJ, 2007, ECS Transactions, Vol. 6, Issue 25, 43-50.

[149] K. Yu Chan, J. Ding, J. Ren, S. Cheng, and K. Y. Tsang, *J. Mat. Chem.* **14,** 505 (2004).

[150] S. Eriksson, U. Nylén, S. Rojas, M. Boutonnet, *Appl. Catal.* , **265**, 207(2004).

[151] E. I. Santiago, L. C. Varanda, H. M. Villullas, *J. Phy. Chem. C*, **111**, 3146(2007).

[152] Z. Liu, C. Yu, I. A. Rusakova, D. Huang and P. Strasser, *Top. Catal.* , **49***,* 1022(2008).

[153] X. Zhang and K. Y. Chan, *J. Mater. Chem.,* **12**, 1203(2002).

[154] X. Zhang and K. Y. Chan, *Chem. Mater.*, **15**, 451(2003).

[155] Z. Liu, J. Lee, M. Han, W. Chen, and L. Gan, *J. Mater. Chem.*, **12,** 2453(2002).

[156] W. X. Chen, J. Y. Lee , and Z. Liu, *Chem. Commun.*, **8***,* 2588(2002**).**

[157] S. Komarneni, *Curr. Sci.*, **85**, 1730(2003).

[158] K. J. Rao, B. Vaidhyanathan, M. Ganguli, and P. A. Ramakrishnan, *Chem. Mater.*, **11,** 882 (1999).

[159] G. Garnweitner and M. Niederberger, *J. Mater. Chem*., **18**, 1171(2008).

[160] A. Vadivel Murugan, T. Muraliganth and A. Manthiram, *J. Phy. Chem. C*, **112**, 14665(2008).

[161] A. J. Kidney,W. R. Parish, *Fundamentals of Natural Gas Processing*, Taylor & Francis, Boca Raton, 2006.

[162] S. Gottesfeld, I. D. Raistrick, S. Srinivasan, *J. Electrochem. Soc.*, **134,** 1455(1987).

[163] G. Jerkiewicz, *Prog. Surf. Sci.*, **57**, 137(1998).

[164] D. Wang, K. Y. Lee, S. Luo and T. B. Flangan, *J. Alloys Compounds* , **252**, 209(1997).

[165] M. Grden, A. Piacik, Z. Koczorowski, A. Czerwinski, *J. Electroanal. Chem.,* **532**, 35(2002).

[166] H. Kobayashi, M. Yamauchi, H. Kitagawa, Y. Kubota, K. Kato, M. Takata, *J. Am. Chem. Soc.*, **130**, 1818(2008).

[167] Zengcai Liu, Shirlaine Koh, Chengfei Yu, and Peter Strasser *J. Electrochem. Soc.* **154** B1192 (2007).

[168] Shirlaine Koh, Nathan Hahn, Chengfei Yu, and Peter Strasser *J. Electrochem. Soc.* **155** B1281 (2008).

[169] Y. Sun and Y. Xia, *Science*, **298**, 2176 (2002).

[170] Y. Sun and Y. Xia, *J. Am. Chem. Soc.*, **126**, 3892 (2004).

[171] J. Chen, J. M. MaLellan, A. Siekkinen, Y. Xiong, Z. Li, and Y. Xia, Y. *J. Am. Chem. Soc.* , **128**, 14776(2006).

[172] S. E. Skrabalak, J. Chen, L. Au, X. Lu**,** X. Li and Y. Xia, *Adv. Mater.* , **19**, 3177(2007).

[173] B. Wiley, T. Herricks, Y. Sun, and Y. Xia, *Nano Lett.* , **4**, 1733(2004).

[174] H. M. Chen, R. Liu, M. Y. Lo, S. C. Chang, L. D. Tsai, Y. M. Peng, and J. F. Lee, *J. Phy. Chem. C*, **112**, 7522(2008).

[175] H. Lang, S. Maldonado, K. J. Stevenson, and B. D. Chandler, *J. Am. Chem. Soc.,* **126**, 12949(2004).

[176] S. Zhou, B. Varughese, B. Eichhorn, G. Jackson, and K. McIlwrath, *Angew. Chem. Int. Ed.*, **44**, 4539(2005).

[177] Z. D. Wei, Y. C. Feng, L. Li,M. J. Liao, Y. Fu, C. X. Sun, Z. G. Shao, and P. K. Shen*, J. Power Source*, **180**, 84(2008).

[178] D. R. Lide, D. R. *CRC Handbook of Chemistry and Physics*, 79th ed.; CRC Press: Boca Raton, **1998.**

[179] F. J. Vidal-Iglesias, J. Solla-Gullon, P. Rodrigiez, E. Herrero, V. Montiel, J. M. Feliu, J and A. Aldaz, *Electrochem. Commun.,* **6**, 1080 (2004).

[180] J. Solla-Gullon, P. Rodrigiez, E. Herrero, J. M. Feliu, and A. Aldaz, *Phys. Chem. Chem. Phys.,* **10**, 1359(2008).

[181] M. D. Macia, J. M. Campina, E. Herrero, and J. M. Feliu, *J. Electroanal. Chem.*, **564**, 141(2003).

[182] N. M. Markovic, in *Handbook of Fuel Cells - Fundamentals, Technology and Application* (eds.) W. Vielstich, A. Lamm, and H. A. Gasteiger , John Wiley: Hoboken, NJ, 2003; Vol. 2.

[183] P. B. Balbuena, D. Altomare, N. Vadlamani, S. Bingi, L. A. Agapito, and J. M. Seminario, *J. Phys. Chem. A*, **108**, 6378(2004).

[184] J. Solla-Gullo, V. Montiel, A. Aldaz, and J. Clavilier, *J. Electrochem. Soc.*, **150**, E104 (2003).

Vita

Arindam Sarkar was born as the eldest son of P. K. Sarkar and B. Sarkar in Burdwan, West Bengal, India on 20th January 1979. He completed his high school from D. A. V. Public School, Ara, Jharkhand, India and higher secondary school from S.P.S.E.C. Kanpur, Uttar Pradesh, India. He earned his B. E. degree in Mechanical Engineering from B.I.T. Durg, Chattisgarh, India in 2001 and M.Tech in Energy Systems and Engineering from Indian Institute of Technology Bombay, Mumbai, India in 2004. He entered the Materials Science and Engineering Graduate Program, The University of Texas at Austin, Austin, U.S.A. in 2005.

List of publications:

1. A. Sarkar, A. Vadivel Murugan, and A. Manthiram, "Microwave-assisted metallurgy: one-pot, rapid solvothermal synthesis of nanoalloy electrocatalysts with enhanced tolerance to methanol poisoning," *Fuel cells* (submitted).
2. A. Sarkar, A. Vadivel Murugan, and A. Manthiram, "Low cost Pd-W nanoalloy electrocatalysts for oxygen reduction reaction in fuel cells," *Journal of Materials Chemistry*, **19**, 159-165 (2009).
3. A. Manthiram, A. Vadivel Murugan, A. Sarkar, and T. Muraliganth, "Nanostructured electrode materials for electrochemical energy storage and conversion," *Energy and Environmental Science*, **1**, 621-638 (2008).
4. A. Sarkar, A. Vadivel Murugan, and A. Manthiram, "Synthesis and characterization of nanostructured Pd-Mo electrocatalysts for oxygen reduction

reaction in fuel cells," *Journal of Physical Chemistry C*, **112**, 12037-12043 (2008).

5. A. Sarkar and R. Banerjee, "Net energy analysis of hydrogen storage options, "*International Journal of Hydrogen Energy*, **30**, 867-877 (2005).
6. A. Sarkar and R. Banerjee, "A quantitative method for characterization of carbon nanotubes for hydrogen storage," *International Journal of Hydrogen Energy*, **29**, 1487-1491 (2004).

Permanent address: 5/1A Garcha 1st Lane, Calcutta, West Bengal, India 700019.

This dissertation was typed by the author.